

Copyright

by

Roman Caudillo

2007

The Dissertation Committee for Roman Caudillo
certifies that this is the approved version of the following dissertation:

**Magnetic, Thermoelectric, and Electronic Properties of
Layered Oxides and Carbon Materials**

Committee:

John B. Goodenough, Supervisor

Miguel Jose-Yacamán, Supervisor

Arumugam Manthiram

Llewellyn Rabenberg

Desiderio Kovar

Jianshi Zhou

**Magnetic, Thermoelectric, and Electronic Properties of
Layered Oxides and Carbon Materials**

by

Roman Caudillo, B.S., M.S.

Dissertation

Presented to the Faculty of the Graduate School of

The University of Texas at Austin

in Partial Fulfillment

of the Requirements

for the Degree of

Doctor of Philosophy

The University of Texas at Austin

August 2007

To my parents, Susana and Roberto

Acknowledgments

First, I would like to express my sincere gratitude to Professor Goodenough for his guidance and support throughout the pursuit of my Ph.D. He is an exemplary role model, not only because of his numerous scientific and technological achievements, but because of the kindness and respect that he always shows for his fellow colleagues, his dedication to his students, and his ability to inspire and motivate others with his hard-work ethic and his often contagious, high-spirited laugh. Personally, he has opened my eyes to the fact that a successful career in science (and elsewhere) should not be primarily about personal accomplishments, but rather about the people that one can positively affect.

I would also like to thank Professor Yacaman for encouraging me to pursue my Ph.D. at UT-Austin and for giving me the opportunity to learn and apply TEM-related techniques to my scientific research. Great appreciation is extended to Dr. Mario Miki whose time and patience in teaching the details of operating a TEM were invaluable. I am also grateful to Professor Rabenberg, whose class provided a good basic understanding of the basic principles of the TEM and electron diffraction. I would like to thank Professor Zhou for his training and help with all of the experimental equipment in Professor Goodenough's laboratories, and I thank my entire committee for their advice, feedback, and revision of this dissertation.

Great appreciation is extended to all of my fellow group members, both past and present, from both Professor Yacaman's and Professor Goodenough's research

groups. I would like to thank Jose Luis Elechiguerra, Domingo Garcia, and Alejandra Camacho for their friendship and support, both within and outside of the laboratory, and especially Alejandra for recommending me for a research position at Intel. Thanks also to Luciana Meli and Abraham Arceo for their friendship and support and a wonderful honeymoon. A special thank you is extended to Francisco Rivadulla for introducing me to Na_xCoO_2 research in Spain and for teaching me the majority of the experimental techniques necessary for my research on Na_xCoO_2 . I would also like to thank Manolo Banobre for his collaboration investigating Na_xCoO_2 . I am extremely grateful to Ronald Dass for the innumerable times he helped me with experimental equipment, interpreting experimental data, or understanding a difficult solid-state physics or chemistry concept. I am grateful to Dr. Huang for his help in the laboratory and his taking the time to teach me how to make and measure the performance of a Li-ion coin-cell battery. Appreciation is extended to Alejandro Diaz-Ortiz for teaching me how use the LaTeX type-setting software used for writing this dissertation. I would like to also thank all of my previous office mates, including Jose Luis, Dr. Reyes-Gasga, Dr. Rodrigo Velazquez, Young, and Alejandro Torres, for many fruitful discussions. I extend my appreciation towards Lydia Griffith, Jamie Wentz, Fatima Bridgewater, and Barbara Espinoza for always being so pleasant and taking care of all the administrative details.

I would like to thank all of my friends outside of the university for their help, support, and encouragement during my studies; particularly Sam Armstrong and Ryan Wooley for their help in constructing figures and schematics using Illustrator, David Mott for always being willing to engage in scientific discussions with a skeptical eye, Lance Cain for legal advice, and Dan Baksht for his help calculating parabolic trajectories at Hancock.

Finally, I would like to acknowledge my family, without whom the pursuit of this Ph.D. would not have been possible in the first place. My parents have

always given me every possible opportunity to further my education and pursue my dreams, whatever they may be, and for this I am forever grateful. I would like to thank my mother for her unconditional love and support; and I would especially like to thank my father for opening my eyes to the exciting world of science at an early age (with dry ice and $E=MC^2$) and for introducing me to engineering research at Carbomedics. I would also like to thank my brother for his creativity, which is a perpetual inspiration, and for all of his scientific questions that have helped keep me, and Dr. Wu, on our toes. I am also very appreciative of Dick Benson for his support, encouragement, and for being my personal “agent” in the scientific world. I would like to extend my gratitude to my Tia July for always believing in me and encouraging me, and for her hospitality during my stay in Mexico while I conducted research experiments at UNAM. I give a special thanks to my cousin Danny for his help “juggling” experiments on Na_xCoO_2 samples and his help coordinating proper job interviewing attire. Most importantly, I would like to thank my dear Rose for always being so supportive, helping me prepare for presentations, filling me with confidence with all of her encouragements, and for lighting up my world with her smile and laughter.

ROMAN CAUDILLO

The University of Texas at Austin

August 2007

Magnetic, Thermoelectric, and Electronic Properties of Layered Oxides and Carbon Materials

Publication No. _____

Roman Caudillo, Ph.D.

The University of Texas at Austin, 2007

Supervisors: John B. Goodenough

Miguel Jose-Yacamán

The structure and physical properties of layered oxides and carbon materials were studied. Two layered carbon materials were studied: carbon nanotubes (CNTs) synthesized by electron irradiation from amorphous carbon *in situ* in a transmission electron microscope (TEM) and a carbon and silver nanocomposite consisting of graphitic carbon nanospheres encapsulating Ag nanoparticles. In the CNT experiments, the effect of electron irradiation in the TEM is shown to alter drastically their structure and properties, even being able to transform amorphous carbon into a CNT. This suggests a possible alternative synthesis technique for the production of

CNTs, in addition to providing a method for tailoring their properties. The structure and magnetic properties of the carbon and silver nanocomposite was characterized with x-ray diffraction, scanning and transmission electron microscopy techniques, and magnetic susceptibility measurements with a superconducting quantum interference device (SQUID) magnetometer. While the sp^2 bonding gives a graphene sheet its mechanical properties, the p_π electrons are responsible for its electronic and magnetic properties. In a flat graphene sheet the p_π electrons are itinerant, but in a narrow p_π band. The introduction of curvature to the graphene sheets that encapsulate the Ag nanoparticles is demonstrated to narrow the p_π band sufficiently to result in “ferromagnetic” behavior. A model that is able to explain spin localization and ferrimagnetic spin-spin interactions in graphitic materials with positive curvature is presented.

Layered oxides from the family of the P2 Na_xCoO_2 structure were synthesized and their properties studied. Na_xCoO_2 has a rich phase diagram ranging from a promising Na-rich thermoelectric composition to the hydrated Na-poor composition $\text{Na}_{0.33}\text{CoO}_2 \cdot 1.3\text{H}_2\text{O}$ that is superconductive. Intermediate to these two Na compositions exists an insulating phase with $x \approx 0.5$ that presents a variety of interesting structural, magnetic, thermoelectric, and electronic behavior. Investigations of Na_xCoO_2 that probe the role of H_2O in the superconductive $\text{Na}_{0.33}\text{CoO}_2 \cdot 1.3\text{H}_2\text{O}$ are presented and conclude that H_2O plays a more active role than a passive lattice spacer. The relationship between Na ordering and an interesting magnetic behavior observed with $\chi(T)$ measurements of annealed Na_xCoO_2 and $\text{Sr}_{x/2}\text{CoO}_2$ samples is determined and found to correspond to a (2a x 2a) superstructure. The properties of Na_xCoO_2 ($x \approx 0.5$) are reviewed and thermoelectric $S(T)$ measurements are made in order to develop a model that is able to explain the salient features of the Na_xCoO_2 ($x \approx 0.5$) phase.

Contents

Acknowledgments	v
Abstract	viii
List of Tables	xiii
List of Figures	xiv
Chapter 1 Introduction	1
1.1 Comparison of Layered Oxides and Layered Carbon Materials	1
1.2 Purpose of Dissertation	6
1.3 Dissertation Overview	10
Part I: Carbon Layered Materials	15
Chapter 2 CNT <i>in-situ</i> TEM synthesis	15
2.1 Introduction	15
2.2 Experimental	16
2.3 Results and discussion	19
Chapter 3 Carbon-encapsulated Ag NPs exhibiting ferromagnetic properties	25

3.1	Introduction	25
3.2	Experimental Details	27
3.2.1	Synthesis	27
3.2.2	Structural Characterization	28
3.2.3	Magnetic Behavior	34
3.2.4	Trace Metal Analysis	42
3.3	Discussion	44
3.4	Conclusions	55
3.5	Observation	56
Part II: Layered Oxides		59
Chapter 4 Na_xCoO_2 and superconductive $\text{Na}_{0.33}\text{CoO}_2 \cdot 1.3\text{H}_2\text{O}$		59
4.1	General Overview	59
4.2	The role of structure, Na content, and Co valence	61
4.3	Role of Doping and Dimensionality in $\text{Na}_{0.33}\text{CoO}_2 \cdot 1.3\text{H}_2\text{O}$	67
4.3.1	Introduction	67
4.3.2	Experimental Section	68
4.3.3	Results and Discussion	69
4.3.4	Conclusions	78
Chapter 5 Na and Sr ordering in Na_xCoO_2 and Sr_xCoO_2		79
5.1	Introduction	79
5.2	Experimental	82
5.2.1	Synthesis	82
5.2.2	Characterization	82
5.3	Results and Discussion	83
5.3.1	Structural Analysis	83

5.3.2	Magnetic Behavior	90
5.3.3	Phase segregation	94
5.3.4	Na and Sr ordering and superstructure	97
5.3.5	I ₂ -deintercalated Na-rich Na _x CoO ₂ samples	104
5.4	Conclusions	105
Chapter 6	A model for Na_xCoO₂ (x≈0.5)	107
6.1	Introduction	107
6.2	Experimental	116
6.3	Discussion and Model	118
6.4	Conclusions	127
Chapter 7	Observations and Recommendations	128
7.1	CNT synthesis with lithographic techniques	128
7.2	Magnetic carbon: curvature and electron transfer	129
7.3	STM of Na _x CoO ₂ and charge-ordering	129
7.4	Na _x CoO ₂ as a potential cathode material in a mixed Li-ion Na-ion battery	130
Bibliography		132
Vita		147

List of Tables

1.1	Comparison of Layered Carbon Materials to Layered Oxides	5
3.1	Summary of ICP-MS elemental analysis for Ag-C samples.	43
4.1	Summary of possible Na_xCoO_2 structures.	62
4.2	Summary of Na_xCoO_2 possible spin states.	65
4.3	Results of the Chemical Analysis of Na_xCoO_2 samples.	69
5.1	Summary of lattice parameters and Na or Sr content in Na_xCoO_2 and Sr_xCoO_2 samples.	88
6.1	Co–O distances (\AA) and Bond Valence Sums (BVS) as reported by Williams [109] for Na_xCoO_2 ($x \approx 0.5$).	111

List of Figures

1.1	Schematic examples of Layered Carbon Materials and Layered Oxides	2
1.2	Na_xCoO_2 phase diagram	9
2.1	CNT formation and healing phenomenon in the TEM	18
2.2	CNT fracture in the TEM	21
2.3	Cross-sectional TEM image of a CNT immediately after fracture . .	22
2.4	Ad-atoms on the surface of a CNT in the TEM	23
3.1	SEM images of carbon-encapsulated Ag nanoparticles (unpressed) .	29
3.2	HRTEM image of C-encapsulated Ag nanoparticle and corresponding x-ray diffractogram	30
3.3	TEM images showing physical removal of Ag from carbon nanospheres by electron irradiation	32
3.4	HAADF STEM images of Ag-C samples after Ag removal by irradi- ation and by chemical extraction	33
3.5	SEM image of a 10-ton-pressed Ag-C sample showing coalescence of Ag	33
3.6	SEM images of a 1-ton-pressed Ag-C sample	35
3.7	TEM image of a 1-ton-pressed Ag-C sample	36
3.8	M(T) curves for powder (unpressed) vs. pressed Ag-C samples . . .	36

3.9	M(H) curves for a powder (unpressed) Ag-C sample	38
3.10	$H_c(T)$ experimental curve and mean-field approximation curve estimating a $T_c \approx 425$ K	39
3.11	M(H) curves for a pressed Ag-C sample	40
3.12	Corrected M(H) curves for powder (unpressed) Ag-C sample after subtracting diamagnetic component	41
3.13	$\chi(T)$ curves for powder (unpressed Ag-C sample) showing thermal hysteresis	42
3.14	Schematic illustration showing effect of curvature on p_π electrons . .	45
3.15	Schematic illustration showing α and β sites in graphite	46
3.16	Schematic illustration showing ferromagnetic superexchange interaction	47
3.17	Schematic illustration showing possible spin orientations	51
3.18	Schematic Illustration showing spin orientations in an applied external field	52
4.1	Schematic illustration of Na-ions occupying the Na2-site in the P2 structure	64
4.2	Effect of Na content on c/a ratio in the P2 structure of Na_xCoO_2 . .	70
4.3	Actual Co^{3+} percentage as a function of the Na content.	72
4.4	Schematic diagram showing the $\text{Co}^{4+/3+}$ redox couple pinned at the top of the $\text{O}^{2-}:2p^6$ band.	73
4.5	Evolution of the temperature dependence of thermopower with Na content.	74
4.6	Variation of the thermopower due to water intercalation.	77
5.1	X-ray diffractogram for a typical Na_xCoO_2 parent phase, indexed for $\text{P6}_3/\text{mmc}$ (194) phase	84

5.2	X-ray diffractogram series of 004 peak showing c-axis expansion upon Na deintercalation	85
5.3	C-axis and a-axis lattice parameters as a function of Na content for Na_xCoO_2 samples	86
5.4	Schematic illustration showing that the $\text{Co}^{4+/3+}$ redox couple is primarily of a_1 -orbital parentage.	87
5.5	X-ray diffractograms of 004 peak for Na_xCoO_2 samples and their corresponding $\text{Sr}_{x/2}\text{CoO}_2$ samples after the ion-exchange reaction. . . .	89
5.6	Magnetic Susceptibility $\chi(T)$ ZFC curves for a Na-rich and a Na-poor sample.	90
5.7	$\chi(T)$ ZFC curves for a Na-poor sample and the corresponding Sr-poor sample after ion-exchange.	91
5.8	ZFC and FC $\chi(T)$ curves for a typical Sr-poor sample	92
5.9	ZFC and FC $\chi(T)$ curves for a typical Sr-rich sample	93
5.10	ZFC $\chi(T)$ curves for annealed Na-poor samples and Sr-poor samples. . . .	94
5.11	TGA for a Na-rich and a Na-poor sample	96
5.12	X-ray diffractograms of 004 peak of Na-poor sample before and after annealing.	97
5.13	Electron Diffraction pattern for a Na-rich parent phase	98
5.14	Electron Diffraction patterns for Sr-rich and Sr-poor samples	99
5.15	Electron Diffraction pattern for an annealed Na-poor sample	101
5.16	Schematic of 1/3 occupancy of counter cation sites and corresponding $(\sqrt{3}a \times \sqrt{3}a)$ superstructure	102
5.17	Schematic of 1/4 occupancy of counter cation sites and corresponding $(2a \times 2a)$ superstructure	102
5.18	$\chi(T)$ curves for I_2 -deintercalated samples	105
6.1	Na_xCoO_2 phase diagram	108

6.2	In-plane $\rho(T)$ measurements for Na_xCoO_2 ($x \approx 0.5$) sample (Foo). . .	109
6.3	Schematic of $(2a \times \sqrt{3}a)$ superstructure for Na_xCoO_2 ($x \approx 0.5$) showing the alternating rows of Co1 and Co2 ions.	109
6.4	Schematic showing the Co1 and Co2 ions in Na_xCoO_2 ($x \approx 0.5$) with their nearest Na neighbors.	110
6.5	$S(T)$ and $R_H(T)$ measurements for Na_xCoO_2 ($x \approx 0.5$) sample (Foo). . .	112
6.6	Magnetic susceptibility $\chi(T)$ and electronic resistivity $\rho(T)$ measured by Huang for Na_xCoO_2 ($x \approx 0.5$)	113
6.7	Gasparovic's [30] proposed model for the magnetic order below 88 K in Na_xCoO_2 ($x \approx 0.5$).	114
6.8	Lattice params vs. T for Na_xCoO_2 ($x \approx 0.5$) (Williams).	115
6.9	$S(T)$ for a series of Na_xCoO_2 samples showing that for Na_xCoO_2 ($x \approx 0.5$) there is a crossover from +S to -S at ≈ 75 K	117
6.10	Schematic illustration showing the occupied Na1 and Na2 sites in Na_xCoO_2 ($x \approx 0.5$) with their nearest Co neighbors.	119
6.11	Schematic of a cross-section of Na_xCoO_2 ($x \approx 0.5$) structure showing Na-Co-Na triplets.	119
6.12	Schematic showing the splitting of the $\text{Co}^{4+/3+}$ redox couple due to the Na ordering.	121
6.13	Schematic of structure showing Na-Co-Na triplet bonding orbitals. . .	122
6.14	Schematic of Na order and the proposed magnetic order below 88 K proposed by Williams [109] showing the resulting $(2a \times 2\sqrt{3}a)$ super- structure.	124
6.15	Schematic showing the ground state and excited state for Na_xCoO_2 ($x \approx 0.5$).	126

Chapter 1

Introduction

1.1 Comparison of Layered Oxides and Layered Carbon Materials

Layered materials constitute an interesting class of solids whose 2D nature commonly gives rise to interesting mechanical, magnetic, thermoelectric, and electronic properties that can be investigated for a deeper understanding of the fundamental physics and chemistry of solids. A better understanding of the structure-property relationships can then lead to the intelligent design of materials that can be developed into useful technological applications. The Li-ion rechargeable battery, ubiquitous in today's cell phones, computer laptops, and many other portable electronic devices, utilizes a Li_xCoO_2 cathode and can also use a graphite-based anode; it provides an excellent example of layered materials that have been developed into an important technological application. This dissertation is based on precisely these two families of layered materials, graphite-based carbon materials and layered oxides. Therefore, it will start by describing these two classes of materials.

Carbon layered materials are all based on the graphite structure (see Fig. 1.1). Therefore, a good starting point for discussing layered carbon materials is a sin-

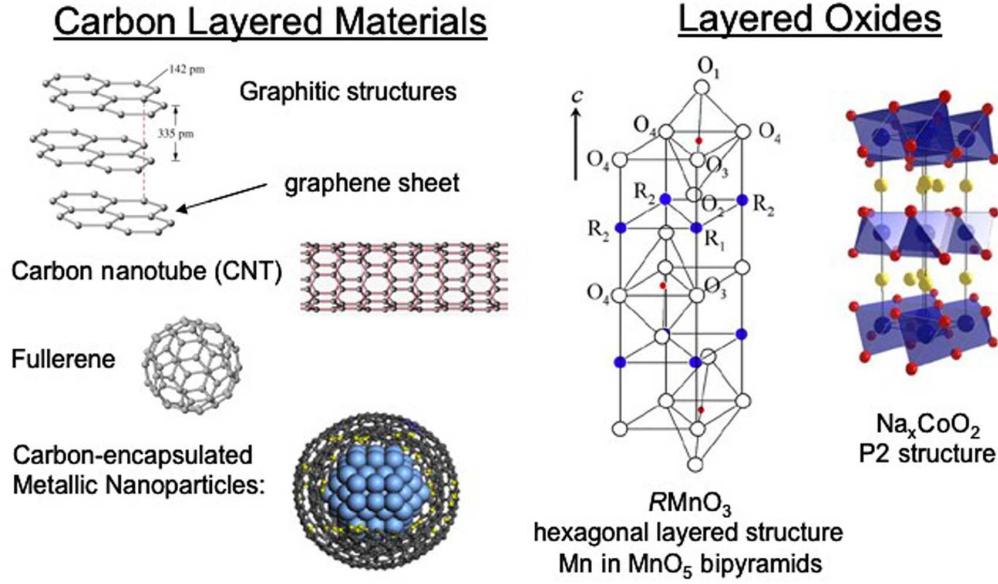


Figure 1.1: Schematic examples of Layered Carbon Materials and Layered Oxides

gle layer of graphite known as a graphene sheet. In graphene, sp^2 σ -bonding and p_π -bonding give strong bonding in the plane, while the electronic properties are dominated by the p_π electrons. Theorists have predicted some unusual properties in single graphene sheets due to an electronic structure where conduction and valence bands touch at discrete points so as to give a linear energy-momentum dispersion relation near those points. Consequently, electrons near the Fermi energy should behave like massless particles and be best described by the relativistic Dirac equation [32]. Quite recently, there has been a lot of excitement in graphene research due to the success of experimentalists in isolating single graphene sheets [80]. This has lead to measurements of an anomalous quantum hall effect in graphene that support their description as massless Dirac Fermions [79, 113, 81].

When one begins to consider multiple layers of graphene sheets, as in graphite, the electronic structure changes and you are no longer dealing with massless Dirac fermions. Instead graphite is a semimetal with enough band overlap to give you

good electronic conductivity from a conduction band of p_π antibonding parentage. As in graphene, sp^2 σ -bonding and p_π -bonding of the graphene sheets gives strong bonding in the plane, but now you also have weak bonding between planes. The p_π electrons in the graphene sheets of graphite are delocalized and give good electronic conductivity. However, there has also been a lot of excitement recently in graphite research due to reports of ferromagnetism in proton-irradiated graphite [95, 57, 36, 27, 35] and carbon nanofoam [86, 83, 87], a nanoporous carbon containing regions of negative curvature. Thus in graphite, it appears that it is possible to push the p_π electrons from itinerant to localized behavior, *e.g.* by the introduction of curvature, and thereby obtain interesting magnetic properties, such as ferromagnetism.

In addition, various carbon nanostructures can be constructed from graphene sheets. The single-walled carbon nanotube (SWCNT) shown in Fig. 1.1 can be thought of as a graphene sheet rolled up into a tube. A multi-walled carbon nanotube (MWCNT) consisting of several graphene sheets is also possible. Similarly a Fullerene consists of a single graphene sheet with the insertion of pentagons in its hexagonal network so as to give it positive curvature and form a closed carbon cage. Nested Fullerenes, sometimes called onions, and carbon-encapsulated metallic nanoparticles are similar structures, but they are made up of several graphene sheets (see Fig. 1.1). Probably the most important differences between all of these structures are the following:

1. Whether they consist of one or more graphene sheets,
2. The manner in which the graphene sheets are rolled up, *i.e.* the details of the introduction of curvature to the graphene sheet, *e.g.* the chirality of a CNT or the type and degree of curvature of the carbon nanostructure, and
3. Whether there is any doping of the graphene sheets, as in the graphite inter-

calation compounds (GICs) YbC_6 and CaC_6 .

Transition-metal layered oxides, on the other hand, contain d electrons having interatomic interactions that can be tuned by adjusting the structure and/or doping to give a variety of magnetic and electronic properties. For example, the RMnO_3 perovskite structure with the smallest rare earth ions adjusts by forming an RMnO_3 hexagonal layered structure shown here that has Mn cations in MnO_5 bipyramids and is of interest for its multiferroic properties. On the other hand, the Na_xCoO_2 structure consists of edge-sharing Co octahedra in CoO_2 sheets that are separated by layers of Na^+ ions in either trigonal prismatic, as shown in Fig. 1.1, or octahedral coordination as in the standard cathode material, Li_xCoO_2 , of Li-ion rechargeable batteries. The amount of Na largely determines the $\text{Co(IV)}/\text{Co}$ ratio of the CoO_2 sheets and can give a large variety of properties including two metallic phases separated by a charge-ordered semiconducting phase, interesting thermoelectric properties, as well as a bilayer hydrated superconducting phase.

These may seem like two disparate classes of materials; however, they are both layered materials and they have numerous similarities. For example, Table 1.1 highlights some of their similarities (as well as their differences). Regarding superconductivity, intercalation of Na-poor Na_xCoO_2 with H_2O molecules results in a bilayer hydrated structure with a greatly increased c-axis, $\text{Na}_{0.33}\text{CoO}_2 \cdot 1.3\text{H}_2\text{O}$, that is superconducting with a $T_c \approx 4$ K. Similarly, in the graphite intercalation compounds (GICs), *e.g.* CaC_6 , intercalation with Ca expands the c-axis and results in superconductivity with a $T_c \approx 12$ K.

The ability of the layered structures to allow for the intercalation of smaller cations is especially useful in the electrodes of rechargeable batteries. Most rechargeable Li-ion batteries today use a graphite-based anode and a Li_xCoO_2 cathode. The large galleries between graphene or CoO_2 sheets are ideal for intercalation and deintercalation of Li^+ ions and the energy difference between the Fermi energies of the

Table 1.1: Comparison of Layered Carbon Materials to Layered Oxides.

	Layered Carbon Materials (<i>s</i> - and <i>p</i> -electron materials)	Layered Oxides (<i>d</i> -electron materials)
Superconductivity	GICs (CaC_6 and YbC_6) K_3C_{60}	$\text{Na}_{0.33}\text{CoO}_2 \cdot 1.3\text{H}_2\text{O}$ High- T_c Copper Oxides
Electrodes	Graphitic Anodes Large galleries allow (de)intercalation	Li_xCoO_2 Cathodes $\text{Co}^{4+/3+}$ redox couple allows for large voltage
Electronic Properties	Curvature takes p_π electrons from itinerant to localized	Na order in Na_xCoO_2 ($x \approx 0.5$) metal \rightarrow semiconductor
Magnetism	Carbon usually diamagnetic curvature/doping can give weak ferromagnetism	Na_xCoO_2 can be Curie-Weiss-like \rightarrow Pauli-like Na order \rightarrow AF coupling

p_π band in graphite and the $\text{Co}^{4+/3+}$ redox couple that can be oxidized and reduced during charging and discharging makes possible the large voltage, and thus high energy density, characteristic of Li-ion batteries.

Both classes of materials are capable of exhibiting both localized and itinerant electron behavior. Carbon materials only have *s* and *p* electrons that usually give strong covalent bonding in broad bands, while layered oxides have *d* electrons that generally give much narrower bands that can accommodate both itinerant and localized electrons. However, this dissertation will show that graphitic carbon materials can also exhibit localized-electron behavior. In the layered carbon materials, the electronic behavior and magnetic properties are most dependent on the curvature of the graphene sheet, while for the Na_xCoO_2 the amount of Na and whether it orders is of primary importance. For the Na_xCoO_2 system, there is a transition from a Curie-Weiss-like behavior in the Na-rich samples, *e.g.* $x \approx 0.7$,^{*} to a Pauli

^{*}Note: However, for $x \approx 1$, Na_xCoO_2 is a nonmagnetic insulator [24].

paramagnetic behavior in the Na-poor samples, *e.g.* $x \approx 0.3$. In between, a Na-ordered ($x \approx 0.5$) phase that is semiconducting contrasts with the metallic Na-rich and Na-poor phases; it exhibits a transition from semiconductor to insulator at 53 K as well as antiferromagnetic coupling of Co^{4+} ions at 88 K. Clearly, these are two very different families of materials, yet with some very interesting parallels.

1.2 Purpose of Dissertation

The main objective of this dissertation is to investigate the effect of structure and electronic doping on the physical properties of layered carbon materials and layered oxides in order to gain a deeper understanding of the fundamental physics and chemistry of solids. For example, the superconductivity in the sodium cobaltate $\text{Na}_{0.33}\text{CoO}_2 \cdot 1.3\text{H}_2\text{O}$ is not well understood and may provide clues to understanding superconductivity in the technologically relevant Cu-oxide high-temperature superconductors (HTSCs) and/or the graphite intercalation compounds (GICs). In addition, the study of layered graphite and cobaltate systems may also provide opportunities to engineer new technologically significant materials such as electrode materials for secondary batteries that are becoming more important considering the increasing demand for energy and the decreasing supply of oil in today's world. A more complete understanding of these and other layered materials can lead to new synthesis techniques for attractive nanomaterials such as the CNT and improved engineering of novel ferromagnetic organic materials and thermoelectric materials.

In layered carbon materials, such as the CNT that exhibits exceptional mechanical properties, the sp^2 -bonded graphene sheets that make up individual tubes are responsible for its robust mechanical properties. The TEM is an indispensable tool in the characterization of important nanomaterials such as the CNT. However, it also imparts significant irradiation effects on nanostructures during viewing. This dissertation shows that the effect of irradiation in a 200 kV TEM can drastically al-

ter the structure and thus properties of carbon nanostructures in the TEM. Indeed, it is shown that the effect of electron irradiation in the TEM on carbon materials can be controlled so as to transform amorphous carbon into a CNT. This suggests the possibility of using electron irradiation of amorphous carbon as a possible alternative synthesis technique for the production of CNTs, in addition to providing a method for tailoring their properties.

While the sp^2 bonding gives a graphene sheet its mechanical properties, the p_π electrons are responsible for its electronic and magnetic properties. In a flat graphene sheet the p_π electrons are itinerant, but in a narrow p_π band. This dissertation will show that the introduction of curvature to a graphene sheet narrows the p_π band and leads to strong correlations that may result in surprising ferromagnetic behavior in graphitic materials. In fact, the characterization of the structure and magnetic properties of a carbon and silver nanocomposite consisting of graphitic carbon nanospheres encapsulating Ag nanoparticles has resulted in a model that is able to explain spin localization and ferrimagnetic spin-spin interactions in graphitic materials with positive curvature.

Similarly, structure has a strong influence on properties in the $RMnO_3$ ($R=Y, Ho, Er, Tm, Yb, Lu$) compounds. Whereas the thermodynamically stable phase for the smaller rare earth ions is a layered hexagonal structure, a metastable orthorhombic perovskite phase can be stabilized by the application of pressure. A subsequent comparison of both structures and characterization with measurements of magnetic susceptibility $\chi(T)$ and thermal conductivity $\kappa(T)$ shows important differences between the two phases and helps explain the suppression of $\kappa(T)$ below T_N in the hexagonal phase with increasing rare-earth ionic radius. In contrast to the Type-A spin-ordered perovskites with large rare-earth ions where T_N is extremely sensitive to rare-earth ionic radius, T_N in the type-E spin-ordered $RMnO_3$ perovskite phase is shown to be essentially independent of rare-earth ionic radius. The transition

from type-A to type-E magnetic order with decreasing rare-earth ionic radius in the perovskite phase is indicative of a competition between ferromagnetic e^1 -O- e^0 interactions and antiferromagnetic t^3 -O- t^3 interactions in the same Mn-O-Mn bonds of the (001) plane where a decreasing Mn-O-Mn bond angle from 155° in LaMnO_3 to 142° in LuMnO_3 increasingly favors the antiferromagnetic interactions [114].

In addition to the importance of structure in determining properties, the cobalt oxidation state in the layered cobalt oxide Na_xCoO_2 is of paramount importance in determining the properties of the material. Carbon materials only consist of s and p electrons while the layered oxides Na_xCoO_2 and RMnO_3 contain transition metal ions that contribute important 3d electrons to the system. In RMnO_3 the Mn^{3+} — Mn^{3+} interactions are through an O^{2-} anion and result in a bandwidth $W < U$ (where W is the Mn d electron bandwidths and U is the on-site electrostatic energy) so that the material is insulating with the Fermi level lying between the $\text{Mn}^{4+/3+}$ redox couple and the $\text{Mn}^{3+/2+}$ redox couple.

On the other hand, the P2 phase of Na_xCoO_2 , which can be stabilized for $0.25 < x < 0.8^{**}$, is mixed-valent; the Fermi level lies within the $\text{Co}^{4+/3+}$ redox couple and itinerant-electron behavior results from direct Co—Co interactions in the ab-plane. Thus in Na_xCoO_2 the Na stoichiometry determines the Co oxidation state and largely determines the electronic and magnetic properties of the system. In addition, the structure is also affected by the Na content and experiences a large c-axis expansion upon deintercalation of Na.

The resulting phase diagram is a rich one (see Fig 1.2). Na-rich compositions, especially $x \approx 0.7$, appear to be promising thermoelectric materials. Na-poor compositions pull in H_2O into their structure to form a hydrated bilayer structure $\text{Na}_{0.33}\text{CoO}_2 \cdot 1.3\text{H}_2\text{O}$ that is superconducting at low temperatures and may help better understand the high-temperature Cu-oxide superconductors. The $x \approx 0.5$

^{**}For $0.8 < x < 1.0$ several works show that Na_xCoO_2 phase separates into a magnetic $x \approx 0.8$ and nonmagnetic, insulating $x = 1.0$ phase [41, 24].

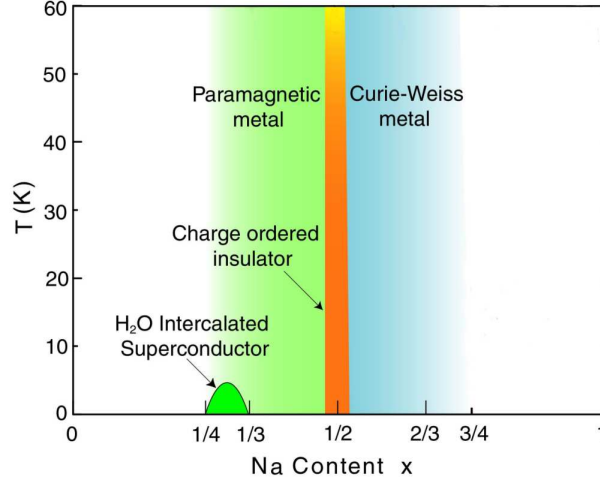


Figure 1.2: Na_xCoO_2 phase diagram (from [29])

composition exhibits Na ordering that changes the symmetry of the crystal from hexagonal to orthorhombic and increases the resistivity by an order of magnitude. In contrast to the metallic ($d\rho/dT > 0$) behavior observed for the other compositions, the resistivity is flat to semiconductor-like ($d\rho/dT < 0$) for Na_xCoO_2 ($x \approx 0.5$) with a transition to a more insulating state occurring at $T_{MIT} = 53$ K. The origin of the “MIT” transition in the $\text{Na} \approx 0.5$ samples is not clear although there is growing evidence that charge ordering or a CDW in the Co array may play an important role. In addition, there exist magnetic transitions at $T_N = 88$ K and 53 K. Because of the richness of the Na_xCoO_2 phase diagram, the focus of the section on oxides in this dissertation is on the anhydrous Na samples, *i.e.* the non-superconducting samples.

The primary objectives in the investigation of Na_xCoO_2 were (1) determining the role of H_2O in the superconductivity of $\text{Na}_{0.33}\text{CoO}_2 \cdot 1.3\text{H}_2\text{O}$, (2) determining the origin of the magnetic behavior in annealed Na_xCoO_2 samples, and (3) developing a model to explain the “MIT” in the $\text{Na} \approx 0.5$ samples by using structural, magnetic, thermoelectric, and transport measurements reported in the literature and made

on polycrystalline samples synthesized by a combination of solid state and soft chemistry (oxidative deintercalation) techniques.

1.3 Dissertation Overview

This dissertation is organized into two main parts. Part I presents new research on layered carbon materials while Part II investigates layered oxide materials. More specifically, Part II investigates the layered cobaltates $A_x\text{CoO}_2$ ($A=\text{Na}, \text{K}, \text{Sr}$). The research on the layered oxides is principally focused on Na_xCoO_2 although some results for the substitution of Na with K, an isovalent atom of different size, and with Sr, an aliovalent ion of different charge, are also presented. For the carbon layered materials in Part I, the dissertation includes a study of two nanostructured graphitic carbon materials, namely carbon nanotubes (CNTs) and carbon nanospheres encapsulating Ag nanoparticles.

Layered carbon materials are based on the graphite structure, where graphene sheets consisting of hexagonally-packed sp^2 -hybridized carbon atoms make up strongly bonded carbon layers with weak interlayer bonds. The strong s and p in-plane bonding can result in exceptional mechanical properties such as occurs in the CNT, a structure consisting of graphene sheets rolled up so as to make tubes of sp^2 -bonded carbon. On the other hand, the p_π electrons determine the electronic properties of the layered carbon materials and are strongly influenced by the curvature of the graphene sheets.

Chapter 2 presents a study of the irradiation effects on carbon in the transmission electron microscope (TEM) that shows how a carbon nanotube (CNT) can be synthesized from amorphous carbon *in-situ* in the TEM by electron irradiation [15]. Whereas most CNT synthesis is by standard techniques, such as arc discharge, laser ablation, or chemical vapor deposition (CVD) [94], this synthesis method creates a large number of carbon ad-atoms that, after some critical amount of radi-

ation, act to restore the system by reconstructing the carbon film. The behavior of ad-atoms can be controlled by adjusting the current density in the microscope, suggesting that carbon nanomaterials can be tailored by electron irradiation.

Chapter 3 explores the structure and magnetic properties of a silver-carbon nanocomposite consisting of silver nanoparticles encapsulated by graphitic carbon nanospheres [14]. In contrast to the layered cobalt oxides that contain d electrons, layered carbon materials consist only of s and p electrons that normally give broad bands and diamagnetic or Pauli paramagnetic behavior. However, recent research [87, 27] has shown that ferromagnetism intrinsic to graphitic carbon materials is a real possibility. In order to better understand the origin of ferromagnetism in carbon materials, and more generally s and p electron systems, magnetic measurements were taken of the Ag and C nanocomposite, in its powder form; they showed weak ferromagnetic behavior up to at least room temperature, from which we estimated magnetic ordering up to 425 K. Chemical analysis with EDS and ICP-MS indicated that there are no magnetic contaminants in the sample; therefore, we attributed the ferromagnetism to the carbon nanospheres and proposed a model for the observed magnetism.

Part II on the layered oxides consists of Chapters 4 through 6, which introduce and explore various aspects of the layered cobaltates. In Chapter 4, an overview of the Na_xCoO_2 system is given, with particular attention given to the P2 structure that, for Na-rich compositions, gives a potentially technologically useful thermoelectric material and, for a small range of Na-poor compositions, gives an intriguing hydrated superconductor $\text{Na}_{0.33}\text{CoO}_2 \cdot 1.3\text{H}_2\text{O}$. The possible structures of the Na_xCoO_2 system are reviewed and compared with the O3 structure of the Li_xCoO_2 system before focussing on the P2 structure. Synthesis of thermodynamically stable structures by hard chemistry routes as well as fine tuning of Na content by soft chemistry oxidative deintercalation techniques that are able to extend the

P2 structure for a wide range of Na contents in a metastable structural state are discussed. The effect of Na content on structural parameters as well as electronic doping and thermoelectric power properties are discussed. Results obtaining a complete analysis of the formal $\text{Co}^{4+/3+}$ oxidation state in Na_xCoO_2 , in the interval $0.31 \leq x \leq 0.69$, are given. Iodometric titration and thermoelectric power indicate that a direct relationship between the Na content and the amount of Co^{3+} cannot be established for the powder Na_xCoO_2 samples measured in our experiments. Creation of a significant amount of oxygen vacancies appears to accompany Na-ion deintercalation, keeping the formal valence at 3.45^+ for $x \leq 0.45$. In addition, thermoelectric power data reveal important differences between the hydrated (superconducting) and nonhydrated (nonsuperconducting) samples that suggest that water plays an important “chemical” role beyond that of a spacer between the CoO_2 layers [9].

Chapter 5 focuses on the magnetic properties of Na_xCoO_2 , in the interval $0.31 \leq x \leq 0.78$, with measurements of $\chi(T)$ taken with a SQUID magnetometer. Samples of $\text{Sr}_{x/2}\text{CoO}_2$ were made by topotactic substitution of Na with Sr from a Na_xCoO_2 parent phase. An interesting magnetic transition appears in the $\chi(T)$ curves of the $\text{Sr}_{x/2}\text{CoO}_2$ samples and also of annealed Na-poor Na_xCoO_2 samples. In order to investigate the origin of the magnetic transition in the annealed Na_xCoO_2 samples, TGA measurements of Na_xCoO_2 samples were performed; they show a phase segregation of Na-poor samples into a Na-rich phase and Co_3O_4 . The Na-rich phase is compared with samples deintercalated independently using I_2 , and the approximate composition of the Na-rich phase that shows the magnetic transition is thus determined. Results indicate that for Na-poor samples, Na_xCoO_2 is unstable and undergoes phase segregation at low temperatures. The counter-cation ordering of both the $\text{Sr}_{x/2}\text{CoO}_2$ samples and the annealed Na-poor Na_xCoO_2 samples was probed with electron diffraction in a TEM, and the magnetic behavior is shown to

originate from the formation of a (2a x 2a) superstructure rather than from the phase segregation or ion substitution itself.

Chapter 6 focuses on the $x \approx 0.5$ Na_xCoO_2 samples. It is well-known that the $x \approx 0.5$ samples exhibit Na ordering at room temperature that changes the symmetry of the system from hexagonal to orthorhombic. At lower temperatures, the Na_xCoO_2 ($x \approx 0.5$) samples exhibit an antiferromagnetic transition at 88 K, and at 53 K a sharp increase in the resistivity that has been referred to as a “MIT” although it is more accurately a semiconductor-insulator transition. On the other hand, there are few reports in the literature on the thermoelectric power, which experiences a crossover from positive to negative values between T_N and T_{MIT} ; no explanation has been offered to account for the change in sign in the thermopower of these samples. Therefore, Na_xCoO_2 ($x \approx 0.5$) and proximal composition samples were synthesized, their Na content was determined with ICP-MS, and their thermoelectric power was measured from 300 K down to 12 K in order to complement the experimental results published in the literature and develop a model that accounts for the crossover in sign in the thermoelectric power as well as the behavior of the other observed properties.

Finally, Chapter 7 makes some observations and recommendations for future experiments on these two families of layered materials. In the final section, a connection is made between the research presented on Na_xCoO_2 and a technologically relevant application by discussing the expected performance of Na_xCoO_2 as a cathode material in a rechargeable battery that uses a Li-ion electrolyte.

Part I

Carbon Layered Materials

Chapter 2

CNT *in-situ* TEM synthesis

2.1 Introduction

*Carbon nanostructures such as the fullerene [54] and carbon nanotubes (CNTs) [44] have been primarily studied by transmission electron microscopy (TEM); for this reason, considerable research into the effects of electron irradiation has been conducted [7]. A CNT synthesis method reported by Troiani *et al.* [106] provides an ideal opportunity to study a single-walled carbon nanotube (SWCNT) under irradiation conditions. In this method two through-holes are created in an amorphous carbon film by electron-beam irradiation in a TEM. A thin graphitic fiber forms in between the two holes and is narrowed until forming a SWCNT [106, 63]. The hole creation and narrowing of the graphitic fiber involves the formation of a large quantity of ad-atoms with high mobility. After some critical amount of irradiation damage is accumulated in the graphitic periphery of the holes, the ad-atoms return to the holes, resulting in a reconstruction of the amorphous carbon film.

Previous irradiation studies of carbon nanostructures indicate that knock-on atom displacements are of primary importance as they can result in displacement

*This chapter was published in [15]

cascades, sputtering, and stable interstitial-vacancy pair formation [7]. For example, the collision of an energetic particle, such as an electron in the TEM, with a carbon atom in a SWCNT can result in the displacement of the carbon atom. If the incident energy of the electron is high enough, a vacancy is created and the displaced atom can either leave the tube entirely and be lost to the vacuum or displace other atoms by knock-on collisions. If the energy of the displaced atom is low, these atoms can adsorb onto the tube walls as ad-atoms, where they assume the role of interstitials in the SWCNT [50, 51, 52, 53]. While vacancies in a SWCNT and in other graphitic structures are considered to be immobile [78], it has been observed that ad-atoms can migrate along the tube surface and recombine with vacancies in a self-healing process at elevated temperatures ($> 300^{\circ}\text{C}$), while at lower temperatures the ad-atoms remain mobile but are less likely to recombine with the vacancies [8]. This chapter describes a reconstructive transformation phenomenon in irradiated carbon whereby ad-atoms persist for long periods of time and act to restore the system upon reaching a critical amount of accumulated irradiation damage in a process that is referred to as healing.

2.2 Experimental

SWCNTs were constructed from an amorphous carbon film by using electron-beam irradiation in a JEOL 2010F field emission gun TEM. Figure 2.1a shows the graphitic fiber formation schematically, and figure 2.1b-g shows the overall experiment and healing phenomenon as we observe it in the TEM. Under the action of high current densities in the TEM (highly condensed beam), holes are opened in a carbon film so as to form a thin graphitic bridge separating them (Fig. 2.1a,b). The beam is spread to soft irradiation conditions, *i.e.* normal current density observation values, and the thin graphitic bridge is narrowed until forming a SWCNT (Fig. 2.1c). Due to knock-on displacements, ad-atoms are created and are observed to combine and

form small strips (ad-strips) around the periphery of the holes. These ad-strips are observed to be mobile, and after a certain threshold of irradiation damage is reached, the carbon undergoes a reconstructive transformation consisting of the returning of the ad-strips and ad-atoms to the holes (Fig. 2.1d). This results in an accumulation of amorphous carbon around the graphitic bridge and periphery of the holes (Fig. 2.1e). The holes close very quickly (1-2 minutes) at the beginning of the healing process (Fig. 2.1f). In some cases, enough ad-atoms return to completely close the holes (Fig. 2.1g). After closing of the holes, subsequent condensations of the electron beam on the zones where a hole has closed are not able to re-open holes as easily, suggesting that the reconstructed amorphous carbon has somehow changed the nature of its bonds.

The irradiation conditions are drastically different during the hole formation and the bridge-thinning portions of the experiment. In order to understand the healing, it is important to understand first the irradiation conditions and effects occurring during (i) hole formation and (ii) thinning of the graphitic bridge.

(i) *Hole formation:* Following the synthesis method reported by [106], holes are formed by 200 keV electron irradiation in a 20-30 nm amorphous carbon film containing Au nanoparticles of ~ 2 nm. By highly condensing the electron beam beyond imaging values, current densities greater than 1000 A/cm^2 are reached at the sample, and the radiation dose is sufficiently high to create through-holes in the carbon film. The amorphous carbon around the periphery of the holes as well as in the bridge separating the two holes is observed to graphitize.

(ii) *Bridge thinning:* The bridge thinning portion of the experiment commences once the holes are formed and a thin graphitic fiber separates them. The beam is then spread to imaging conditions of current densities between $0.1\text{-}100 \text{ A/cm}^2$. During this phase, there is a size enlargement of the holes and a subsequent narrowing and lengthening of the bridge structure.

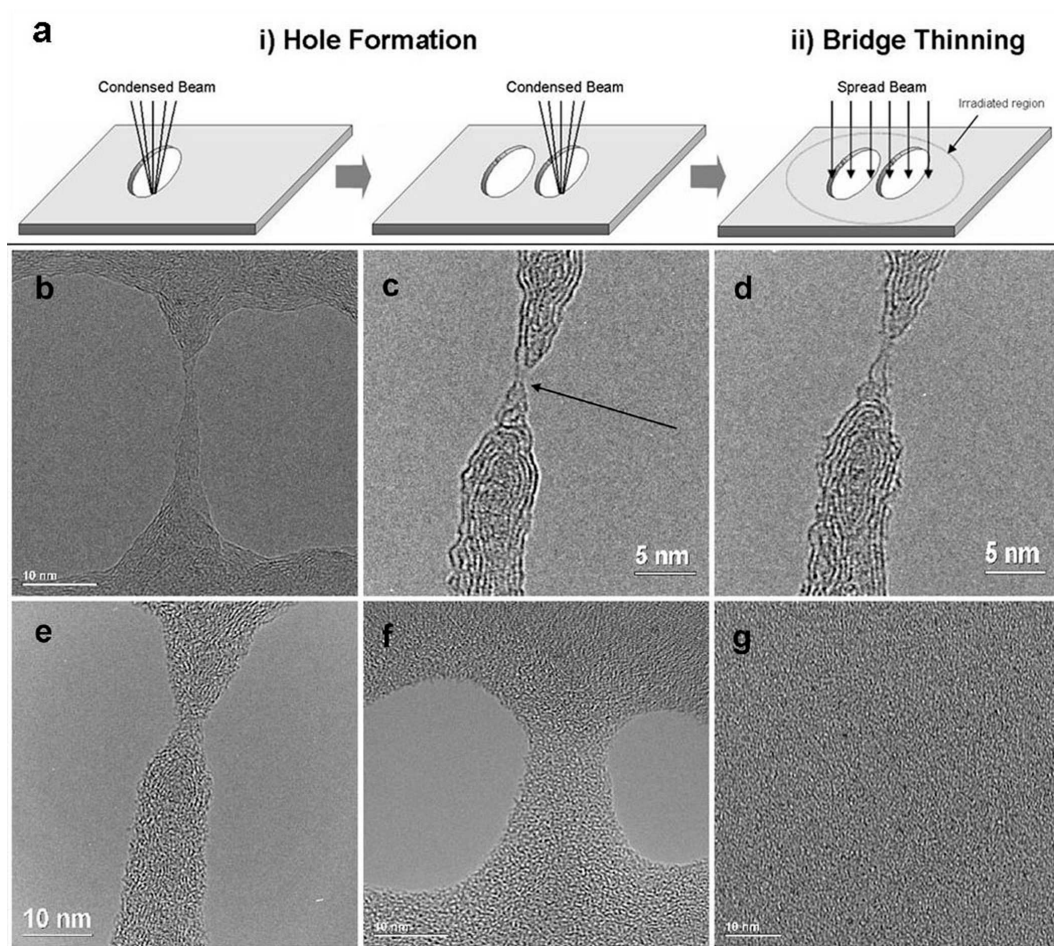


Figure 2.1: Carbon nanotube formation and healing phenomenon. (a) Schematic illustration of hole formation by highly condensed electron beam, and bridge-thinning during soft irradiation (spread beam) condition (irradiated region is shown). (b-g) Sequence of TEM images depicting healing phenomenon. (b) Low magnification image showing two holes in the carbon film separated by a graphitic bridge. (c) High magnification image of graphitic bridge that has been narrowed to the point of forming a SWCNT at its neck (signalled by arrow). (d) High magnification image of the beginning of the healing process, showing graphitic bridge with ad-strips and ad-atoms visible along its edges. (e) High magnification image showing a rapid accumulation of amorphous carbon around the graphitic bridge and periphery of the holes. (f) Low magnification image showing the rapid closing of the holes. (g) Image of the fully reconstructed film after healing process is completed and the holes have completely closed.

2.3 Results and discussion

During the hard irradiation conditions occurring in the first portion of the experiment, holes are created in the carbon film via radiation damage such as sputtering and knock-on atom displacements. However, it should be emphasized that during the hole formation process, some of the displaced atoms are not lost to the vacuum but rather are adsorbed onto the carbon film surface, presumably around the periphery of the holes.

The amorphous carbon around the periphery of the holes as well as in the bridge separating the two holes graphitizes due to radiation-induced self-organization. The phase transformation from amorphous carbon to graphitic carbon is possible due to self-organization processes occurring during irradiation. The irradiation of the amorphous carbon film creates vacancy-interstitial pairs, but unlike in a SWCNT or in graphitic structures, vacancies are mobile in amorphous carbon and are therefore able to migrate and eliminate energetically high regions, or disordered regions, thus leading to graphitization [78].

During the bridge-thinning portion of the experiment, we postulate two mechanisms working simultaneously to achieve the narrowing of the bridge structure under the soft irradiation conditions present in the TEM: (1) deformation in response to an axial stress being applied to the bridge due to a contraction of the film and (2) atom displacements due to irradiation occurring in the bridge, resulting in the creation of vacancies and mobile ad-atoms, followed by a diffusion of the ad-atoms to the center region of the bridges where they reconstruct the amorphous carbon into graphitic carbon.

The carbon undergoes a contraction due to graphitization caused by the afore-mentioned self-organization irradiation process. The higher density of graphite over amorphous carbon causes a contraction in the film, which applies an axial tension to the bridge structure. The graphitic fiber responds by undergoing a series of

deformations in a narrowing process that ultimately results in a neck being created somewhere along the bridge and a SWCNT being formed at the neck. The contraction is facilitated by the catalytic effect of the metallic nanoparticles present in the film. The mechanism by which Au nanoparticles catalyze the carbon transformation is not well-understood, but their catalytic effect was verified experimentally by conducting the synthesis method without the presence of Au nanoparticles and observing a much less pronounced contraction in the film as well as an observable difference in the amount of graphitized carbon.

The thinning of the graphitic fiber necessarily involves a diffusion of carbon atoms away from the neck region. The experiment was conducted close to room temperature, which under the given irradiation conditions creates vacancies and mobile ad-atoms. The ad-atoms diffuse away from the neck region to allow the graphene sheets to reconstruct into a SWCNT. This process can occur by elimination of dangling bonds and Stone-Wales transformations, leading to reconstruction and dimensional changes [1]. Vacancy clustering likely leads to brittle fracture, whereas atomic rearrangements lead to plastic fracture.** As speculated by earlier irradiation studies [1], the limiting case of surface reconstruction should involve the formation of a single chain of carbon atoms. Troiani *et al.* [106] and Marques *et al.* [63] have verified carbon chain formation for short lengths of time (seconds) both experimentally and through simulations. In contrast, this work reports the formation of a single chain of carbon atoms that was observed to be stable for five minutes prior to increasing the current density and inducing fracture (Fig. 2.2b).

Our proposed mechanism suggests that higher current densities at the sample should cause greater graphitization in the surrounding carbon film, thus imparting a larger axial stress to the bridge as well as enhancing the bridges ability to respond by deformation processes that are facilitated by the presence of irradiation-induced

** Here plastic fracture refers to the formation of a neck and not necessarily to dislocation motion.

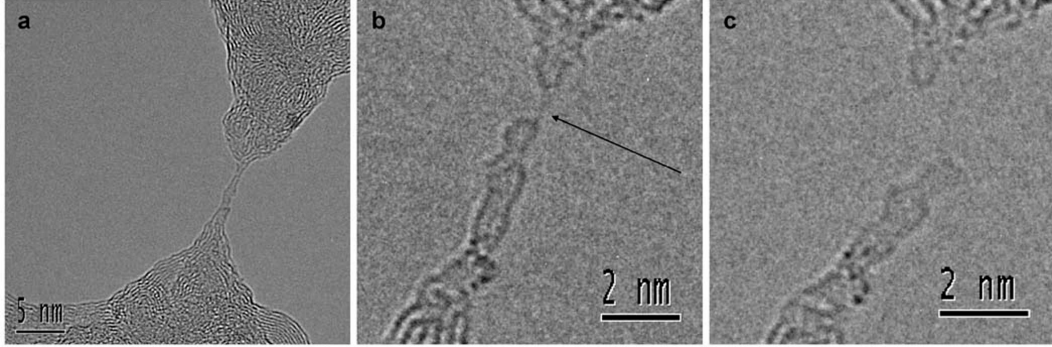


Figure 2.2: Sequence of TEM images depicting plastic fracture. (a) A SWCNT is formed in the neck region of the graphitic bridge separating two holes. (b) The SWCNT deforms in response to axial tension and irradiation damage, forming a single chain of carbon atoms of nearly 1 nm in length that remained stable for 5 minutes (signalled by arrow). (c) The bridge fractures at the chain of carbon atoms upon increasing the current density.

vacancies. This prediction is in fact what we observe experimentally. Current densities greater than 20 A/cm^2 result in further thinning of the graphitic fiber until forming a SWCNT, while low current densities ($0.1\text{-}10 \text{ A/cm}^2$) tend to stabilize the graphitic bridge structure. For current densities greater than 75 A/cm^2 , the SWCNT is seen to undergo brittle fracture. For moderate current densities ($10\text{-}40 \text{ A/cm}^2$), low strain rates lead to plastic fracture of the SWCNT by nanotube elongation and, eventually, linear carbon chain formation prior to fracture (Fig. 2.2). For the lowest current density conditions ($10\text{-}20 \text{ A/cm}^2$) leading to plastic fracture, carbon chain lifetimes of up to 5 minutes prior to fracture were observed (Fig. 2.2b). It is quite remarkable that it is possible to have amorphous carbon, a graphitic fiber, a SWCNT, and a linear chain of carbon atoms all integrally connected and that such a configuration can remain stable for a considerable amount of time.

While it may not be obvious from the planar view TEM images that the neck indeed consists of a SWCNT rather than, for example, a carbon strip, we were able to obtain cross-sectional TEM images of a bridge immediately after fracture

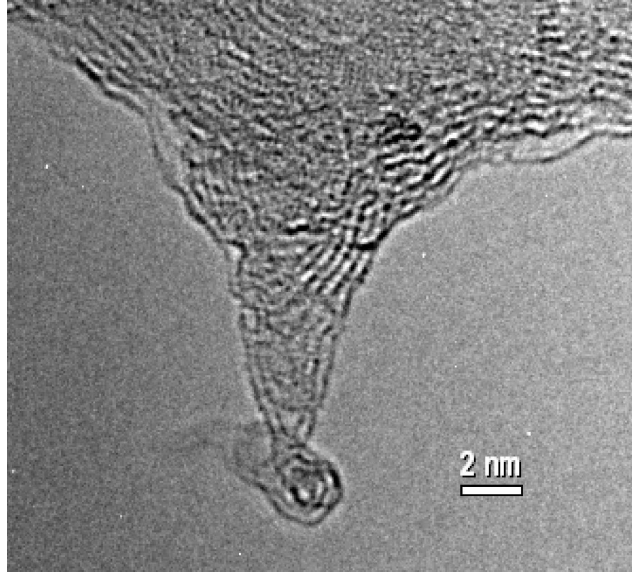


Figure 2.3: TEM images of one side of a bridge that has fractured and bent into the beam, so as to be parallel to the beam direction and thereby provide a cross-sectional view of the bridge structure. The cross-sectional view clearly indicates that the bridge neck consists of a CNT that itself necks into some smaller structure, possibly a CNT of smaller diameter.

that clearly showed the presence of a CNT neck. Figure 2.3 shows one side of a bridge structure that has fractured and bent into the direction of the electron beam, thereby providing a cross-sectional view of a portion of the bridge neck. The structure is clearly not a 2-dimensional carbon strip, but rather a 3-dimensional CNT. In addition, the CNT appears to neck even further at its tip into some smaller structure, possibly a CNT of smaller diameter.

The above discussion is concerned with effects occurring prior to the healing phenomenon; however, they are essential to understanding the healing. Our observations, as well as the proposed mechanism, indicate that some of the atoms displaced during the hole-forming and bridge-thinning process are not lost to the vacuum but rather remain as ad-atoms that diffuse to the amorphous regions. Once some critical accumulated irradiation damage is reached, the ad-atoms try to restore

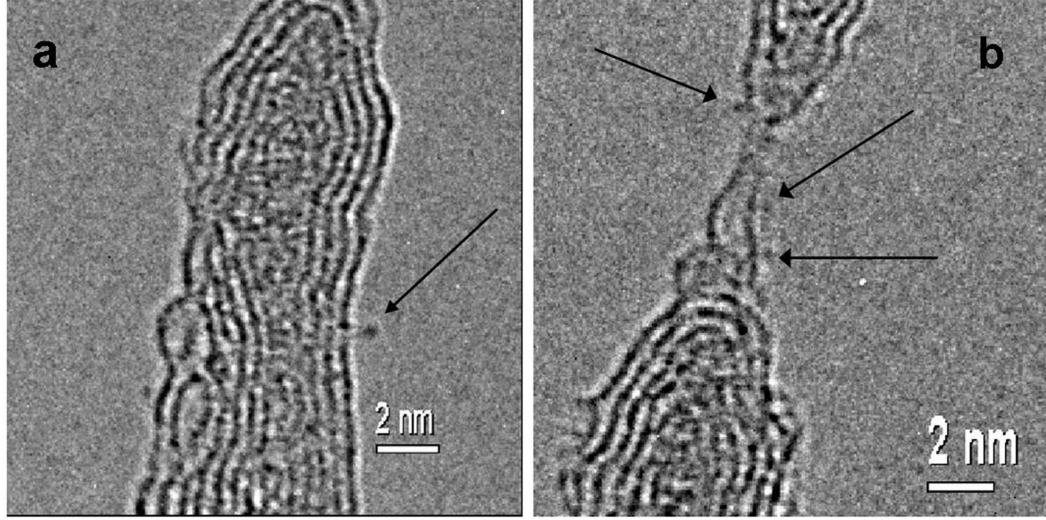


Figure 2.4: TEM images of ad-strips. (a) Ad-strip (signalled by arrow) on the surface of graphitic bridge diffusing rapidly during the healing process. (b) Numerous ad-strips (signalled by arrows) returning to CNT neck during healing process.

the previous state and rapidly diffuse back to the graphitized bridge and periphery of the holes (Fig. 2.4). The observed, sudden pronounced diffusion confirms that at least some of the carbon atoms removed during hole formation and thinning of the graphitic fiber, instead of going to the vacuum become ad-atoms that are able to persist for extended lengths of time, possibly as interstitials in the surrounding amorphous carbon. They likely return to the holes because the heavily graphitized periphery of the holes and bridge region accumulate radiation damage faster than the amorphous regions due to vacancies being relatively immobile in graphite. These graphitic regions are the first to become highly damaged and unstable, and therefore they provide an ideal site for the return of ad-atoms or interstitials.

Our observations agree well with the proposed mechanism and lead one to suggest that the tempo of the experiment can be controlled. Indeed, by adjusting the current density, we were able to form the CNT neck, return to a thicker graphitic bridge structure after irradiation-induced healing occurred, and then again formed

a CNT neck. It is remarkable that the process is somewhat reversible and that its directionality as well as tempo can be controlled. The results indicate that the carbon ad-atoms generated by electron irradiation are very active and can be used to tailor the structure and properties of carbon nanomaterials as well as to induce self-repair. This observation opens up the possibility of developing electron-beam lithography methods for the synthesis and design of carbon nanomaterials and nanodevices.

Chapter 3

Carbon-encapsulated Ag NPs exhibiting ferromagnetic properties

3.1 Introduction

*Recent reports of ferromagnetism in a variety of carbon materials have sparked renewed interest and intense research into the magnetic properties of carbon materials. Organic ferromagnets exhibiting spontaneous magnetization at room temperature were previously reported as early as 1987 [105, 82, 75, 76, 102], but these reports were received with skepticism due to the potential presence of magnetic impurities. As Miller [66] points out, for many magnetic polymers this skepticism proved to be a justified concern. More recently, for example, doubt was cast [60] on the intrinsic origin of the ferromagnetism with a 500 K Curie temperature previously reported in polymerized rhombohedral C₆₀ [61] after detailed chemical analysis revealed considerable iron content [39, 96, 37] in the carbon samples. For C₆₀ compounds, fer-

*This chapter was published in [14]

romagnetism had also been reported in tetrakis(dimethylamino)ethylene-C₆₀ [2, 77] and 3-aminophenyl-methano-C₆₀-cobaltocene [72] below 17 K and 19 K, respectively. On the other hand, ferromagnetic behavior up to 800 K had been reported for polymerized C₆₀ that had undergone photo-assisted oxidation [74].

More recently there have been reports of ferromagnetism in proton-irradiated graphite [95, 57, 36, 27, 35], nanographite [38, 26, 56, 55, 64], graphite containing topographic defects [68], negative curvature Schwarzite-like carbon nanofoams [86, 83, 87, 88, 104], fullerene-related carbons [59, 4, 110, 3, 37, 13], microporous carbon [49], as well as reports of a unique magnetic behavior of carbon nanohorns [5]. However, despite the growing number of carbon-based materials exhibiting ferromagnetic behavior, a clear explanation as to the origin of the magnetic behavior in these materials still needs to be developed. Some research suggests that hydrogen may play an important role in determining the magnetic properties of graphite [27]. On the other hand, the unique magnetic behavior in carbon nanohorns may be explained by the presence of adsorbed oxygen [6]. Still other research points to the importance of edge-states [84] or topographic defects [68] or negative curvature [83] in the graphene sheets for determining magnetic properties. Kopelevich *et al.* [49] speculate that the ferromagnetism in microporous carbon may be attributable to graphitic fragments with positive or negative curvature.

In addition to the search for a more complete understanding of the mechanism of magnetic state formation in carbon and other *s*- and *p*-electron materials, the study of carbon nanomaterials with ferromagnetic properties is also driven by an enormous technological potential in nanotechnology, telecommunications, medicine, and biology. Exciting applications in medicine such as imaging blood flow with magnetic resonance imaging (MRI) machines, treatment of cancerous tumors, and enhanced brain scans have already been discussed [33].

This chapter presents a new class of “ferromagnetic” carbon consisting of

carbon nanospheres encapsulating silver nanoparticles. The Ag-C material in its powder form exhibited ferromagnetic behavior up to at least room temperature, but pressing the powder suppressed the ferromagnetism and instead recovered the expected diamagnetic behavior for a bulk carbon sample. In addition, a peak in the mass magnetization was measured at low temperatures (50–90 K) and was suppressed when measured in the cooling direction. We propose a model that attributes the ferromagnetism to $(sp)^1$ localized spins in the carbon nanospheres and the peak to a first-order spin reorientation with a thermal hysteresis that suppresses the peak when measuring in the cooling direction.

3.2 Experimental Details

3.2.1 Synthesis

The Ag-C nanocomposite was provided by NovaCentrix, Inc.** Silver nanoparticles are synthesized by a pulsed arc-discharge process and stabilized by carbon introduced into the system in the form of a hydrocarbon. Two cylindrical high-purity Ag electrodes are arc-discharged in an inert gas flow such as argon. The arc discharge produces dramatic increases in temperature and pressure, vaporizing some of the Ag electrode and creating a plasma between the electrodes that is carried downstream by the gas flow. Rapid cooling causes Ag nanoparticles to nucleate and grow downstream. A hydrocarbon, *e.g.* acetylene or methane, is introduced into the process and results in a carbon coating on the Ag particles that stabilizes their size between 10 and 40 nm. The carbon-coated Ag nanoparticles are then collected downstream in the form of an easy to manipulate black powder. Large quantities of the material can be produced at high rates (many kgs per hour).

**NovaCentrix, Inc., 1908 Kramer Lane, Building B, Austin, Texas, 78758, USA.

3.2.2 Structural Characterization

The Ag-C sample was structurally and chemically characterized by scanning electron microscopy (SEM), energy dispersive spectroscopy (EDS), x-ray diffraction, and transmission electron microscopy (TEM), including both HRTEM (High Resolution TEM) and high angle annular dark field (HAADF) scanning TEM (STEM). Due to the dramatic differences in the magnetic properties between the unpressed powder samples and the pressed samples, we present a morphological characterization of both sample types. In addition, we demonstrate the ability to remove the Ag nanoparticles from the C nanospheres of the powder samples physically by electron irradiation in the TEM.

Unpressed Powder Samples

The powder sample was first characterized with a spherical aberration (C_s)-corrected JEOL JSM-7700F SEM. Figure 3.1 shows the SEM images of the Ag-C sample at three different magnifications. Here we can see that the sample consists of spherical particles with diameters of approximately 10–40 nm connected in necklace-like structures.

EDS chemical analysis detected both C and Ag in a weight% ratio of 70:30. Figure 3.2 (inset) shows an x-ray diffractogram of the sample confirming the presence of crystalline Ag. Peak broadening from X-ray diffraction gives an average Ag crystallite size of ~ 10 nm, agreeing well with SEM and TEM images. The absence of any X-ray diffraction peaks corresponding to a crystalline carbon phase, *e.g.* graphite, diamond, or fullerenes, might lead one to suggest that all of the carbon present in the sample is amorphous. However, Fig. 3.2 shows a typical TEM image of the sample clearly revealing crystalline order in the carbon surrounding a Ag nanoparticle. The carbon surrounding the Ag nanoparticles is not amorphous, but is instead graphitic although with an increased interplanar spacing of ~ 3.7 Å as

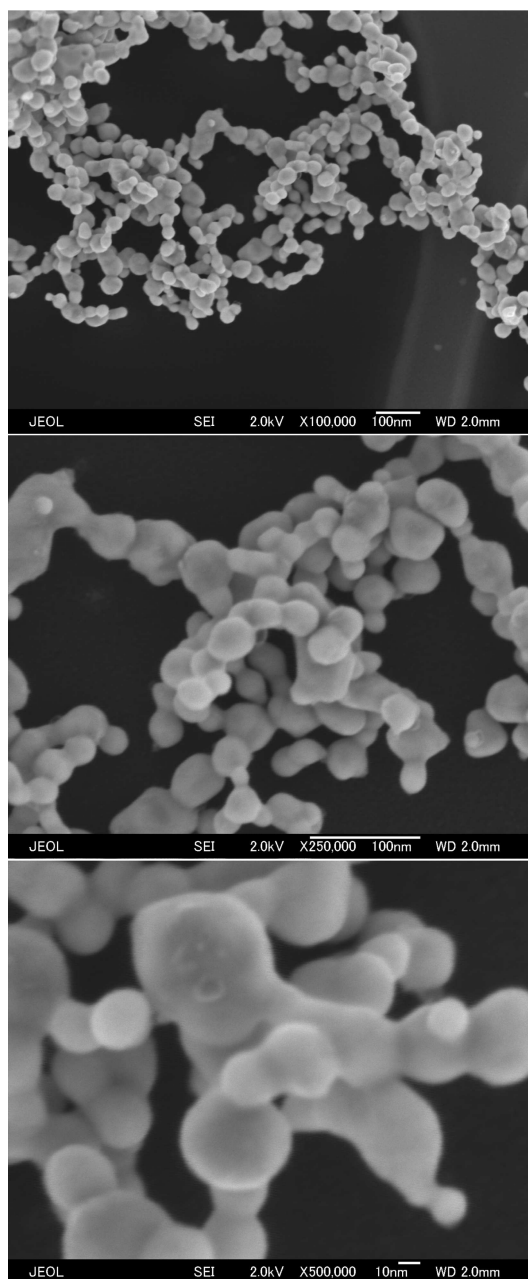


Figure 3.1: SEM images of Ag-C sample at 3 different magnifications, clearly showing that the Ag-C powder consists of spherical particles connected in necklace-like structures.

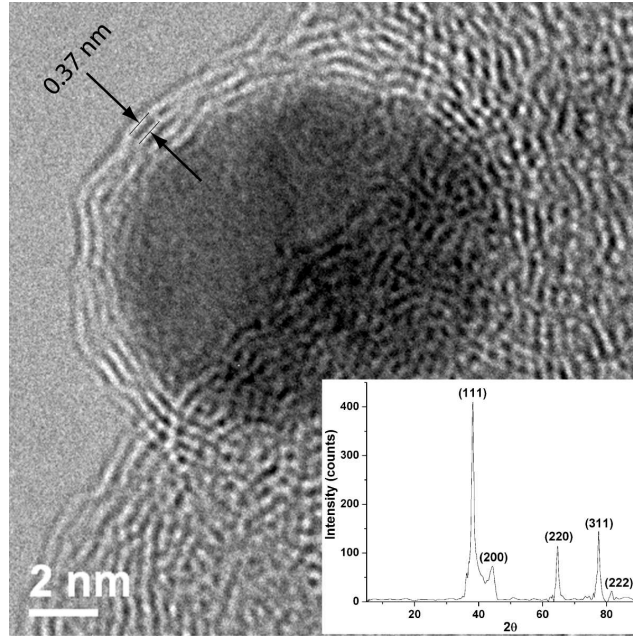


Figure 3.2: HRTEM image showing a Ag nanoparticle (darker contrast) surrounded by graphitic carbon (C nanosphere) showing areas with an expanded interplanar spacing of 3.7 Å. Inset: X-ray diffractogram for Ag-C sample, indexed for the crystalline Ag cubic phase (Fm $\bar{3}$ m). Peak broadening gives an average Ag crystallite size of ~ 10 nm.

compared to the 3.35 Å interplanar spacing expected for bulk graphite.

The very thin dimension of the graphitic carbon coating the Ag nanoparticles compared to the bulkier Ag nanoparticle substrate that it surrounds results in the X-ray diffraction signal from the Ag dominating; any diffraction from the graphitic carbon in the sample is lost in the diffracted X-ray signal. We also observe a large percentage of amorphous carbon in the sample, thus accounting for the larger weight% of C measured by EDS. However, the carbon surrounding the Ag nanoparticles is always observed to be graphitic in the TEM. We refer to these graphitic shells encapsulating the Ag nanoparticles as carbon nanospheres.

Removal of Ag from the Carbon Nanospheres

The Ag can be removed from the C nanospheres either physically by a 200 keV electron beam in the TEM or chemically by acid treatment, *e.g.* with HCl or HNO₃. The physical removal of the Ag provides a better opportunity to study the structure of the C nanospheres and demonstrates their stability.

Figure 3.3 shows TEM images of the sample before and after physical removal of Ag by electron irradiation in the TEM. The Ag was removed by condensing the electron beam on the sample so as to achieve very high current densities at the sample, *i.e.* greater than 250 A/cm². Upon reaching a critical irradiation level, the Ag was observed to leave dramatically its carbon encasing and deposit immediately on the lacey carbon support of the TEM grid. The removal of Ag from the Ag-C nanocomposite left behind the C nanospheres intact, demonstrating their relative stability to the electron beam and revealing their spherical structure.

For chemical removal, the sample was treated with concentrated nitric acid and sonicated for 5 minutes. The product was then filtered with de-ionized water, dried with moderate heating, and then examined in the TEM. Figure 3.4 shows HAADF images comparing the differences in the samples after Ag removal by electron irradiation vs. chemical extraction. In contrast to the images after physical removal of Ag by irradiation, the structure after chemical extraction appears more sponge-like. Unlike the Ag removal by irradiation, the chemical treatment changes the structure of the carbon nanospheres; further measurements were not made on the chemically-treated samples as their structure had been fundamentally altered.

Pressed Samples

Powder samples were pressed in a die into cylindrical tablets of ~5 mm diameter and ~2 mm height by applying up to 10 tons of pressure. All pressed samples (both 1-ton and 10-ton) exhibited a metallic sheen in contrast to the matte-black of un-

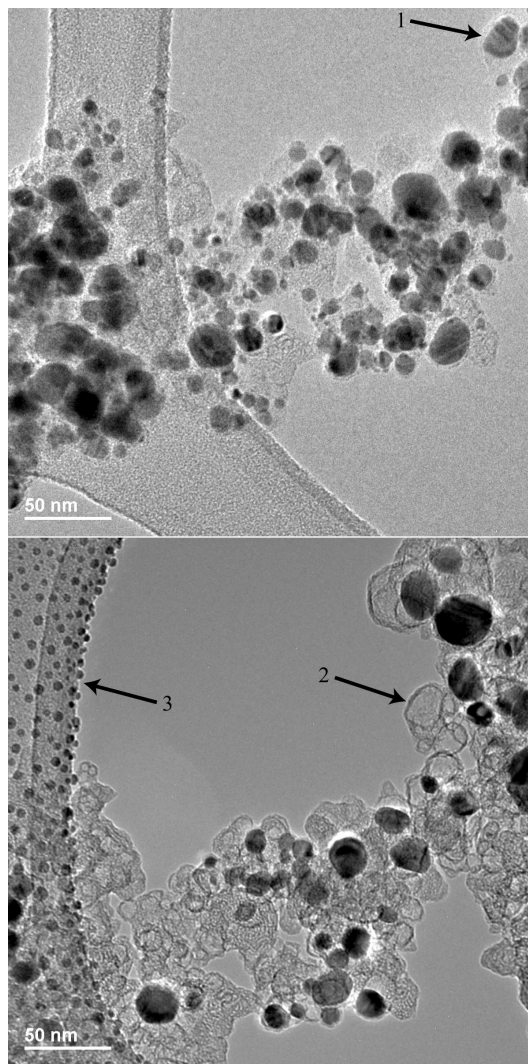


Figure 3.3: TEM images showing the physical removal of Ag from carbon nanospheres by electron irradiation in the TEM. Top panel: Ag-C sample before Ag removal. Lower panel: Same area after removal of Ag from the carbon nanospheres. Notice the smaller size and even distribution of the Ag nanoparticles deposited on the lacey carbon support after removal by intense irradiation (arrow 3) as well as the empty carbon nanospheres that remain after the Ag removal (arrow 2 is same C nanosphere as arrow 1).

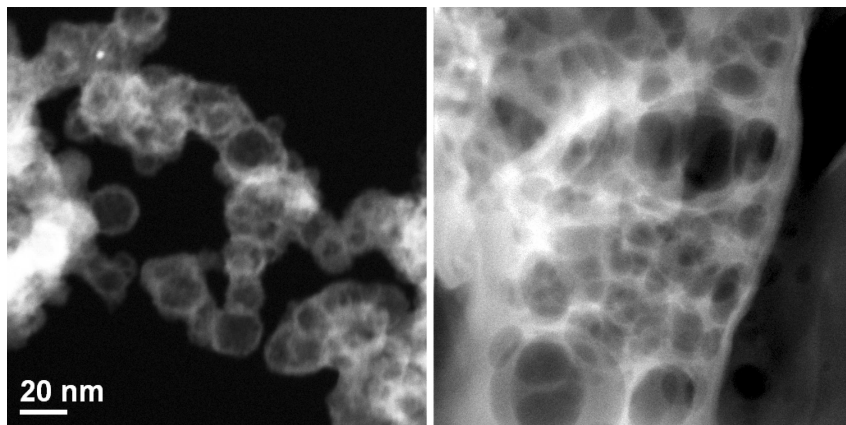


Figure 3.4: HAADF STEM images showing the underlying carbon structure after silver removal by irradiation and by chemical extraction. Left panel: Ag removal by the e-beam in the TEM retains necklace-like structure of C nanospheres. Right panel: Ag removal by chemical treatment with nitric acid fundamentally changes the underlying carbon nanosphere structure to a sponge-like carbon.

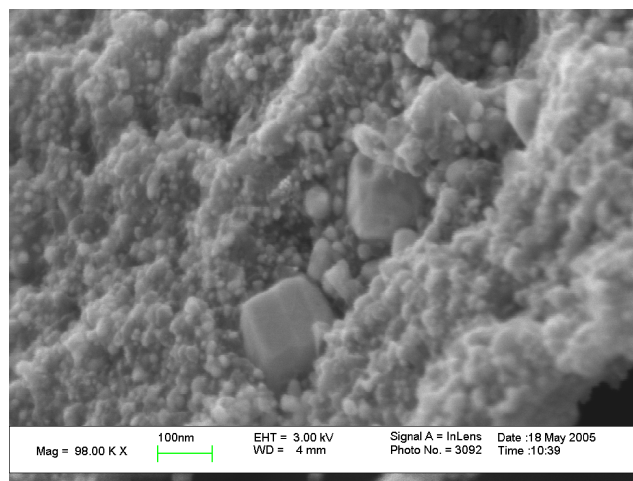


Figure 3.5: SEM image of a 10-ton-pressed Ag-C sample showing the coalescence of some Ag nanoparticles into larger particles that show marked faceting.

pressed powder samples. SEM characterization revealed that pressing with 10 tons changes the underlying structure of the nanocomposite by causing the coalescence of Ag nanoparticles into larger particles that show marked faceting (see Fig. 3.5) in contrast to the spherical geometries seen in the powder samples. On the other hand, samples pressed with ~ 1 ton of pressure showed no changes to their underlying morphology. Figure 3.6 shows an SEM image of a portion of a 1-ton-pressed sample at 4 different magnifications. The images clearly show that the carbon nanospheres are densely packed by the pressing process so as to form slabs. After pressing, they are less necklace-like, but they retain the morphology of carbon-encapsulated Ag nanoparticles, as is evident in the TEM image of Fig. 3.7 taken from the edge of a 1-ton-pressed sample.

3.2.3 Magnetic Behavior

The magnetic properties of the Ag-C powder samples and 1-ton-pressed samples were analyzed with a Quantum Design superconducting quantum interference device (SQUID) magnetometer. Mass magnetization (M_{mass}) vs. temperature (T) curves were measured for samples that were zero-field-cooled (ZFC) and field-cooled (FC). We define

$$M_{\text{mass}} = M/(\text{total mass}),$$

where M is the magnetization in emu and M_{mass} is the mass magnetization. In addition, FC measurements were taken in both directions, *i.e.* upon cooling and warming. The FC measurements taken in the cooling direction are referred to as FCC while those taken in the warming direction are referred to as FCW. For reference, ZFC measurements can only be taken in the warming direction. M_{mass} vs. magnetic field (H), *i.e.* hysteresis curves, were also measured from 2 K up to 300 K, from which the coercive field (H_c) at different temperatures was obtained and then plotted vs. T .

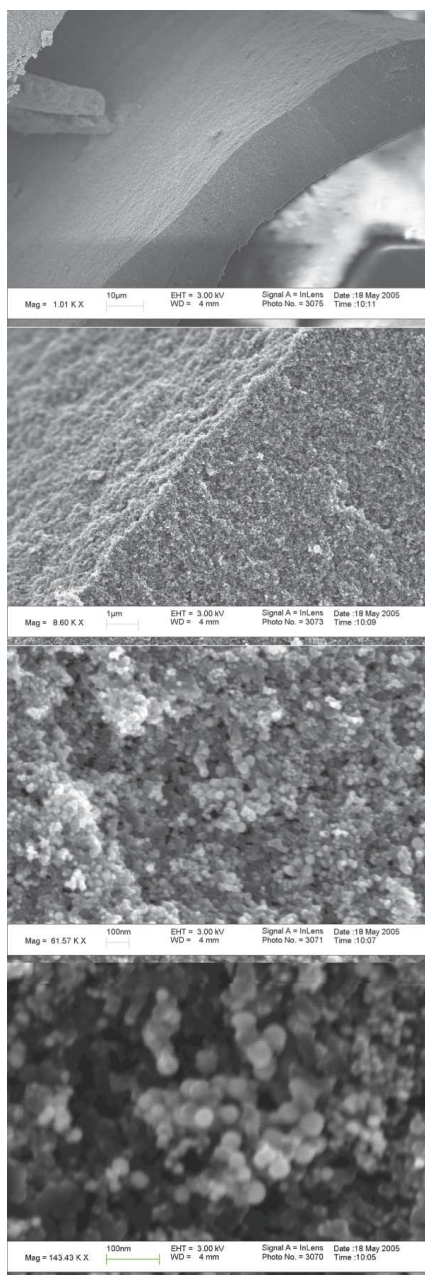


Figure 3.6: SEM images of a 1-ton-pressed Ag-C sample at 4 different magnifications showing that the C-nanospheres densely pack to form slabs and still retain the underlying C-nanosphere morphology.

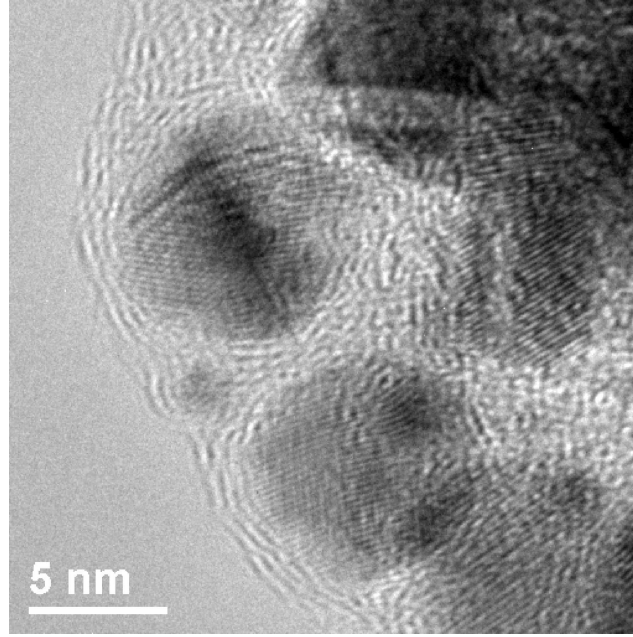


Figure 3.7: TEM image of a 1-ton-pressed Ag-C sample showing that the morphology of the carbon-encapsulated Ag nanoparticles is maintained.

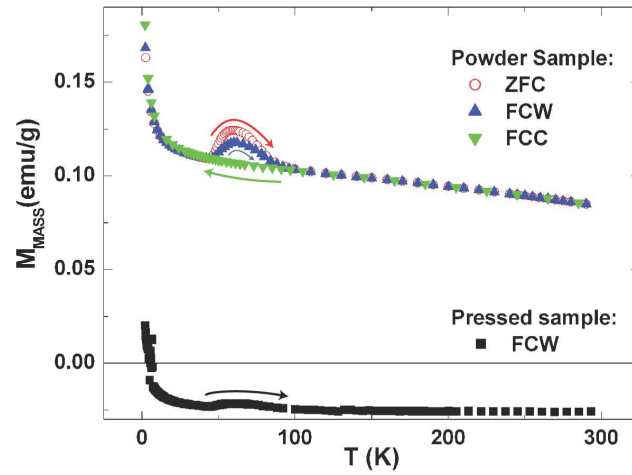


Figure 3.8: (Color on-line) $M_{\text{mass}}(T)$ curves for powder Ag-C samples (upper) and pressed Ag-C samples (lower) measured in a field of 1.0 T. Arrows indicate whether the measurement was made upon cooling or warming.

Ferromagnetic Behavior of Powder Samples

Figure 3.8 shows the $M_{\text{mass}}(T)$ behavior for both the powder and pressed samples. The three upper $M_{\text{mass}}(T)$ curves correspond to a powder sample measured in the ZFC, FCC, and FCW modes already described. The only difference in $M_{\text{mass}}(T)$ for the three measuring modes is in the peak that appears between 50 and 90 K. Also the $M_{\text{mass}}(T)$ curves for the powder sample are positive and of greater magnitude than the $M_{\text{mass}}(T)$ curve of the pressed sample, which is negative and corresponds to diamagnetic behavior.

In order to determine whether the positive $M_{\text{mass}}(T)$ of the powder sample corresponds to ferromagnetic (or ferrimagnetic) behavior, M_{mass} vs. H curves were measured at various temperatures. Figure 3.9 shows a selection of measured $M_{\text{mass}}(H)$ curves for a sample measured at 2, 10, 50, 100, and 200 K. The upper left inset of Fig. 3.9 is a close-up of the $M_{\text{mass}}(H)$ curve at 10 K clearly showing a ferromagnetic hysteresis. The lower right inset is the corresponding $M_{\text{mass}}(T)$ ZFC curve for the measured sample. Some differences in the M_{mass} values between the main panel $M_{\text{mass}}(H)$ data and the inset $M_{\text{mass}}(T)$ data for a given (H, T) are discussed in the context of a spin reorientation.

The H_c determined from $M_{\text{mass}}(H)$ curves is also plotted vs. T in Fig. 3.10; the $M_{\text{mass}}(H)$ curves indicate a weak ferromagnetic behavior all the way up to 300 K with an $H_c=389$ Oe at 2 K and an $H_c=103$ Oe at 300 K. Furthermore, the $H_c(T)$ data (excluding the data giving the sharp increase in H_c at low T) can be fit to the mean-field approximation

$$H_c(T) = H_c(0) \cdot \sqrt{1 - \frac{T}{T_c}},$$

where the best fit is achieved for an extrapolated $H_c(0) = 190$ Oe and a $T_c = 425$ K, from which we estimate the presence of ferromagnetic behavior up to ~ 425 K

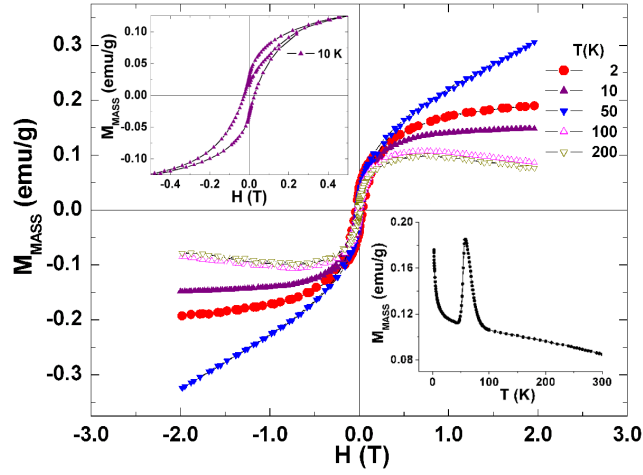


Figure 3.9: (Color on-line) Selected $M_{\text{mass}}(H)$ curves for a ZFC powder sample. Upper left inset: Close up of $M_{\text{mass}}(H)$ curve at 10 K clearly showing ferromagnetic hysteresis. Lower right inset: corresponding $M_{\text{mass}}(T)$ ZFC curve.

(Fig. 3.10). The upturn in H_c at lower temperatures is discussed in the context of a spin reorientation.

Also of interest is the saturation behavior of the $M_{\text{mass}}(H)$ curves (Fig. 3.9). The curves taken at low temperatures, *i.e.* left of the $M_{\text{mass}}(T)$ peak, continue to increase to a higher M_{mass} while the higher-temperature curves, *i.e.* right of the peak, appear to saturate at a lower H and show a downturn in M_{mass} with increasing H beyond saturation. The downturn in the $M_{\text{mass}}(H)$ curves suggests that there is a diamagnetic component present in the sample that begins to dominate at higher H once the ferromagnetic component has saturated.

Diamagnetic Behavior of Pressed Samples

The lower curve in Fig. 3.8 shows the $M_{\text{mass}}(T)$ behavior for a sample pressed with ~ 1 ton of pressure. The pressed sample is no longer ferromagnetic, but instead shows diamagnetic behavior above 5 K with a sharp tail at low T that gives a positive M_{mass} below 5 K. In addition, because diamagnetism and ferromagnetism can

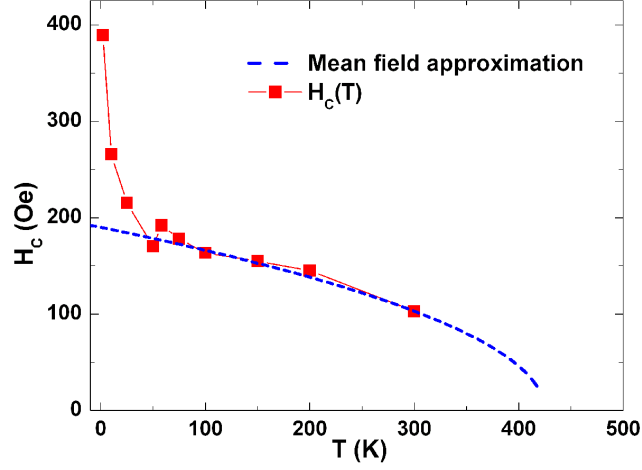


Figure 3.10: (Color on-line) H_c calculated from $M_{\text{mass}}(H)$ curves plotted vs. T showing ferromagnetic behavior up to 300 K. Mean field approximation giving a $T_c \approx 425$ K.

coexist [28], Fig. 3.11 shows $M_{\text{mass}}(H)$ curves that clearly demonstrate the absence of ferromagnetic hysteresis in the pressed samples and thus the complete transition to diamagnetic behavior with isolated paramagnetic spins in the pressed samples. Furthermore, the diamagnetic behavior strongly suggests that the ferromagnetic behavior of the powder samples is intrinsic to the Ag-C sample and cannot be explained by magnetic impurities since the pressed sample and the powder sample consist of the same materials.

The diamagnetic $M_{\text{mass}}(T > 100\text{K})$ in Fig. 3.8 corresponds to a mass susceptibility of $\sim -2.6 \times 10^{-6}$ emu/g, which is within the range of the diamagnetic susceptibility of nearly all known carbon allotropes, which exhibit diamagnetic susceptibility in the range of $\chi = -(10^{-5} - 10^{-7})$ emu/g [87]. Linear fits to the $M_{\text{mass}}(H)$ curves of Fig. 3.11 also give a mass susceptibility approaching $\sim -2.6 \times 10^{-6}$ emu/g. Therefore, pressing the sample recovers the diamagnetic behavior expected for bulk carbon as well as reducing the peak in the $M_{\text{mass}}(T)$. We attribute the low- T tail (below 5 K) to retention of isolated paramagnetic spins in the carbon mass.

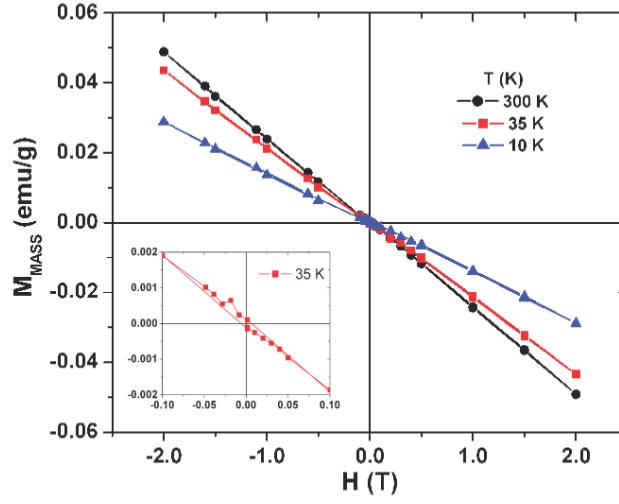


Figure 3.11: (Color on-line) Selected $M_{\text{mass}}(H)$ curves for a pressed sample at 10 K, 35 K and 300 K, clearly showing the absence of ferromagnetic hysteresis and complete transition to diamagnetic behavior in the pressed samples. Inset: Magnified view of $M_{\text{mass}}(H)$ curve at 35 K showing the diamagnetic behavior at low fields.

Corrected Mass Magnetization for Powder Samples

As previously discussed, from Fig. 3.9 we deduce the presence of both a diamagnetic and weak ferromagnetic component in the powder samples. If we assume that the diamagnetic component in the powder samples responsible for the downturn in the $M_{\text{mass}}(H)$ curves has the same magnitude as the diamagnetic component in the pressed samples, we can use the diamagnetic susceptibility of the pressed samples,

$$\chi_{\text{dia}} = -2.6 \times 10^{-6} \text{ emu/g},$$

to correct the $M_{\text{mass}}(H)$ curves of the powder samples of Fig. 3.9. Accordingly, we define a corrected magnetization,

$$M_{\text{corr}}(H) = M_{\text{mass}}(H) - \chi_{\text{dia}} \cdot H,$$

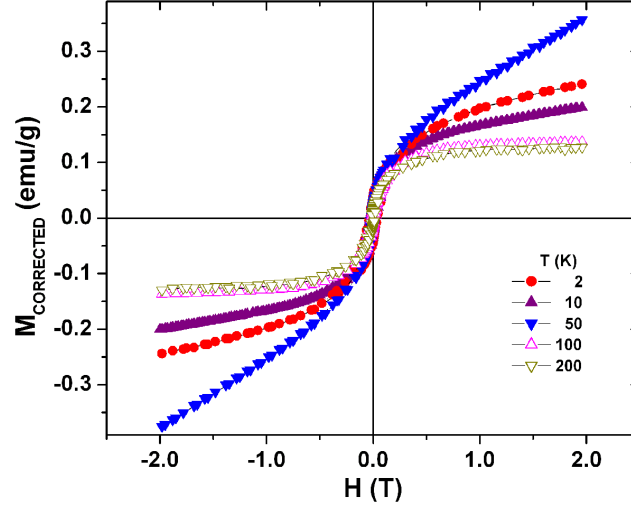


Figure 3.12: (Color on-line) Corrected mass magnetization, $M_{\text{corr}}(T)$, for powder Ag-C samples showing a near saturation of the magnetization for $T \geq 100$ K.

for the ferromagnetic component of the powder samples. Figure 3.12 shows $M_{\text{corr}}(H)$. The correction eliminates the downturn in the magnetization observed in Fig. 3.9, thus supporting that the diamagnetic component in the pressed sample is about the same as that in the powder sample. Furthermore, we now see that for $T \geq 100$ K the M_{corr} nearly saturates in an applied $H = 2$ T with an $M_s \rightarrow 0.14$ emu/g. For lower T , the M_{corr} does not saturate in an applied $H = 2$ T, especially for temperatures corresponding to the $M_{\text{mass}}(T)$ peak where it reaches 0.35 emu/g at 2 T.

Peak in the Mass Magnetization and Spin Reorientation

Our data are consistent with a first-order spin reorientation with a critical temperature (T_m) that varies only a little between nanospheres, but exhibits a thermal hysteresis. The critical temperature upon warming is $50 \text{ K} < T_{m\uparrow} < 90 \text{ K}$; upon cooling, the critical temperature occurs at a lower temperature. In order to test this deduction, we measured the ZFC curves for samples cooled to different temperatures to see at what lower temperature the peak in $M_{\text{mass}}(T)$ appears. The

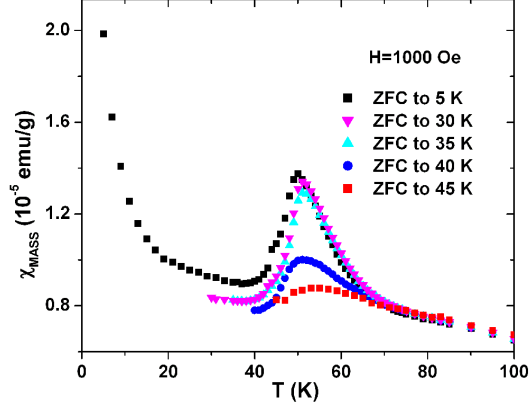


Figure 3.13: (Color on-line) Mass susceptibility $\chi_{\text{mass}}(T)$ for powder Ag-C samples ZFC to different temperatures, showing a thermal hysteresis that results in the peak being suppressed for samples that are not sufficiently cooled.

result, shown in Fig. 3.13, clearly identifies the interval $30 \text{ K} < T_{m\downarrow} < 40 \text{ K}$ for the critical temperature on cooling in zero field. In addition, there appears to be a time dependence of the spin reorientation that makes the transition sluggish upon cooling in an applied magnetic field. If an applied magnetic field inhibits the spin reorientation, it would slow it down to broaden the peak in the FCC measurement to where it is not visible. This situation would occur if the higher temperature spin orientation were favored by an applied magnetic field.

3.2.4 Trace Metal Analysis

The presence of the observed magnetic behavior in a sample containing only Ag and C is highly unusual since Ag and bulk carbon are diamagnetic. For this reason, the sample was examined for traces of magnetic contaminants with a micromass platform quadrupole inductively-coupled plasma mass spectrometer (ICP-MS) with a hexapole collision/reaction cell and a single Daly-type detector.

Mass spectrometry measurements were done on milligram samples of the Ag-

Table 3.1: Summary of ICP-MS elemental analysis (Below detection limit = BDL).

Element	Method Blank (ppb)	Sample 1 (ppb)	Sample 2 (ppb)
^{52}Cr	21.7	BDL	373
^{60}Ni	1449	BDL	161
^{63}Cu	22.4	88.1	113
^{65}Cu	22.7	85.3	BDL
^{109}Ag	BDL	683135	316706
^{114}Cd	BDL	64.0	BDL
^{120}Sn	BDL	3.46	BDL
Other	—	BDL	BDL

C sample extracted with concentrated HNO_3 and sonicated with ultrasound for at least 20 minutes. The solutions were then diluted to appropriate levels for comparison to calibrated standard solutions. Two solutions were analyzed in detail, along with a method blank consisting of the concentrated HNO_3 sonicated without the sample and diluted and prepared for analysis in the same way as the two sample solutions. Samples were scanned for all possible elements and quantitatively analyzed for the following elements: Li, B, Na, Mg, Al, Si, P, K, Ca, V, Cr, Mn, Fe, Co, Ni, Cu, Zn, As, Se, Rb, Sr, Mo, Ag, Cd, Sn, Sb, Cs, Ba, La, Ce, Pb, Bi, Th, and U.

Table 3.1 shows the summary of the quantitative ICP-MS analysis. Both sample solutions gave strong peaks for Ag in the ppm range, indicating that the Ag was dissolved out of the Ag-C sample and suggesting that other metals present in the sample should also have been dissolved into the solution. The two sample solutions showed only some metal contaminants in the ppb range with all other elements falling below the detection limit (BDL). Of the elements detected in the ppb range, only one of them, Cu^{65} , was detected in both sample 1 and 2. Cu was less than 100 ppb above the method blank and is usually not magnetic. Cr was detected in one sample solution (350 ppb above the method blank) and was BDL in

the other sample solution. The other elements listed in Table 3.1 were only detected in one sample and were all present in greater amounts in the method blank. Thus the only possible magnetic contaminant detected, Cr, was only found in one of the sample solutions and was only 0.1% of the amount of Ag detected in the solution; therefore it cannot explain the observed magnetic behavior. These results support that the magnetism being reported is indeed coming from the Ag-C sample and not from magnetic contaminants present in the sample.

3.3 Discussion

A model accounting for the observed magnetic behavior must not only be able to explain how spins are localized in the Ag-C sample, but also what type of magnetic interaction exists between the localized spins in order to give a net magnetic moment and the observed ferromagnetic behavior. Localization of spins in Ag is unlikely since Ag has a full $4d^{10}$ shell and one $5s^1$ electron that is delocalized in a broad, half-filled band that gives metallic conduction. Therefore, the localized spins and the ferromagnetic behavior must be coming from the carbon surrounding the Ag nanoparticles. In order to understand how the spins are being localized in the carbon, we must first have an understanding of the structure of the carbon coating the Ag nanoparticles.

As seen in Figs. 3.1-3.4, the carbon forms necklace-like structures comprised of interconnected spheres. The spheres are nested, closed carbon cages of a graphene nature that encapsulate the Ag nanoparticles. For example, Fig. 3.2 shows a carbon nanosphere consisting of 4 nested, closed carbon cages.

What is most important about the structure for a model of the ferromagnetism is the curvature of the nanospheres. In graphite, $sp^2 + p_\pi$ bonding gives metallic behavior from itinerant p_π electrons both in the ab -plane and in narrow c -axis dispersion bands. Introducing a curvature to graphene planes changes the

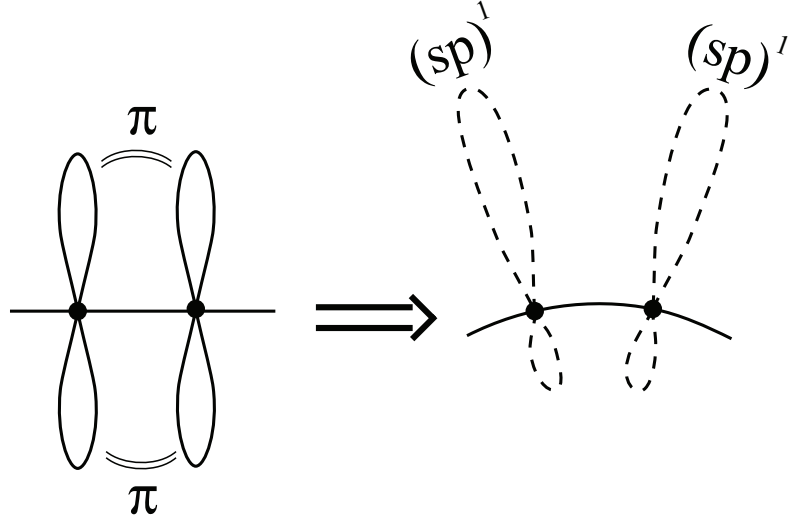


Figure 3.14: Schematic representation showing the transition from p_π delocalized spins in a planar graphene sheet toward $(sp)^1$ localized spins in a curved graphene sheet.

$sp^2 + p_\pi$ bonding towards sp^3 hybridization as found in Si, but with a half-filled $(sp)^1$ orbital extending out from the curved graphene sheet (see Fig. 3.14). For a large curvature of the graphene sheets, the s character of the (sp) hybrid orbital is large so that extension of the orbital is small on the interior of the graphene layers, *i.e.* towards the center of the nanosphere. Consequently, for a large curvature these half-filled orbitals have only a small overlap with like orbitals on their carbon near neighbors in the plane and, as discussed below, between half of the carbon across planes. Thus the curvature reduces the intraplane overlap of the half-filled orbitals perpendicular to the surface of the carbon sheets from that of the p_π orbitals of flat sheets until, at a critical curvature, the electrons in these orbitals become localized with a spin $S = 1/2$ in the absence of strong interplane interactions.

Across planes, the situation is more complex as there exist two distinct carbon sites in graphite. Due to the ABAB c-axis stacking of carbon planes in graphite, there are carbon α -sites with carbon neighbors directly below and above and carbon

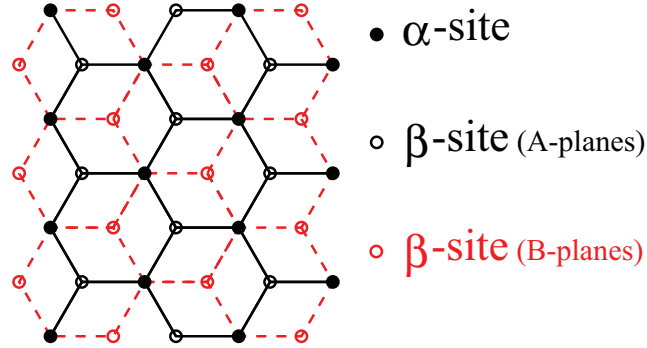


Figure 3.15: (Color on-line) Schematic illustration showing the α and β -sites in graphite.

β -sites without carbon neighbors directly below and above (Fig. 3.15). Thus half of the carbon atoms are in α -sites that form chains of C atoms along the c -axis while the other half are in β -sites with no carbon neighbors directly above or below.

Whereas the curvature reduces the in-plane π -bonding to where the spins on the β sites are localized, the interplane bonding between α -site C atoms remains strong enough to give a 1D itinerant-electron band. If the 1D band remains half-filled, we should expect an antiferromagnetic coupling between the β -site spins through the α -site 1D band. However, a smaller work function for silver than for graphite, $\Phi_{\text{Ag}} < \Phi_{\text{C}}$, means that electrons are donated from the Ag nanoparticles to the C nanospheres. Since the correlation splitting U of the $(sp)^1$ and $(sp)^2$ states at the β sites is larger than the splitting of the two-electron and three-electron bonds of the α sites, the Ag can be expected to donate electrons to the 1D α -site bands to make them *ca.* 3/4-filled with a spin of $0.5 \mu_{\text{B}}/\text{C}_{\alpha}$. As shown schematically in Fig. 3.16, the dominant virtual charge transfer is from an α -chain to a β site, and the Pauli exclusion principle only allows transfer of electrons with a spin opposite to the spin on a β site. Therefore, we anticipate an antiferromagnetic coupling between the α -site and β -site spins to give a net ferrimagnetic moment of *ca.* $0.25 \mu_{\text{B}}/\text{C}$ for the powder samples.

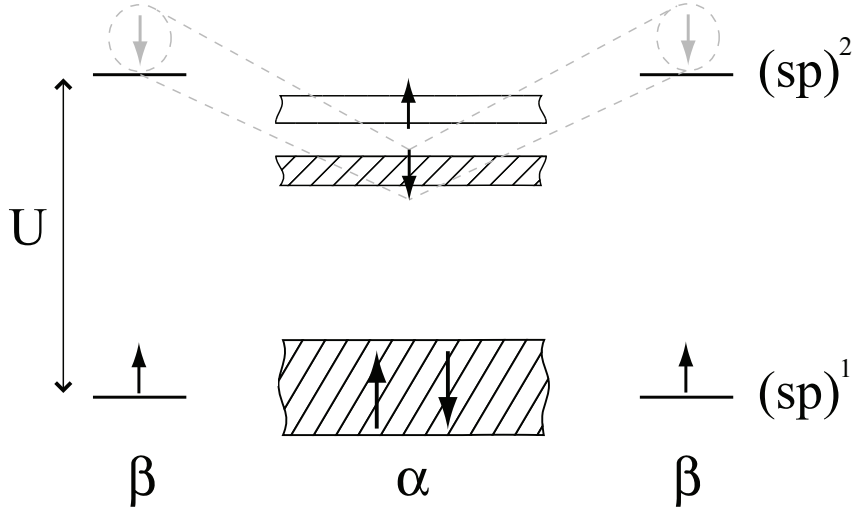


Figure 3.16: Schematic illustration of the ferromagnetic superexchange interaction between β -sites through a strongly-correlated 3/4-filled α band. Here $(sp)^1$ indicates a half-filled (sp) orbital and $(sp)^2$ indicates a filled (sp) orbital, and U is the correlation splitting of the $(sp)^1$ and $(sp)^2$ states.

This model is supported by the TEM image in Fig. 3.2 where we see that the interplanar spacing of the carbon sheets surrounding the Ag nanoparticles is ~ 3.7 Å, which is greater than the 3.35 Å spacing of graphite. The larger C-C distance between the α -site C atoms is consistent with the introduction of antibonding electrons that, in essence, transforms two-electron bonding orbitals to three-electron bonds with localized antibonding-electron spins. From the virial theorem, as has been argued elsewhere [34], the transition from spin-paired to strongly correlated antibonding electrons would increase the separation of the α -site C along a 1D chain, as we observe in our TEM images of the powder samples.

Flattening of the graphitic sheets would restore graphite p_π bonding to eliminate localized electrons even at the β sites; however, our structural characterization indicates that this is not the case for the 1-ton-pressed samples since the curvature is maintained (see Fig. 3.7) in the graphene sheets surrounding the Ag nanoparticles. Instead this pressure appears to increase the C-C bonding between nanospheres

and, more importantly, shorten the C–C interplanar spacing, thus broadening the 1D α -site bands and pairing antiparallel the β -site spins. This change would revert the system to the diamagnetic behavior expected for bulk Ag and C samples, which we indeed observe in Fig 3.8 and Fig 3.11 for the pressed samples.

The peak in the $M_{\text{mass}}(T)$ data can be explained by a spin reorientation. The only difference in the FCW and ZFC $M_{\text{mass}}(T)$ curves of Fig. 3.8 for the powder sample is in the magnitude of a peak found in the interval $50 \text{ K} < T < 90 \text{ K}$. The peak is only observed for measurements made in the warming direction (ZFC and FCW); it is completely suppressed for measurements made in the cooling direction (FCC). Also the magnitude of the ZFC peak is always slightly greater than the FCW peak.

A similar peak in carbon nanohorns has been reported by Bandow *et al.* [6] and was attributed to adsorbed oxygen. Although there are similarities between the $M_{\text{mass}}(T)$ peak of the carbon nanosphere powder samples and the peak in the carbon nanohorn samples, the peak we observe cannot be explained by the presence of oxygen because of the thermal hysteresis and suppression of the peak when measuring in the cooling direction. There are magnetic transitions associated with solid oxygen within the peak temperature interval [22, 70], but they are second-order and thus are always observed at the same temperature whether measurements are made upon warming or cooling (no thermal hysteresis). Therefore, the presence of oxygen cannot explain the observed peak in the carbon nanosphere sample; instead, we propose an explanation for the observed peak based on a first-order spin reorientation.

Both the $M_{\text{mass}}(T)$ and $M_{\text{corr}}(H)$ behavior suggest that the sample exhibits a spin reorientation at the temperature corresponding to the peak. A spin reorientation occurs when there is a change in the site easy-magnetization axis. Where the spins reorient their direction, the spin system becomes more plastic, which allows

for a larger M in an applied H . In a second-order transition, the site anisotropy energy goes smoothly through zero; but in a first-order transition, the anisotropy energy goes to a minimum, but remains finite. A displacive structural change would accompany a first-order transition.

A spin reorientation is thus able to explain the complete suppression of the peak upon cooling in a magnetic field (FCC curve in Fig. 3.8), as well as the smaller thermal hysteresis upon cooling in zero field shown in the ZFC curves of Fig. 3.13. In addition, the $M_{\text{corr}}(H)$ curves measured at temperatures corresponding to the $M_{\text{mass}}(T)$ peak, where the spin system is more plastic, showed a greatly increased saturation M_{corr} that is consistent with a spin reorientation (see Fig 3.12). For example, at 50 K, $M_{\text{corr}}(H)$ is still increasing strongly at an H of 2 T with a $M_{\text{corr}} \approx 0.35$ emu/g.

A spin reorientation is also supported by the increase in H_c for temperatures below the $M_{\text{mass}}(T)$ peak (see Fig. 3.10). We expect different spin orientations to lead to a difference in the nature of the domain structure and thus in the $M_{\text{corr}}(H)$ behavior and the H_c . Apparently, the lower temperature orientation has a higher saturation magnetization at a higher field (Fig 3.12) as well as a larger H_c that increases more rapidly with decreasing temperature, giving an upturn in the low-temperature H_c (Fig. 3.10).

Furthermore, we attribute the difference in the magnetization data between the main panel and lower right inset of Fig. 3.9 to the time dependence of the spin reorientation. Because multiple measurements are made at the same temperature when measuring a hysteresis curve, the magnetization measurements made at 50 K for the $M_{\text{mass}}(H)$ hysteresis curve in the main panel were taken over a much longer time than the single measurement made at 50 K for the $M_{\text{mass}}(T)$ curve in the lower right inset. Therefore, since the sample is held close to the spin reorientation temperature (50 K) for a longer period of time in the main panel, the spin system

has become more plastic. This results in $M_{\text{mass}}(T = 50K, H = 1T) > M_{\text{mass}}(T = 2K, H = 1T)$ in the main panel and explains the discrepancy with the magnetization data in the lower right panel, where $M_{\text{mass}}(2K) > M_{\text{mass}}(50K)$.

Figure 3.17 shows the suspected spin orientations for spin reorientations occurring within the carbon nanosphere. Orientation A corresponds to spins oriented parallel to the (*sp*) orbital axis, *i.e.* perpendicular to the carbon nanosphere surface, and orientation B corresponds to spins oriented perpendicular to the orbital axis, *i.e.* tangential to the carbon nanosphere surface. As deduced above for a 3/4-filled α band, a net moment of $0.25 \mu_B/\text{C}$ atom is expected. However, from Fig. 3.17 we see that the spin orientations and the spherical geometry of the carbon nanospheres results in no net magnetic moment in the absence of an external magnetic field. However, once domain walls have been introduced by the application of a magnetic field, a remnant magnetization and a coercivity can be expected.

Fig. 3.18 shows how both spin orientations result in a net ferromagnetic moment in an external magnetic field. For orientation A, more spins align parallel to the external field by forming a Bloch wall, which is shown in Fig. 3.18 as an idealized Bloch wall across the equator of the nanosphere. The net ferromagnetic moment increases from the equator to the poles due to an increasing component of the preferred spin orientation lying in the direction of the external field. In addition, spin canting away from the preferred spin orientation, *i.e.* parallel to the (*sp*) orbital axis, may also contribute further to the net moment. Spin orientation B achieves a net moment by canting its spins away from the spherical surface in the direction of the external field. For this case, the net ferromagnetic moment increases from the equator to the poles because of an increasing torque exerted by the external field on the spins. Both orientations do not allow complete alignment of the β spins in an applied H , so that the net moment for each spin orientation is less than the $0.25 \mu_B/\text{C}$ atom previously calculated.

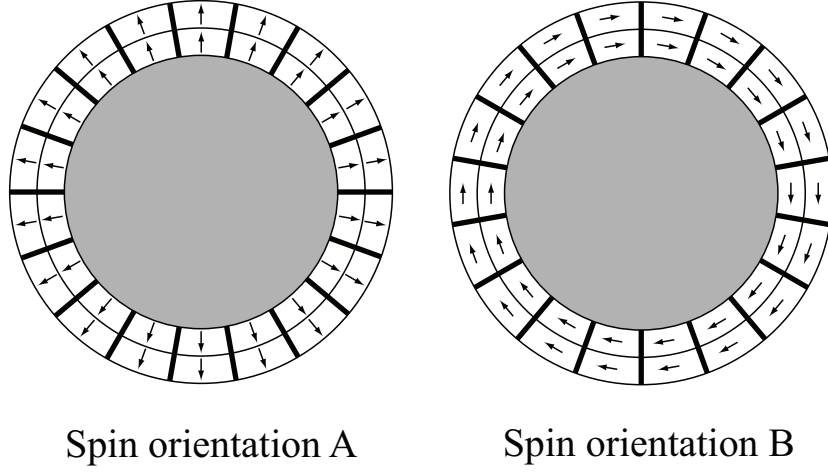


Figure 3.17: Schematic illustration showing two possible spin orientations of localized $(sp)^1$ β spins separated by itinerant α sites. Orientation A corresponds to spins oriented along the (sp) orbital axis, while orientation B corresponds to spins tangential to the spherical surface.

If the local net moment is $\mu = 0.25 \mu_B/\text{C atom}$, then for spin orientation A it can be shown that the net moment for a carbon nanosphere is approximately

$$\begin{aligned}
 \mu_A &= \int_S \mu \cos(\phi) dS \\
 &= \frac{2r^2 \int_0^{\pi/2} \mu \cos(\phi) \sin(\phi) d\phi \int_0^{2\pi} d\theta}{4\pi r^2} \\
 &= 0.5 \mu \\
 &= 0.125 \mu_B/\text{C atom}.
 \end{aligned}$$

or 50% of the $\mu = 0.25 \mu_B/\text{C}$, not including any canting of the spins away from the (sp) orbital axis, which would further increase the net moment. On the other hand, it is not possible to calculate the net moment for spin orientation B without knowing the degree of spin-canting out of the plane. Although it is difficult to determine from these considerations which spin orientation occurs at low and high temperature,

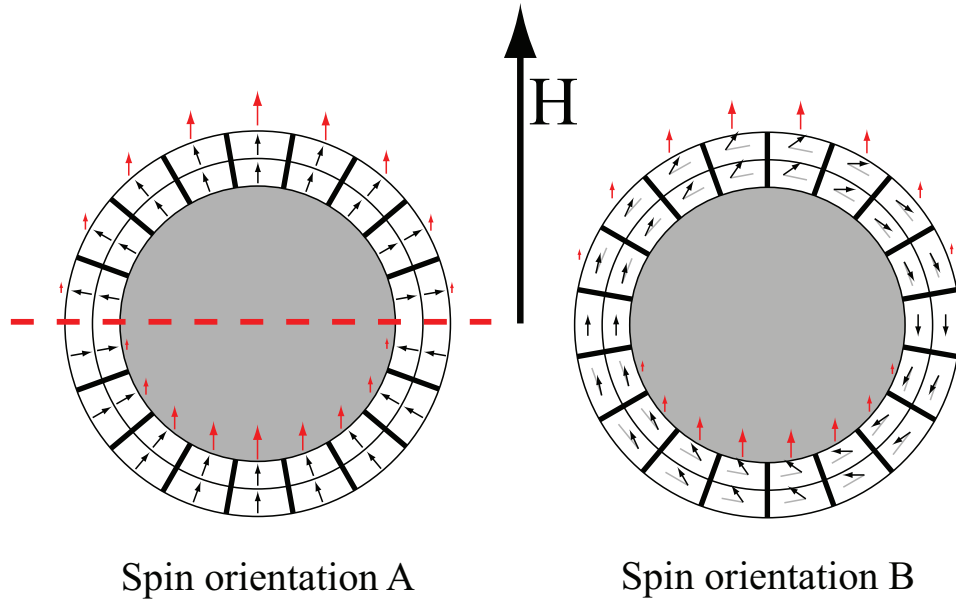


Figure 3.18: (Color on-line) Schematic illustration showing spin orientation A and B in an applied external field H . Orientation A achieves a net ferromagnetic moment by the formation of a Bloch wall (dashed red line) in addition to spin-canting (not shown). Orientation B achieves a net ferromagnetic moment by spin-canting. The small red arrows shown on the outer and inner surface of the carbon shells are schematic representations of the net ferromagnetic moment and show an increasing ferromagnetic moment for both orientations as one approaches the poles.

nevertheless, our experimental data support a spin reorientation that causes a peak in the $M_{\text{mass}}(T)$ curves upon warming, but not upon cooling, an upturn in the H_c at low temperatures that corresponds to a more difficult spin reversal of the low-temperature spin orientation, and a difference in saturation magnetizations at temperatures below and above the spin reorientation temperature.

The ferromagnetic areas appear to be separated by domain walls as in any ferromagnet. The motion of these walls in an applied field H allows the tracing out of an M – H hysteresis loop. However, bending of the spins into the direction of the applied H field would be resisted by the magnetocrystalline anisotropy, which is expected to be different for each spin orientation. Therefore, although it is not possible to determine which of the suspected spin orientations is favored at the lower or higher temperatures, it is apparent that the low-temperature orientation results in a higher H_c that increases more rapidly with decreasing temperature. Also, the low temperature orientation does not allow for full ferromagnetic alignment of the spins in an $H = 2$ T, suggesting a stronger magnetocrystalline anisotropy. Rotation of the spins from parallel to perpendicular to the orbital axes would occur at a temperature where the net site anisotropy becomes small and the spins are more easily aligned in the direction of the applied field; but the interatomic exchange field does not change sign. Such a spin reorientation would result in a peak in the $M_{\text{mass}}(T)$, which is indeed observed.

On the outer surface of the carbon nanosphere the $(sp)^1$ orbital will be a reactive surface state so long as there is no interaction with a neighboring nanosphere or an adsorbed species. In the graphene layers below the surface, the localized $(sp)^1$ electrons appear to be sterically protected from adsorbed species, thus giving the observed ferrimagnetic behavior in the powder samples even if the surface states are all spin-paired with a surface species or a neighboring nanosphere. With three concentric carbon nanospheres and $\mu = 0.125\mu_B/\text{C}$ atom about each Ag particle

(assuming orientation A), we can estimate a magnetization $M_{\text{corr}} \approx 0.6$ emu/g, which is sufficient to account for the observed magnetization M_{corr} .

The reactive states on a carbon nanosphere surface provide the C–C bonding between nanospheres needed to form the robust necklace-like structures observed in the powder samples. The other reactive surface sites may be satisfied by chemisorbed species, *e.g.* the oxygen detected in small quantities with EDS and/or hydrogen from adsorbed H₂O. Satisfaction of the active surface sites would explain why, under pressure, the carbon nanosphere necklaces can form slabs of densely packed nanospheres that are fragile enough that they can relatively easily be mechanically broken back down into the original carbon nanosphere necklace-like structures of the Ag-C powder. That is, if the electrons on the surface of the C nanospheres remained as reactive sites, then one would expect a chemical bond between pressed C nanospheres and much more robust pressed samples. However, since this is not the case, it appears that the C–C bonding between nanospheres needed to form the necklace-like structures occurred during the synthesis process and the remaining exposed surface sites became satisfied by chemisorbed species, such as the oxygen and water present in the air to which the samples were exposed immediately after synthesis and during their handling.

This model accounts qualitatively for the presence of a diamagnetic and a weak ferrimagnetic contribution to the magnetic susceptibility as is signaled by the magnetic measurements in Fig. 3.9. It also predicts a magnetic-ordering temperature and weak ferrimagnetism that is dependent on electron transfer from the Ag particles to the α -site C chains. Although the model allows for a reorientation of the spin axis relative to the (*sp*) orbital axis, our data do not provide an unambiguous identification of which spin orientation is favored at the lowest temperatures. Nevertheless, we would expect spin orientation B to be favored at lower temperatures since this orientation is stabilized by magnetostatics.

While we have principally considered intraparticle interactions, *e.g.* spin orientation relative to the (sp) orbital axis, it may be that the interparticle interactions, *i.e.* between nanospheres, are responsible for the spin reorientation. Then the peak in the $M(T)$ may be associated with an interparticle spin reorientation between carbon nanospheres or with a transition from a superparamagnetic to a blocked state.

3.4 Conclusions

Carbon can be present in many different forms, each exhibiting drastically different properties. Carbon nanostructures, such as fullerenes, onions, and CNTs have generated much scientific research and are already being used in numerous applications. More recently, novel carbon nanostructures, such as carbon nanofoam, have sparked a new interest in carbon materials that possess ferromagnetic properties. The carbon nanostructures presented here appear to be one such material.

We conclude that by increasing the curvature of a graphite sheet to beyond a critical value, it is possible to generate reactive, half-filled (sp)¹ orbitals projecting from the outer surface and localized (sp)¹ spins below the surface. The reactive, localized spins on the surface may be spin-paired by adsorbed species or by C–C bonding with neighboring nanospheres. The localized (sp)¹ spins below the surface occur at β sites and interact within a graphene sheet through a strongly correlated itinerant-electron band at α sites that form carbon chains along the c -axis.

A difference in work functions between Ag and C results in the Ag nanoparticle donating electrons to the carbon nanosphere α band so that it becomes more than half-filled. The magnetic interaction between the localized spins at the β sites is through a more than half-filled α band that gives a ferromagnetic alignment of the β spins through a spin-polarized α band with an antiferromagnetically aligned net moment that is less than the moment on the β sites. Therefore the interaction

between the α and β sites is ferrimagnetic with a magnetic ordering above room temperature.

Pressure shortens the C-C bonds of the α -site chains, which suppresses the spin-polarization of the α -site antibonding electrons and strengthens the interactions between the half-filled orbitals of the β sites. As a result, the diamagnetism of the carbon dominates the susceptibility of the pressed samples.

We believe this finding opens the door to tailoring the curvature of carbon nanospheres encapsulating a metallic nanoparticle core for a variety of applications. For example, carbon is a biologically friendly material and Ag, even when sterically stabilized, has been shown to have antimicrobial properties and even shows the potential to inhibit HIV [25]. In this light, a ferromagnetic carbon coating could prove very useful in drug delivery, or even guided drug delivery where a magnetic field, *e.g.* from an MRI, is used to guide the encapsulated material to a specific location in the human body. Furthermore, there seems to be no reason why the synthesis could not be extended to include other metals within the ferromagnetic carbon nanospheres, thus opening many new possibilities.

More fundamentally, this work proposes a model for magnetic order in graphitic carbon materials. While there are various models for the localization of spins in carbon materials, there are very few models for the magnetic interaction between such localized spins capable of explaining the recently observed “ferromagnetic” behavior in a variety of carbon materials.

3.5 Observation

A significant number and variety of carbon materials with ferromagnetic properties have now been reported. Unlike the negative curvature carbon nanofoams, our material contains Ag nanoparticles that play the role of electron donors to α -site bands that are spin-polarized and give a net ferrimagnetic moment from α and β

sites. We note here that, unlike other models in the literature, we have used a model that is not dependent on negative curvature regions in the carbon. Although one might expect such regions to exist at the necks of neighboring carbon nanospheres in necklace-like structures, from Fig. 3.4 (left panel) we can find no evidence of such negative curvature regions in our material; instead we clearly observe spherical carbon shells joined by C-C bonding.

Part II

Layered Oxides

Chapter 4

Na_xCoO_2 and superconductive $\text{Na}_{0.33}\text{CoO}_2 \cdot 1.3\text{H}_2\text{O}$

4.1 General Overview

Original investigations of Na_xCoO_2 focused on its potential as a cathode material in a Na-ion battery and were motivated by the excellent performance of the Li_xCoO_2 system as a cathode material for a Li-ion rechargeable battery. Although its performance as a cathode in a Na battery proved inferior to those of the Li_xCoO_2 cathode in the analogous Li-ion battery, the discovery of a high thermoelectric power together with a high electronic conductivity and low thermal conductivity in Na_xCoO_2 sparked a new interest in its potential as a thermoelectric material [103]. Subsequent investigations have shown that the sodium-rich Na_xCoO_2 composition with $x \approx 0.7$ is the most promising for a thermoelectric material. Although a clear understanding of the system is still under investigation, its large thermopower ($100 \mu\text{V}/\text{K}$ at 300 K) has been attributed to the spin entropy carried by strongly correlated electrons hopping on a triangular lattice [29].

The more recent discovery of superconductivity in the hydrated sodium-

poor cobaltate $\text{Na}_{0.33}\text{CoO}_2 \cdot 1.3\text{H}_2\text{O}$ [99, 91] has generated considerable research activity into understanding the origin of the superconductivity in this system. Although the low- T_c (≈ 4.5 K) and chemical instability of the hydrated superconductive $\text{Na}_{0.33}\text{CoO}_2 \cdot 1.3\text{H}_2\text{O}$ phase make it commercially unattractive, it is still of great interest due to both its similarities and differences to the copper-oxide high-temperature superconductors (HTSC). Like the copper-oxide HTSC, the superconductivity appears to be strongly 2D in character and also gives a dome-shaped dependence of T_c vs. electronic doping [91]. On the other hand, the structure is quite different, with the Cu-oxides having in-plane Cu-O-Cu interactions while the Co-oxides have hexagonal symmetry and direct Co-Co interactions.

Perhaps the most conspicuous difference is the role of water in the superconducting phase; indeed $\text{Na}_{0.33}\text{CoO}_2 \cdot 1.3\text{H}_2\text{O}$ is one of the few, if not the only, example of a hydrated superconductor. In fact, it is quite sensitive to the degree of hydration as well as the $\text{Co(IV)}/\text{Co}$ ratio. Obviously, clear determination is needed as to the role of the intercalated water in the superconducting cobalt oxides, *i.e.* whether it plays a passive role as a spacer in the structure, expanding the c -axis and separating the CoO_2 planes, making them more two-dimensional as in the Cu-oxide HTSCs, or whether it plays an active role, healing oxygen vacancies and/or contributing positive counter cations to the system in the form of H_3O^+ .

In addition to ongoing investigation of both the Na-rich Na_xCoO_2 with promising thermoelectric properties and the hydrated Na-poor $\text{Na}_{0.33}\text{CoO}_2 \cdot 1.3\text{H}_2\text{O}$, subsequent research efforts into understanding the physical properties for the entire phase diagram have yielded other compositions of interest. In particular the Na_xCoO_2 composition with $x \approx 0.5$ undergoes what has been referred to as a “metal-insulator” transition (MIT) in the literature [40]. While the 2-layer phase with Na-ions in prismatic coordination (P2) is metallic throughout the range of Na compositions ($0.25 < x < 0.8$), at $x \approx 0.5$ the resistivity is flat to semiconductor-

like with an abrupt upturn at a $T_{MIT} \approx 53$ K. Although the origin of the electronic transition is still not clear, investigations have shown that Na ordering for the $x \approx 0.5$ composition results in a transition from hexagonal ($P6_3/mmc$) to orthorhombic ($Pnmm$) symmetry at room temperature and a possibly charge-ordered state at lower temperature that may play a role in the transition to an insulating state [29]. Furthermore, a transition to an antiferromagnetically ordered state at 87 K precedes the transition to an insulating state at 53 K and is also of interest in understanding the system [30].

4.2 The role of structure, Na content, and Co valence

A clear knowledge of the possible structures of the Na_xCoO_2 system is essential to ultimately understanding their properties. All of the possible Na_xCoO_2 structures (as well as the Li_xCoO_2 structures) are layered with alternating CoO_2 layers and counter-cation planes. The Co ions are in octahedral coordination, and the CoO_2 layers are composed of edge-sharing octahedra. Alternatively, the CoO_2 layer can also be described as close-packed planes of Co atoms, with close-packed planes of O atoms above and below the Co plane.

The counter-cations Na or Li (K, Ca and Sr are also possible) are located between the CoO_2 layers in either trigonal prismatic or octahedral sites. The Na (or Li) coordination as well as the stacking sequence of the planes of oxygen atoms gives a convenient way of designating the structure for both the Na_xCoO_2 and Li_xCoO_2 layered cobalt oxide systems. For example, the Li_xCoO_2 structure used as a cathode material has Li-ions in octahedral coordination with an oxygen stacking sequence of ABCABC; it is therefore designated as the O3 structure. The O3 structure is simply a face-centered cubic array of oxygen as in the rocksalt structure with the Co and counter-cations fully ordered on alternate (111) planes of octahedral sites.

Many structures are possible if one employs both hard chemistry (solid state

Table 4.1: Summary of Na_xCoO_2 structures that can be synthesized by hard chemistry for different compositions [23].

Na content	Phase	Na coordination	O stacking
$x = 1$	α	O3	ABC
$x = 0.77$	α'	O'3	ABC
$0.64 \leq x \leq 0.74$	γ	P2	AABB
$0.55 \leq x \leq 0.66$	β	P'3	AABBCC
$x < 0.55$	$\text{Co}_3\text{O}_4 + \beta$	$\text{Co}_3\text{O}_4 + \text{P'3}$	AABBCC

synthesis) techniques as well as soft chemistry (oxidative deintercalation/reductive intercalation) techniques, *e.g.* O3, P3, O1, P2, O2, O'3, and P'3 (where the prime indicates a monoclinic distortion in the structure). While hard chemistry is used to synthesize the thermodynamically stable high-temperature structure for a particular Na composition, soft chemistry can be used to achieve low-temperature and metastable structures that are not possible to access by hard chemistry alone. Table 4.1 shows the stable structures that can be synthesized in the Na_xCoO_2 system by hard chemistry for different Na compositions.

While Table 4.1 gives the structures that can be made by the hard chemistry of solid state synthesis, it is also possible to maintain a structure beyond the compositional range allowed by the solid state synthesis by employing soft chemistry such as oxidative deintercalation at ambient temperature. For example, the P2 phase may be maintained down to Na compositions as low as $x \approx 0.25$ or any other intermediate Na concentration by appropriate choice of oxidizer, concentration of oxidizer, and duration of exposure to the oxidizing medium. This is of particular importance, considering that the hydrated superconductor $\text{Na}_{0.33}\text{CoO}_2 \cdot 1.3\text{H}_2\text{O}$ is derived from the metastable P2 structure with $x \approx 0.33$ that is synthesized by precisely this combination of hard and soft chemistry.

It is instructive to point out some important differences between the possible

structures. While the O3, P3, and O1 structures can be derived from each other by simple sliding of the CoO_2 sheets, the P2 structure differs from the family of O3 structures not only by sheet shifts, but also by a $\pi/3$ rotation of all (CoO_6) octahedra. Thus for a transition from an O3-type structure to the P2 structure, a greater amount of energy is needed. This inter-layer shifting explains the transitions that are observed from $\text{O3} \rightarrow \text{O}'3 \rightarrow \text{P}'3$ upon electrochemical deintercalation of Li in the Li_xCoO_2 system as well as the transition to O1 upon deep chemical deintercalation. So long as the electrochemical or chemical deintercalation is carried out at ambient T, there is not enough available energy to transition between the O3-type structures to the P2 structure. Conversely in the Na_xCoO_2 system, the P2 structure is maintained for a wide range of Na content in a metastable state so long as the temperature is not raised enough so as to provide enough energy for the $\pi/3$ rotation of the (CoO_6) octahedra to occur. Again, this point is important since the P2 structure is the one that gives the good thermoelectric material for $x \approx 0.7$, the superconductor for $x \approx 0.33$, and exhibits the insulator transition for $x \approx 0.5$.

Obviously the P2 structure is of primary importance in the Na_xCoO_2 system. For that reason, we will focus on the finer details of this structure. As in the O-type structures, the Na ions in the P2 phase also have 6-fold coordination with surrounding oxygen atoms; however, instead of an octahedral environment of oxygen ligands, the Na ions are in a trigonal prismatic coordination. This coordination has the effect of slightly opening up the structure, which makes sense for the larger Na ions. In addition, whereas in the O3 structure of the Li_xCoO_2 system the octahedral sites of the Li ions are separated by tetrahedral sites, in the P2 structure there are no tetrahedral sites but rather there are 2 distinct prismatic sites for the Na ions. The Na1 site corresponds to prismatic sites that share faces with the Co octahedra, and the Na2 site corresponds to prismatic sites that share edges with neighboring Co octahedra. Figure 4.1 shows Na ions occupying the Na2 sites of a P2 structure.

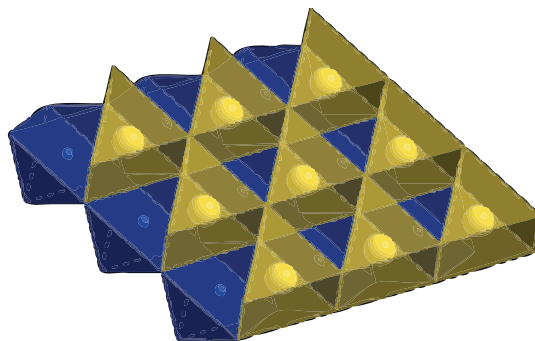


Figure 4.1: Schematic illustration of Na-ions occupying the Na2-site in the P2 structure, defined as the trigonal prismatic site that shares edges with neighboring Co octahedra.

From a simple point charge model, one would expect the Na ions to occupy the Na2 sites, which share edges with the Co octahedra, and to avoid occupying the Na1 site that share faces with the Co octahedra. Such an arrangement would appear to minimize the electrostatic repulsion between $\text{Co}^{4+/3+}$ and Na^+ and thus minimize the free energy of the system. However, the situation is more complex than this since there are also other electrostatic interactions. Experimental observations, *e.g.* neutron diffraction, indicate a mixed occupancy of both sites, with a preferential occupancy for the Na2 site except for the $x \approx 0.5$ composition, which shows equal occupancy of both sites and an ordered state [42, 109].

Experimentally the P2 structure is synthesized by a solid state reaction of Na_2CO_3 and Co_3O_4 in appropriate quantities so as to achieve the desired stoichiometry of a parent phase with a composition between $x \approx 0.64$ and 0.74 as indicated by Table 4.1. The Na content can then be tuned by oxidative deintercalation, *e.g.* with Br_2 , I_2 , HCl , or NO_2BF_4 , preserving the P2 structure down to $x \approx 0.25$. Chemical intercalation can also be used to increase the Na content up to $x \approx 1.0$ while maintaining the P2 phase [41].

The Na content in the sample strongly affects the structure. As Na is removed from the structure, the screening of negative charge between O^{2-} of the oxygen

Table 4.2: Summary of Na_xCoO_2 possible spin states.

Co valence spin state	Electronic configuration	Spin (S)	Paramag. moment μ_{eff}/μ_B
(LS) Co^{3+}	t^6e^0	0	0
(IS) Co^{3+}	t^5e^1	1	2.82
(HS) Co^{3+}	t^4e^2	2	4.9
(LS) Co^{4+}	t^5e^0	1/2	1.7

layers is decreased and the electrostatic repulsion between the CoO_2 layers increases, resulting in a c-axis expansion. Alternatively, the expansion can be explained by a decrease in the cohesive force between CoO_2 layers provided by $\text{O}^{2-}-\text{Na}^+-\text{O}^{2-}$ bonds upon the removal of Na^+ .

In addition to dramatically altering the structure, the Na content controls the Co oxidation state and thus the electronic and magnetic properties of the Na_xCoO_2 system. For example, at $x=1$ the system only contains Co^{3+} with a low spin (LS) $t^6_{2g}e^0_g$ electronic configuration that is magnetically dead (diamagnetic) and electronically insulating due to a full t_{2g} -band [41, 24]. However, for $x < 1$, Co^{4+} is introduced into the system. Table 4.2 shows all possible spin states for the localized $\text{Co}^{4+/3+}$ valence state. Unlike the Co-oxide perovskites, there are no transitions of the Co^{3+} to intermediate spin (IS) or high spin (HS) states [71, 97, 11, 90]. Introducing LS Co^{4+} with a magnetic moment of $S = 1/2$ has the effect of creating holes in the t_{2g} -band and causing a transition to metallic behavior where the holes are polaronic.

The potential of a thermoelectric material is often judged by the dimensionless figure of merit

$$ZT = \frac{\alpha^2 T}{\kappa \rho}$$

where α is the thermoelectric power (or Seebeck coefficient), κ is the thermal conductivity, and ρ is the electronic resistivity of the material. A $ZT > 1$ is considered a good thermoelectric material.

The Na_xCoO_2 composition with $x \approx 0.7$ shows a $ZT \approx 1$ thanks to a large electronic conductivity, high thermoelectric power, and low thermal conductivity. This combination is difficult to achieve since the electronic contribution to the thermal conductivity as derived from the Wiedemann-Franz law is large. In the Na_xCoO_2 system the lattice contribution to the thermal conductivity is low due to disorder in the Na plane. This disorder is at least partly attributable to the occupancy of both Na1 and Na2 sites in the Na^+ layer. While the electron contribution to the thermal conductivity is still high, the lattice contribution is low enough to provide for a high ZT because of an anomalously large α for a metal. The $x \approx 0.7$ sample approaches the transition from itinerant to localized electronic behavior, and strong-correlation fluctuations are evident in a temperature-dependent paramagnetic susceptibility.

In addition, the thermoelectric power is p-type due to holes in a t_{2g} band that is highly correlated. Strong-correlation fluctuations are associated with polaronic Co^{4+} ions that have a magnetic moment of $S = 1/2$ and thus carry a spin entropy that results in a high thermoelectric power. As the electronic conductivity increases with a decreasing amount of Na, the thermoelectric power also decreases; broadening of the narrow t_{2g} band suppresses the strong correlation fluctuations.

The Na_xCoO_2 system thus falls under the category of a phonon-glass/electron-crystal that is desired for good thermoelectric materials. It can be seen as a system comprised of “nano-blocks” consisting of CoO_2 sheets that give a high electronic conductivity and thermoelectric power, and disordered Na layers that give poor thermal conductivity. This suppression of the lattice contribution to the thermal conductivity from the electronic contribution, in addition to high thermoelectric power, is precisely what is sought after in a good thermoelectric material. However, it should also be noted that strong-correlation fluctuations also help to suppress the phonon contribution to the thermal conductivity.

In summary, Na_xCoO_2 is of extreme interest for both technological reasons,

e.g. as a potential thermoelectric material and as a cathode in a Na-ion battery, as well as for a deeper understanding of basic scientific phenomena such as superconductivity and electronic and magnetic transitions in strongly correlated electron systems. In order to better understand the high thermoelectric power, conductivity, and low thermal conductivity in the Na-rich thermoelectric composition, the superconductivity in the hydrated Na-poor composition, and the insulating transition in the $x \approx 0.5$ composition, this and the following chapters investigate the structure, Co valence, and Na ordering in the Na_xCoO_2 system and their role in determining the various properties that are observed.

4.3 Role of Doping and Dimensionality in $\text{Na}_{0.33}\text{CoO}_2 \cdot 1.3\text{H}_2\text{O}$

4.3.1 Introduction

*Superconductivity remains one of the most attractive and challenging areas of research in materials science. The recent report of superconductivity by Takada *et al.* [99] in hydrated Na_xCoO_2 has generated considerable activity and given an unprecedented impulse to the investigation of the fundamental properties of this system. However, an explanation of the role of the water in the occurrence of superconductivity in this material has remained elusive. Superconductivity was found after Na-ion deintercalation below $x \approx 0.42$ and subsequent hydration [99, 91]. H_2O intercalates between the CoO_2 layers, increasing dramatically the lattice spacing and reducing the electronic dimensionality of the structure (the c-axis increases more than 50% over its original value). The proximity to a nonmetallic phase establishes a possible comparison to the hole-doped cuprates, but the CoO_2 planes in Na_xCoO_2 adopt a 2D hexagonal symmetry in contrast to the square coplanar symmetry of

*The contents of this section were published in [9].

CuO₂ planes in the high-temperature cuprate superconductors. On the other hand, the domed shape of the T_c vs. x curve reported by Schaak *et al.* [91] has been questioned in a series of works [16, 67] in which dimensionality is argued to have a strong influence on the appearance of superconductivity.

In this section a systematic and extensive study of the formal valence state of Co versus Na and H₂O contents is presented. In the non-hydrated samples that are studied, the Co valence is much lower than that expected from the Na content. Both thermoelectric power and iodometric titration indicate that oxygen is progressively removed from the structure upon deep Na deintercalation. Our data point to an active role of H₂O in the CoO₂ layers and the removal of oxygen vacancies that would otherwise strongly perturb the periodic potential and prevent superconductivity.

4.3.2 Experimental Section

Polycrystalline Na_{*x*}CoO₂ was prepared by a conventional solid-state reaction. Dried Na₂CO₃ and Co₃O₄ were thoroughly mixed in a molar ratio Na/Co = 0.7 in an Al₂O₃ crucible that was placed directly in a preheated furnace at 850°C to avoid Na evaporation and fired for 12 h in air. A second heat treatment at 900°C was carried out for 12 h in air. After each heat treatment the sample was slowly cooled to room temperature and reground. Na was chemically deintercalated from Na_{0.67}CoO₂ by stirring the powder in a Br₂/CH₃CN oxidizing solution for 5 days at room temperature. Different Br₂ excesses (1- 100) with respect to the stoichiometric amount needed to remove all of the Na were used in order to get a wide range of compositions. The products were washed several times with CH₃CN and acetone, and then dried under vacuum. The Na and Co contents of the phases were determined by inductively coupled plasma optical emission spectroscopy (ICP-OES). The analysis confirms that the amount of Na decreases systematically as the excess of Br₂ increases (Table 4.3).

Table 4.3: Results of the Chemical Analysis of Na_xCoO_2 powder samples.

Na content, x	% Co^{3+}	oxygen content,	
		$2 - \delta$	Br_2 excess
0.690	89.0	1.90	
0.673	77.3	1.95	
0.450	61.0	1.92	x1
0.429	58.9	1.92	x5
0.402	56.6	1.91	x10
0.381	58.1	1.90	x20
0.369	53.8	1.92	x30
0.362	54.2	1.91	x40
0.322	52.2	1.90	x50
0.310	57.0	1.87	x100

The oxidation state of cobalt was determined for all the samples with the iodometric titration method. Superconducting samples were obtained by stirring Na_xCoO_2 , $x < 0.45$, in water for 2 days at room temperature. Thermoelectric power was measured from 85 to 450 K in a homemade setup. Lattice parameters were calculated from the X-ray patterns after indexing all the reflections with Rietica^{**}.

4.3.3 Results and Discussion

Na_xCoO_2 is a highly hygroscopic material, which makes it very unstable under ambient conditions. This, and the unavoidable Na evaporation during the high-temperature synthesis, reduces control over the final stoichiometry and prevents a good characterization of the intrinsic and structural properties for a wide range of x . So, although the unit cell for the most stable phase, $x \approx 0.68$, is considered hexagonal with space group $P6_3/mmc$ (No. 194), hexagonal $R3m$ (No. 160) and monoclinic $C2/m$ (No. 12) have been reported for nearly the same composition [21]. Moreover, ordering of Na vacancies may change the symmetry. In the case of

^{**}Program available at <http://www.rietica.org/>

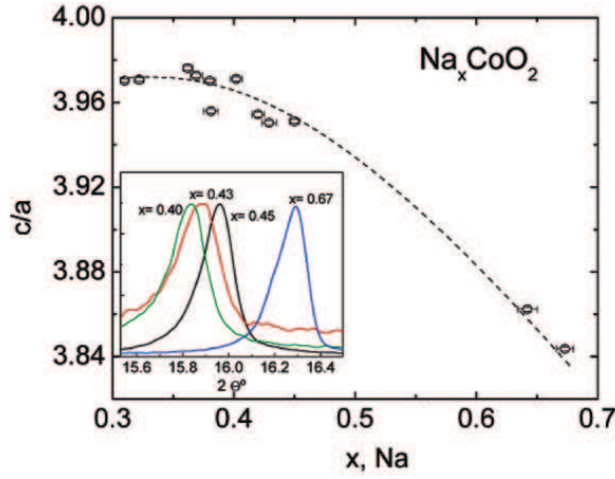


Figure 4.2: Effect of Na content on c/a ratio in the P2 structure of Na_xCoO_2 . Inset: X-ray diffraction for the 002 reflection (c -axis) for various compositions.

superconducting samples, the complexity and controversy are even bigger because a mixture of fully and partially hydrated phases can coexist in the same specimen [16].

We confirmed that the best fits of our powder diffractograms of the parent phase, $x = 0.67$ and 0.69 , were achieved on the basis of a single phase with space group $P6_3/mmc$. On the other hand, to get a good fitting of the diffractograms corresponding to the Na-deintercalated samples, two new minority phases of the hexagonal space groups, $P6_3/m$ (No. 176) and $P6/m$ (No. 175), must be considered in addition to the $P6_3/mmc$ majority phase. The ratio of the c/a lattice parameters as a function of the Na content are shown in Figure 4.2 for the majority phase. A significant increase of the c -axis lattice parameter is observed with decreasing Na content (see the displacement of the (002) reflection in the inset of Figure 4.2) while the a -axis parameter decreases slightly but continuously over the entire sodium content range. This appreciable expansion of the unit cell along the c -axis is due to the decrease in bonding between the CoO_2 layers as Na is removed. Surprisingly, the expansion of the c -axis parameter is less marked below $x \approx 0.4$, leading to an

approximately constant c/a ratio down to $x \approx 0.3$. A similar effect was reported in the related material Li_xCoO_2 and was ascribed to the growing amount of oxygen vacancies that accompanies Li^+ deintercalation [107]. It is of fundamental relevance for the understanding of the magnetic/transport properties of Na_xCoO_2 to know whether a significant amount of oxygen vacancies are also present in this case.

Some groups recently reported the presence of an oxygen content less than stoichiometric in both hydrated [47, 100] and non-hydrated [47, 89] samples of Na_xCoO_2 . However, just a few, very specific compositions were studied in these works, and in the case of the hydrated samples the amount of water present that is not inserted between the layers is difficult to determine, which introduces an important source of error. So, to determine the presence and extent of oxygen vacancies in this material, we have first carried out a meticulous determination of the Co oxidation state in the non-hydrated samples in a wide compositional range. Then, we have related the oxidation state (and hence their actual $\text{Co(IV)}/\text{Co}$ ratio) with the experimentally determined thermopower, which is very sensitive to the effective charge carrier concentration. This allowed us to infer an active role of H_2O in the superconducting samples beyond that of a simple lattice spacer.

We have determined the oxidation state as a function of Na for the non-hydrated samples in the range $0.310 \leq x \leq 0.690$. The samples were dried, all the solutions were previously bubbled with Ar, and the volumetric titration was carried out quickly to avoid any ambient oxidation of I^- . Reproducible iodometric titrations were consistent with an oxidation state of $\text{Co}^{3+/4+}$ that is considerably lower (a larger amount of Co^{3+} and a smaller amount of Co^{4+}) than expected from the Na content determined by ICP-OES. The percentage of Co^{3+} determined experimentally is plotted in Figure 4.3 versus the Na content determined by ICP-OES.

The compound appears to be oxygen deficient, even at the largest doping

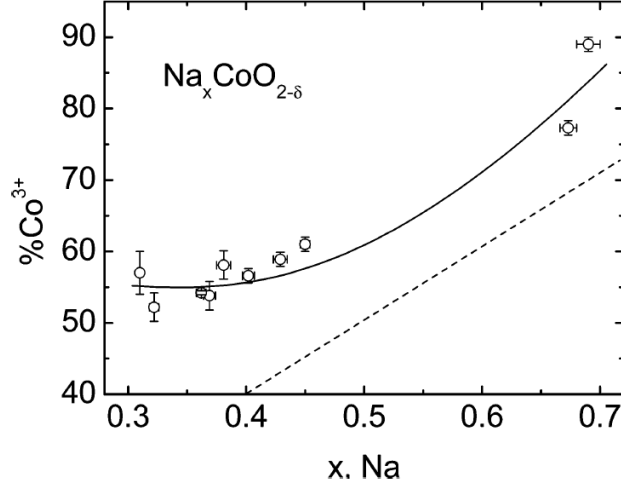


Figure 4.3: Actual Co^{3+} percentage as a function of the Na content.

probed in this work ($x = 0.69$), although the amount of oxygen vacancies (or inserted H^+) increases very much below $x \approx 0.5$. In fact, deintercalation of Na below $x \approx 0.4$ has almost no effect in the final oxidation state of Co, which remains close to $\approx 3.45+$, down to at least $x \approx 0.3$, the lowest Na content probed in this work. The creation of an important number of oxygen vacancies below $x \approx 0.4$ and the consequent reduction of the expected charge of the metallic ions is also consistent with an almost constant c/a ratio (see Figure 4.2).

We note here that the amount of oxygen vacancies present in Na_xCoO_2 samples is highly dependent on the sample type (powder vs. single crystal) and the details of the synthesis. Our results agree with various other groups [48, 47, 46, 69] that have also taken care to measure dry Na_xCoO_2 samples and also found evidence that oxygen vacancies were present in their samples. On the other hand, neutron diffraction experiments carried out by other groups [108] indicate that the oxygen content in the Na_xCoO_2 samples studied is stoichiometric to a precision of 1 to 2% and that therefore the Co oxidation state is solely determined by the Na content. More recently, Choi and Manthiram [18] have shown that for Na_xCoO_2 samples

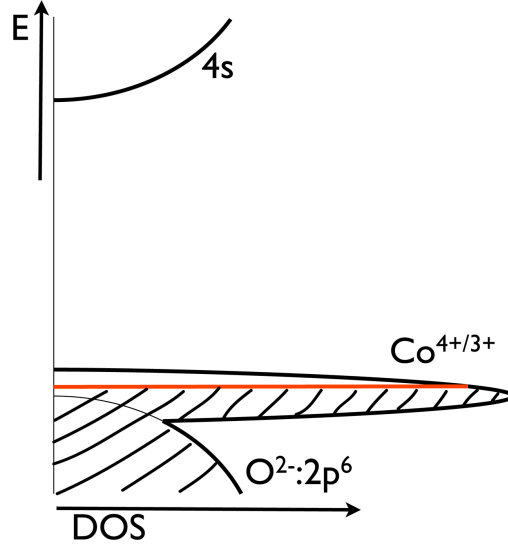


Figure 4.4: Schematic diagram showing the $\text{Co}^{4+/3+}$ redox couple pinned at the top of the $\text{O}^{2-}:2p^6$ band.

deintercalated with NO_2BF_4 a higher oxidation state than the $3.45+$ we report for our Br_2 -deintercalated Na_xCoO_2 samples can be measured.

The loss of oxygen is made possible by a pinning of the $\text{Co}^{3+/4+}:t_{2g}$ band at the top of the $\text{O}^{2-}:2p^6$ band (see Fig. 4.4). In this case, a redox process between the pairs $\text{Co}^{3+/4+}$ and O^-/O^{2-} can occur when holes are actually introduced into the oxygen band. The O^- species form $(\text{O}_2)^{2-}$ at the surface with subsequent loss of oxygen by $2(\text{O}_2)^{2-} \rightarrow \text{O}_2 + 2\text{O}^{2-}$. Marianetti *et al.* [62] proposed an alternative mechanism in which hole-doping at the t_{2g} band rehybridizes the e_g and $\text{O}:2p$ orbitals, which produces an effective hole transfer to the oxygen band and hence the same global redox process described above.

This redox process $\text{Co}^{3+/4+} \longleftrightarrow \text{O}^-/\text{O}^{2-}$ makes it extremely difficult to obtain good control over doping of the CoO_2 layers through variation of the Na content. Similar results of oxygen migration were reported in Li_xCoO_2 , where Venkatraman and Manthiram [107] demonstrated that the maximum oxidation state for Co is also

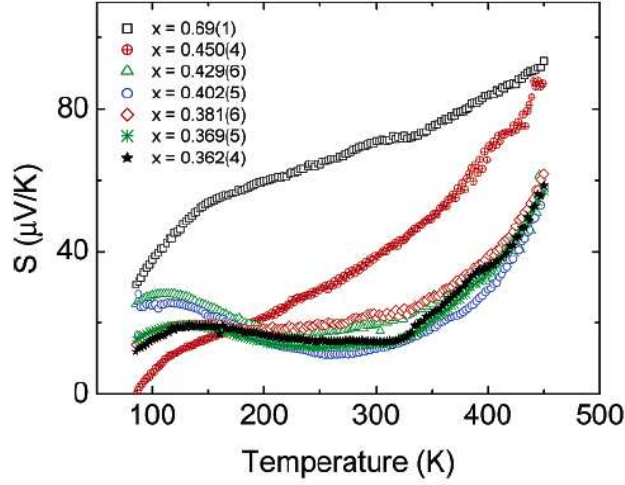


Figure 4.5: Evolution of the temperature dependence of thermopower with Na content.

around 3.5+ even after all the Li^+ was removed from the structure. More recently, Choi and Manthiram [17] showed with prompt gamma activation analysis (PGAA) that chemically delithiating Li_xCoO_2 samples beyond $x < 0.5$ leads to significant proton insertion into the lattice.

To confirm our results that oxygen vacancies accompany Na deintercalation in our Na_xCoO_2 powder samples, we have carried out systematic measurement of the thermoelectric power in the same samples analyzed chemically. Thermopower is the most sensitive electronic transport property of a metal; it is very susceptible to variations in the number of carriers and gives direct information of the asymmetry of the density of states around the Fermi energy. The results for the system $\text{Na}_x\text{CoO}_{2-\delta}$ are shown in Figure 4.5

The samples with high Na content present a thermoelectric power behavior similar to that previously reported by several authors [103, 101]. The thermopower increases with temperature, but the value and the temperature dependence deviates

from what is normally found in a metal with such a low resistivity^{***}. As Na is removed, the thermopower decreases and becomes less temperature dependent, and in the low doping range it remains practically insensitive to variations in Na content. These measurements are fully consistent with the results obtained previously from iodometric titration analysis. The thermopower in the powder is dominated by the ab-plane [103] due to its higher conductivity; the influence of the dimensionality is low, so we are testing the variations in the number of charge carriers available for scattering in the electronically active CoO₂ planes (provided that the material remains metallic) [29]. Hence, the invariance of the thermopower in the low doping region corroborates the inefficiency of Na removal to introduce charge carriers in the CoO₂ layers due to the oxygen loss process in our samples. Therefore, our results show unambiguously through two completely independent methods that a direct relationship between the Na content and the number of holes introduced into the CoO₂ planes does not exist for our Na_xCoO₂ samples. This effect is particularly dramatic at low doping ranges, where superconductivity is found after hydration.

The parallelism with the cuprates in terms of out-of-plane doping control of the in-plane electronic charge is not completely valid in Na_xCoO₂, unless water plays an active role in the doping of the CoO₂ planes. This opens two possibilities for the role of H₂O in the superconductivity.

1. Structural role: H₂O is a passive lattice spacer. Hydrated samples with lower Na content accept more H₂O and become more 2D than those with higher Na content, favoring superconductivity. However, Schaak *et al.* [91] found that although the c-axis expands in the superconducting samples when lowering the Na content, the amount of intercalated H₂O remains constant, about 1.3 molecules per formula unit, independent of x . Moreover, Shi *et al.* [92] re-

^{***}Note: An unusually high asymmetry of the $\epsilon(k)$ *vs.* k dispersion curve about ϵ_F can account for the high thermopower.

ported a decreasing T_c with an increasing c-axis lattice parameter, reflecting the strong controversy among the results.

2. Chemical role: H_2O plays an active role in the doping of the CoO_2 planes. If the oxygen of the intercalated H_2O enters the oxygen vacancies of the CoO_2 planes (as occurs for bound H_2O on the surface of an oxide particle), it gives its protons to the free interstitial water to create $(H_3O)^+$ ions, which reduces the CoO_2 sheets like the addition of Na^+ ions. Moreover, the bound O^{2-} ions from the water decrease the strong perturbations of the periodic potential created by the vacancies and removal of excess protons, inserted in lieu of oxygen vacancies, from the system by the hydration process would oxidize the CoO_2 sheets. In fact, Karppinen *et al.* [47] reported a net increase in the oxidation state of Co as the hydrated superconducting phase is obtained from the corresponding non-hydrated one. If we assume that the water molecules intercalated between CoO_2 layers are electrically neutral and that the $(H_3O)^+$ ions are counterbalanced by the O^{2-} ions that heal the oxygen vacancies, an increase of the oxidation state of Co would explain the continuous increase in the c-axis lattice parameter that is observed in the hydrated samples excess hydrogen is replaced by H_2O that is not active in healing oxygen vacancies, despite the constant amount of water introduced [91].

To check this active role of intercalated H_2O in controlling the oxidation state of the CoO_2 planes, we have monitored the evolution of the thermopower as a non-superconductive sample is hydrated to render the superconductive phase. The results are plotted in Figure 4.6. We have measured the magnetic susceptibility of this hydrated sample to show that it becomes superconducting below $T_c \approx 4$ K. It is important to note that the thermoelectric power only probes variations in the electronic structure of the material, and so variation in the amount of water introduced between the layers is not a source of error for this experiment. From the results

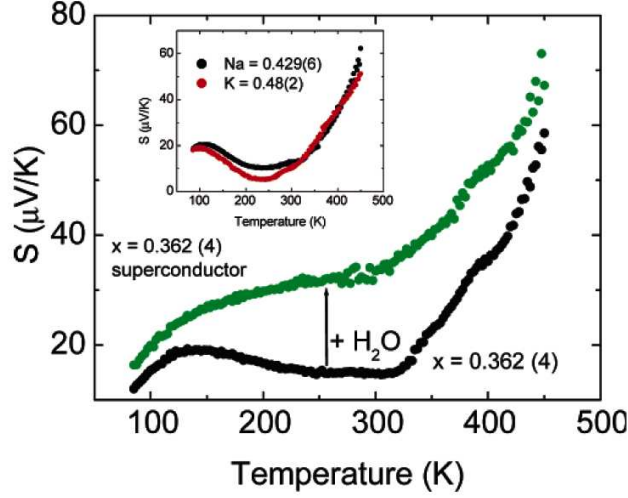


Figure 4.6: Variation of the thermopower due to water intercalation..

previously obtained in dried samples (Figure 4.5), an increase of the thermopower in the superconducting sample (Figure 4.6) is consistent with a substantial change in the oxidation of the CoO_2 planes due to H_2O intercalation. Alternatively, the anisotropic expansion of the structure introduces the possibility of a change in the density of states at the Fermi energy, $N(E_F)$, due to the overlapping of the $e_{+/-}$ and a_1 bands at E_F [85, 93], which could also contribute to the thermopower. To distinguish between these two possibilities, we have synthesized K_xCoO_2 (with structure identical to Na_xCoO_2 except for a larger interlayer spacing in the K samples) and compared the thermopower for two samples with almost identical composition (inset of Figure 4.6). The thermopower presents identical behavior in both materials irrespective of whether the interlayer spacer is Na^+ or K^+ .

It is true that the increase in the c-axis parameter in the K samples with respect to the Na phase is much lower than in the hydrated superconductors, but the thermopower remains practically insensitive to the lattice spacer. This result supports that a change in the oxidation state of the CoO_2 planes and the elimination of oxygen vacancies that strongly perturb the periodic potential by the introduc-

tion of H_2O is a realistic explanation of the role of the water in stabilizing the superconducting state.

From a comparison of Figures 4.5 and 4.6, the increase in the thermopower after water insertion could in principle be interpreted as a signature of reduction instead of oxidation. However, a conclusion like that could be erroneous, especially in a system where the population of more than one band crossing the Fermi energy is changing continuously.

4.3.4 Conclusions

Our results indicate that below $x \approx 0.4$ in Na_xCoO_2 , the formal oxidation state of Co remains constant around $3.45+$, which indicates oxygen loss from and/or H^+ insertion into the $\text{CoO}_{2-\delta}$ layers. We have argued that the water insertion allows the introduction of oxygen into the oxygen vacancies and that the acidic character of a $\text{Co}^{4+}/\text{Co}^{3+}$ oxide would release hydrogen from OH^- groups on the $\text{CoO}_{2-\delta}(\text{OH})_{2\delta}$ layers to the interstitial H_2O to create H_3O^+ ions in the Na layers between CoO_2 layers. In this way the water removes the perturbation of the periodic potential in the CoO_2 layers and makes superconductivity possible. The role of lattice dimensionality is probably important for the occurrence of superconductivity in the hydrated samples by a modification of $N(E_F)$, but our experiments point to H_2O molecules playing a role other than a passive lattice spacer.

Chapter 5

Na and Sr ordering in Na_xCoO_2 and Sr_xCoO_2

5.1 Introduction

In the previous chapter, the structure and properties of Na_xCoO_2 were presented. The P2 structure was shown to have a rich phase diagram that includes a promising thermoelectric material, a hydrated superconductor, and a charge-ordered insulator. Iodometric titration in conjunction with ICP-MS indicated that the oxidation state of Co could not be accurately determined from Na content alone, particularly for Na-poor samples. This difficulty was attributed to the presence of oxygen vacancies in the polycrystalline powder samples that were studied and was presumably a consequence of the instability caused by the pinning of the $\text{Co}^{4+}/^{3+}$ redox couple at the top of the $\text{O}^{2-}:2p^6$ band. Furthermore, thermoelectric power measurements revealed important differences between anhydrous Na_xCoO_2 and $\text{Na}_{0.33}\text{CoO}_2 \cdot 1.3\text{H}_2\text{O}$ that suggest H_2O molecules play a role beyond that of passive lattice spacers in the hydrated superconductor. For example, the idea of H_2O molecules entering the crystal in order to heal oxygen vacancies and restore the periodic potential of the CoO_2

sheets was discussed. It was shown that the relationship between Na content and $\text{Co}^{4+/3+}$ doping is not always straightforward in Na_xCoO_2 samples (whether due to oxygen vacancies or proton insertion), thus shedding light on some of the difficulties that exist in understanding superconducting $\text{Na}_{0.33}\text{CoO}_2 \cdot 1.3\text{H}_2\text{O}$ samples.

On the other hand, this chapter concentrates on the magnetic properties of anhydrous (non-superconducting) Na_xCoO_2 samples. The magnetic susceptibility $\chi(T)$ of anhydrous Na_xCoO_2 polycrystalline powder samples is examined and compared with those of $\text{Sr}_{x/2}\text{CoO}_2$. Such a comparison provides a good opportunity to determine the effect of counter-cation charge (monovalent Na^+ *vs.* divalent Sr^{2+}), number of counter-cations present (x *vs.* $x/2$) for the same degree of doping, as well as counter-cation ordering on the magnetic properties. The $\text{Sr}_{x/2}\text{CoO}_2$ samples are synthesized by ion-exchange reaction from a Na_xCoO_2 parent phase. Interestingly, novel magnetic behavior in the Sr-poor samples ($Sr \approx 0.25$) consisting of a peak in the ZFC susceptibility curve at ≈ 33 K and a large hysteresis between the ZFC and FC curve below the ZFC peak temperature is observed. This magnetic behavior is unexpected in the sense that a Na_xCoO_2 sample with similar structure and doping of the $\text{Co}^{4+/3+}$ couple does not exhibit the same behavior. In order to determine the effect of the annealing treatment during the ion-exchange reaction on the $\text{Sr}_{x/2}\text{CoO}_2$ samples, control samples of the Na_xCoO_2 parent phase were prepared using the same annealing treatment as in the ion-exchange reaction but without the Sr reactant; annealed Na-poor samples were found to exhibit similar magnetic behavior to the Sr-poor samples. The annealing conditions were studied more closely with thermogravimetric analysis (TGA) and x-ray diffraction (XRD). A minority presence of Co_3O_4 as well as a shift of the (002) and (004) XRD peaks to higher 2θ , indicative of a c-axis compression, are found to correspond to a phase segregation of Na-poor Na_xCoO_2 to a majority Na-rich Na_xCoO_2 phase, a minority Co_3O_4 phase, and a loss of O_2 .

Considering the importance of Na ordering on the properties of the well-studied Na_xCoO_2 ($x \approx 0.5$) composition, the Na and Sr ordering in the Na_xCoO_2 and $\text{Sr}_{x/2}\text{CoO}_2$ samples were studied with electron diffraction in a TEM. From simple electrostatic considerations, one would expect $(2a \times 2a)$ ordering for a $1/4$ occupancy of counter-cation sites and $(\sqrt{3}a \times \sqrt{3}a)$ ordering for a $1/3$ occupancy. For the Sr samples, this is precisely what the electron diffraction reveals. In addition, the annealed Na-poor samples that exhibit the same magnetic behavior as the Sr-poor samples also exhibit the same counter-cation superstructure of $(2a \times 2a)$. On the other hand, our x-ray diffraction analysis indicated that the post-annealed phase-segregated Na-rich phase has a Na composition between $0.56 \leq x \leq 0.75$. This does not correspond to a straightforward Na-ordering expected from basic electrostatic consideration. Instead it suggests a mixed-site occupancy of both Na1 and Na2 sites and a possible $1/4$ occupancy of counter-cation vacancies on one of those types of sites.

Finally, Na-rich Na_xCoO_2 powder samples with Na compositions between $0.5 \leq x \leq 0.7$ were synthesized by fine tuning the Na content with a less powerful oxidizer, I_2 instead of Br_2 . Since the oxidative deintercalation is carried out at ambient temperature, the phase segregation and the formation of Co_3O_4 can be avoided. The magnetic susceptibility of these “directly” synthesized Na-rich Na_xCoO_2 samples was measured and compared to the magnetic behavior of the Sr-poor samples and the annealed Na-poor samples. A rich variety of magnetic behavior is observed to exist for compositions between $0.5 \leq x \leq 0.7$, but a Na_xCoO_2 sample with $x \approx 0.56$ is observed to exhibit a magnetic behavior most similar to the Sr-poor samples and the annealed Na-poor samples, although the ZFC peak appears to be shifted to lower T .

5.2 Experimental

5.2.1 Synthesis

As described in the previous chapter, polycrystalline Na_xCoO_2 powder samples with $0.7 \leq x \leq 0.8$ were prepared by solid-state reaction of Na_2CO_3 and Co_3O_4 and their Na content was fine-tuned by oxidative deintercalation in either a $\text{Br}_2/\text{CH}_3\text{CN}$ solution or an $\text{I}_2/\text{CH}_3\text{CN}$ solution. The Br_2 deintercalation was used to produce Na-poor samples with $x \leq 0.48$, whereas the I_2 deintercalation was used to produce Na-rich compositions with $0.5 \leq x \leq 0.7$. By varying the molar excess of Br_2 or I_2 in the acetonitrile solutions, the composition of the Na-poor and Na-rich compositions was controlled.

In addition, following the modified Cushing-Wiley method [21], polycrystalline powder $\text{Sr}_{x/2}\text{CoO}_2$ samples were prepared from selected Na_xCoO_2 polycrystalline powder samples that were made as described above. The general low-temperature ion-exchange reaction is the following:



where 10% molar excess $\text{Sr}(\text{NO}_3)_2$ is used and the reaction is carried out at 360°C for 12 hours in either flowing O_2 or N_2 gas. The final products are washed with distilled water. Control samples of the parent phase Na_xCoO_2 samples used for the ion-exchange reactions were also annealed at 360°C for 12 hours in flowing O_2 or N_2 gas; these samples are referred to as the annealed Na_xCoO_2 samples.

5.2.2 Characterization

X-ray diffraction of the powder samples was carried out with a Philips and an X-pert diffractometer (Cu-K_α radiation). All of the synthesized samples were indexed for the $\text{P6}_3/\text{mmc}$ crystal structure (P2 phase). Their c-axis and a-axis lattice parame-

ters were determined from a fit of each corresponding diffractogram with the MDI Jade software package.*

The Na and Sr contents for these samples were determined with a micromass platform quadrupole inductively-coupled plasma mass spectrometer (ICP-MS) with a hexapole collision/reaction cell and a single Daly-type detector. Na to Co ratios are much more accurate with this technique than with Atomic Absorption Spectroscopy (AAS).

The magnetic behavior of the samples was studied with susceptibility $\chi(T)$ measurements performed on a Quantum Design superconducting quantum interference device (SQUID) magnetometer. $\chi(T)$ curves were measured for samples that were zero-field-cooled (ZFC) and field-cooled (FC) in a measuring field of 100 Oe.

In order to probe whether there existed any Na or Sr superstructure ordering, electron diffraction measurements were made with a JEOL 2010F transmission electron microscope (TEM) operated at 200 kV.

Finally, to study the effects of the annealing conditions on the ion-exchanged samples and the annealed Na_xCoO_2 control samples, thermogravimetric analysis (TGA) was performed on a Na-rich and Na-poor sample.

5.3 Results and Discussion

5.3.1 Structural Analysis

Structural analysis with XRD indicated that all Na_xCoO_2 parent samples as well as the I_2 and Br_2 deintercalated samples derived from them could be indexed for the P2-structure $\gamma\text{-Na}_x\text{CoO}_2$ phase and that the samples were single phase. Fig. 5.1 shows the x-ray diffractogram for a parent phase Na_xCoO_2 sample with $x = 0.78$ indexed for the $\text{P6}_3/\text{mmc}$ (194) crystal structure that corresponds to the P2-structure or γ

*<http://www.materialsdata.com/>

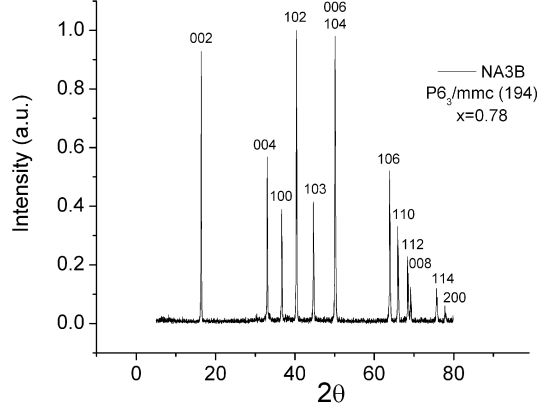


Figure 5.1: X-ray diffractogram for a typical Na_xCoO_2 parent phase, indexed for $\text{P6}_3/\text{mmc}$ (194) crystal structure and corresponding to a Na content of $x = 0.78$.

phase of Na_xCoO_2 . In addition, $\text{Sr}_{x/2}\text{CoO}_2$ and annealed Na-poor Na_xCoO_2 samples could also be indexed for the $\text{P6}_3/\text{mmc}$ (194) crystal structure; however, a minority of Co_3O_4 phase was detected in the x-ray diffractograms of the annealed Na-poor samples.

Chemical analysis with ICP-MS was used to determine accurately the Na to Co ratio, x . Combining the results of the structural analysis with the chemical analysis, it is observed that upon Na deintercalation the structure experiences a large c-axis expansion. The c-axis expansion is most easily observed by the shift of the (004) XRD peak to lower 2θ upon deintercalation. Thus the position of the (004) XRD peak can be calibrated to the ICP-MS chemical analysis and provides a convenient method for determining the Na content x from the XRD data. Fig. 5.2 shows a magnified view of the (004) XRD peak for a series of Na_xCoO_2 samples with Na content ranging from $0.31 \leq x \leq 0.78$, where the Na content x measured with ICP-MS is indicated above each (004) XRD peak. There is a clear correlation between the (004) peak position and the Na content. Likewise, the (002) peak can

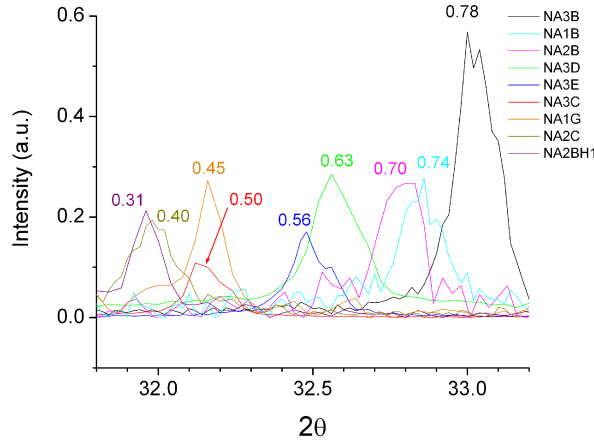


Figure 5.2: A series of x-ray diffractograms for Na_xCoO_2 samples with different Na content, magnified to show the (004) peak and clearly showing the c-axis expansion upon Na-deintercalation (Na content x , determined from ICP-MS chemical analysis, is indicated above each 004 peak)

also be calibrated to Na content x ; however, the (004) peak is more accurate for this purpose because of less error in the XRD measurements taken at higher 2θ .

Similarly, the (100) XRD peak position reflects changes in the a-axis lattice parameter with varying Na content. As can be seen in Fig. 5.3, the structure experiences a small a-axis compression of ≈ 0.025 Å upon Na deintercalation from $x = 0.78$ to 0.31, whereas the c-axis expansion for the same range in x is relatively large (≈ 0.3 Å). Such a trend in the lattice parameters upon Na deintercalation suggests that the holes that are introduced into the $\text{Co}^{4+/3+}$ redox couple are primarily of a_1 -orbital parentage.

The schematic in Fig. 5.4 shows the expected crystal field splitting for a Co^{4+} ion (hole) in an octahedral site where the degeneracy of the d electrons is partially removed by the characteristic t_{2g} and e_g splitting. In addition, the degeneracy of the t_{2g} electrons has been removed by a further splitting into $e_{+/-}$ orbitals that lie primarily in the CoO_2 plane and reflect the hexagonal symmetry of the Co

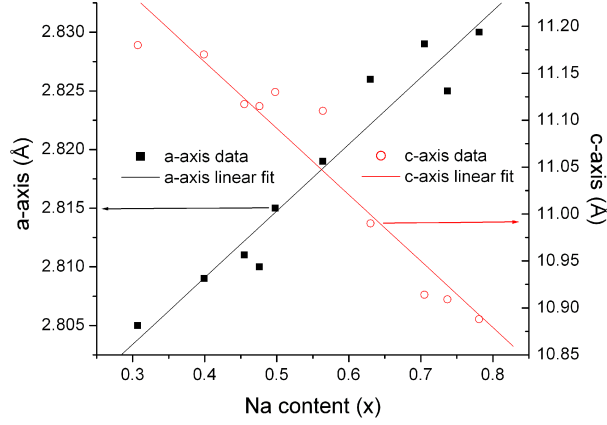


Figure 5.3: C-axis and a-axis lattice parameters for Na_xCoO_2 samples are plotted vs. Na content, clearly showing a large c-axis expansion and a small a-axis compression (note the different scales) upon Na deintercalation.

array in the plane and a_1 orbitals that point out of the CoO_2 plane. The c-axis expansion is a result of the removal of a_1 electrons that participated in bonds along the c-axis through empty Na^+ sp_z orbitals. Alternatively, the c-axis expansion can be attributed to an increased electrostatic repulsion between the O^{2-} layers of neighboring CoO_2 sheets as Na^+ ions are removed. Conversely, the relatively stable a-axis lattice parameter indicates that in the CoO_2 sheets no electrons are being removed from the filled, lower-lying $e_{+/-}$ orbitals of the Co ions. The a_1 orbitals that are pointed out of the plane have little overlap with each other and thus they may be expected to behave like localized electrons; however, hybridization of the t_{2g} electrons with the $\text{O}^{2-}:2p^6$ band introduces enough oxygen character into the a_1 orbitals to give good electronic conductivity in a narrow a_1^* band, as is evidenced by the metallic conductivity discussed in the previous chapter that is higher in the ab -plane than along the c-axis.

A more accurate quantitative determination of the lattice parameters can be achieved with the Jade XRD software package by fitting the entire XRD pattern peak

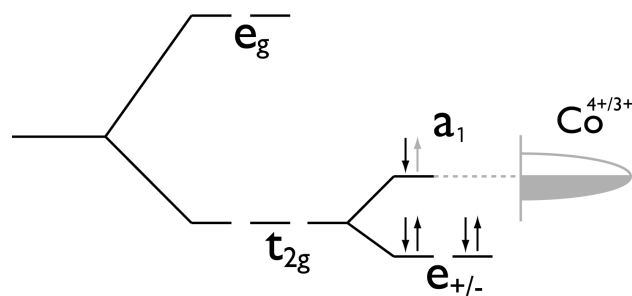


Figure 5.4: Schematic illustration showing that the $\text{Co}^{4+/3+}$ redox couple is primarily of a_1 -orbital parentage. The octahedral coordination removes the degeneracy of the d electrons by splitting into t_{2g} and e_g levels. The degeneracy of the t_{2g} electrons is further removed by the hexagonal symmetry of the CoO_2 sheets into lower-lying $e_{+/-}$ orbitals that lie primarily in the plane and higher energy a_1 orbitals that point out of the plane. Thus, holes introduced into the $\text{Co}^{4+/3+}$ redox couple have primarily a_1 -orbital character.

Table 5.1: Summary of lattice parameters and Na or Sr content in Na_xCoO_2 and Sr_xCoO_2 samples.

Sample	a-axis (Å)	c-axis (Å)	Na/Sr content (x)
NA3B	2.830	10.888	0.781
NA1B	2.825	10.909	0.737
NA2B	2.829	10.914	0.705
NA3D	2.826	10.990	0.630
NA3E	2.819	11.050	0.564
NA3C	2.815	11.130	0.498
NA1C	2.810	11.115	0.476
NA1G	2.811	11.117	0.455
NA2C	2.809	11.170	0.399
NA2BH1	2.805	11.180	0.307
SR1B	2.816	11.518	0.345
SR1C	2.816	11.506	0.284
xNA1G	2.819	11.045	n/a
yNA1G	2.83	10.943	n/a

positions to the $\text{P6}_3/\text{mmc}$ (194) crystal structure and refining the lattice parameters values until the best fit is achieved. Table 5.1 shows the results of the crystal structure refinements with the Jade software for the series of samples studied in this chapter, as well as their Na or Sr content as determined with ICP-MS chemical analysis. The last 4 entries in Table 5.1 correspond to the $\text{Sr}_{x/2}\text{CoO}_2$ samples and the annealed Na-poor Na_xCoO_2 samples that are discussed next.

The structural analysis with XRD for the $\text{Sr}_{x/2}\text{CoO}_2$ samples made by ion-exchange reaction from Na_xCoO_2 parent samples indicates that the $\text{Sr}_{x/2}\text{CoO}_2$ samples are single-phase and isomorphic with the Na_xCoO_2 parent phase, *i.e.* they can also be indexed for the $\text{P6}_3/\text{mmc}$ crystal structure. Chemical analysis on the $\text{Sr}_{x/2}\text{CoO}_2$ samples was used to determine the Sr:Co ratio and confirmed the success of the ion-exchange reaction (Na:Co ratio was less than 0.005). The two $\text{Sr}_{x/2}\text{CoO}_2$ compositions that were studied are listed in Table 5.1. SR1B has a Sr content of

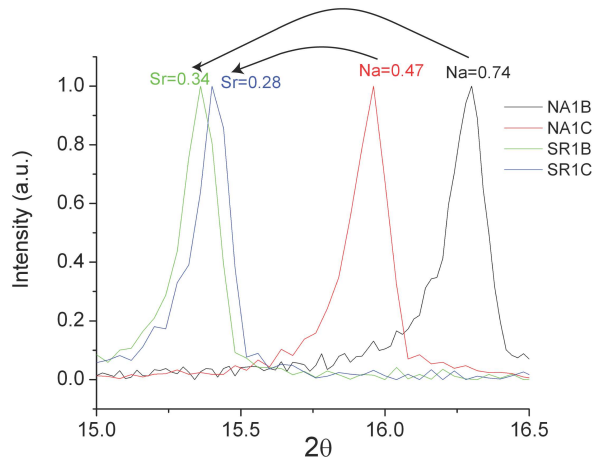


Figure 5.5: X-ray diffractograms of 004 peak for Na_xCoO_2 samples and their corresponding $\text{Sr}_{x/2}\text{CoO}_2$ samples after the ion-exchange reaction. Both samples show a c-axis expansion upon exchanging Na for the larger Sr ion, however also note that the $\text{Sr}_{x/2}\text{CoO}_2$ samples show the opposite trend in c-axis lattice parameter as a function of counter-cation content

0.345 and is referred to as the Sr-rich sample because it was derived from the Na-rich Na_xCoO_2 NA1B sample also listed in Table 5.1. Similarly, SR1C has a Sr content of 0.284 and is referred to as the Sr-poor sample because it was derived from the Na-poor Na_xCoO_2 NA1C sample.

Both the $\text{Sr}_{x/2}\text{CoO}_2$ samples have the same average crystal structure as their Na_xCoO_2 parent structures but with an expanded c-axis lattice parameter and approximately 1/2 the number of counter-cations. Fig. 5.5, which tracks the (004) XRD peak position before and after the ion-exchange reaction, clearly shows the c-axis expansion that occurs as a result of the ion-exchange reaction. Interestingly, the $\text{Sr}_{x/2}\text{CoO}_2$ samples exhibit a trend in the c-axis lattice parameter *vs.* counter-cation content that is opposite to that of the parent Na compounds. This opposite trend is most likely due to the larger and more strongly charged Sr^{2+} ions in the isomorphic structure. In addition, we also note that the Sr-rich sample has slightly less than 1/2 the number of Sr^{2+} ions as Na^+ ions in its parent phase (0.345 *vs.* 0.737). On

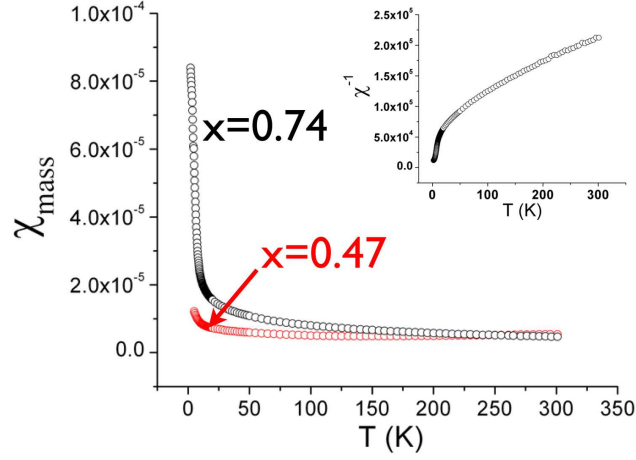


Figure 5.6: Magnetic susceptibility, $\chi(T)$, ZFC curves for a Na-rich sample ($x=0.74$), NA1B, showing Curie-Weiss-like behavior versus a Na-poor sample ($x=0.47$), NA1C, showing Pauli-paramagnetic-like behavior. Upper Right Inset: $\chi^{-1}(T)$ curve for the Na-rich sample showing Curie-Weiss behavior at the higher temperatures.

the other hand, the Sr-poor sample has slightly more than 1/2 the number of Sr^{2+} ions as Na^+ ions in its parent phase (0.284 *vs.* 0.476); in the more empty structure, it appears that it is energetically favorable to pull in slightly more Sr to help relieve the instability of the more oxidized $\text{Co}^{4+/3+}$ redox couple.

Finally, the last two entries in Table 5.1 refer to the majority phase of the annealed Na-poor Na_xCoO_2 samples. The Na content x cannot be determined from ICP-MS for these samples and therefore is marked as not available (n/a); however, the lattice parameters can be calculated from the XRD data, and the calibrated (004) XRD peak position can be used to estimate x as has already been discussed.

5.3.2 Magnetic Behavior

Figure 5.6 shows the magnetic behavior for the Na_xCoO_2 parent samples that were used for the ion-exchange reactions. The Na-rich sample, NA1B, exhibits a larger magnetic susceptibility than the Na-poor sample, NA1C. The magnetic susceptibil-

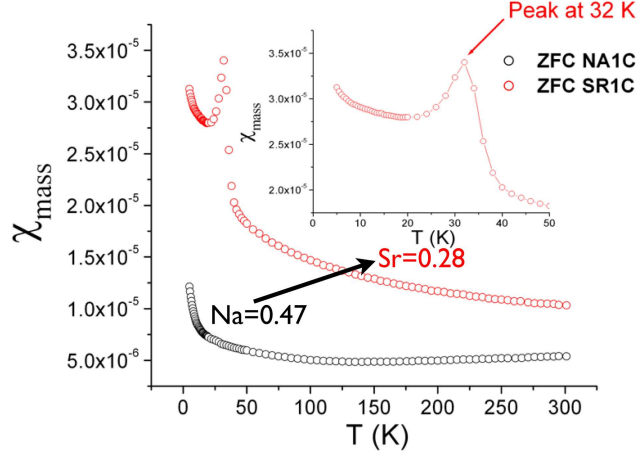


Figure 5.7: Magnetic susceptibility $\chi(T)$ ZFC curves for a Na-poor sample and the corresponding Sr-poor sample after ion-exchange reaction. (Inset) A magnified view of the ZFC curve for the Sr-poor sample clearly showing a peak at ≈ 32 K.

ity of the Na-rich sample increases with decreasing temperature, showing a “Curie-Weiss” behavior (linear $\chi^{-1}(T)$) at the higher temperatures before increasing more sharply at the lower temperatures. The deviation from the Curie-Weiss behavior at the lower temperatures is indicative of a weak ferromagnetism from canted antiferromagnetic spins. On the other hand, the Na-poor sample does not follow a Curie-Weiss behavior and is better described by a flat “Pauli paramagnetic” susceptibility with strong correlation fluctuations.

For the $\text{Sr}_{x/2}\text{CoO}_2$ samples, one might expect a similar behavior of $\chi(T)$ to that of their parent Na_xCoO_2 samples since they have approximately the same doping. However, the ion-exchange reaction results in novel magnetic behavior in both of the Sr samples, especially the Sr-poor sample. Fig. 5.7 shows the change in $\chi(T)$ upon substituting Sr for Na in the Na-poor sample NA1C. An overall increase in $\chi(T)$ is apparent, as well as the emergence of a peak in the ZFC $\chi(T)$ curve that appears at ≈ 32 K. Taking an even closer look at the magnetic behavior of the Sr-poor sample, Fig. 5.8 shows both the ZFC and FC $\chi(T)$ curves for the Sr-poor

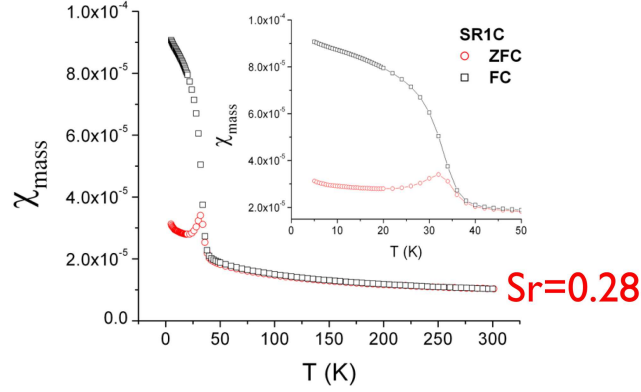


Figure 5.8: Typical magnetic behavior for a Sr-poor sample, exhibiting a large hysteresis between the ZFC and FC $\chi(T)$ measurements and a peak in the ZFC curve at 32 K (see Inset).

SR1C sample. A large hysteresis between the ZFC and FC curves is observed, with the peak in the ZFC curve occurring at a slightly lower temperature (≈ 3 K lower) than where the splitting begins.

Although the magnetic behavior of the Sr-rich sample (SR1B) resembles much more closely that of its parent Na-rich sample (NA1B), a closer examination of both the ZFC and FC curves also reveals similar features to that of the Sr-poor sample, although less pronounced. Fig. 5.9 shows the $\chi(T)$ curves for SR1B and reveals a slight hysteresis between the ZFC and FC curves as well as a very small (or broader) peak in the ZFC curve. Whereas the splitting in the ZFC and FC curves occurs at approximately the same T , the ZFC peak is definitely shifted to a lower T (≈ 21 K).

In order to determine the effect of the annealing treatment during the ion-exchange reaction, the susceptibility $\chi(T)$ curves were also measured for the control samples of Na_xCoO_2 annealed under the same conditions (360 °C for 12 hours) but without the addition of the Sr precursor ($\text{Sr}(\text{NO}_3)_2$). Fig. 5.10 shows a very similar magnetic behavior between the annealed Na-poor control samples (xNA1G and yNA1G) and the Sr-poor sample (SR1C). The peak in the ZFC curves is observed

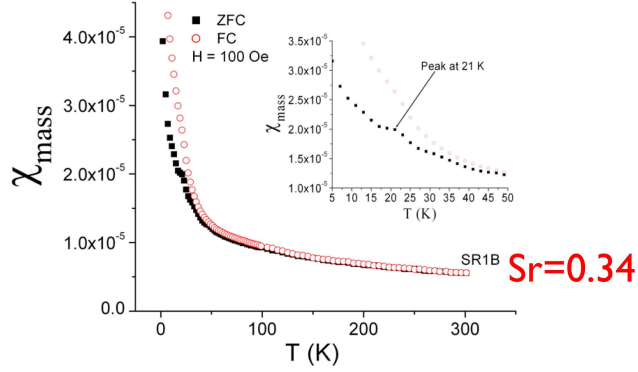


Figure 5.9: Typical magnetic behavior for a Sr-rich sample, exhibiting almost no hysteresis between the ZFC and FC $\chi(T)$ measurements and a small peak in the ZFC curve at 21 K (see Inset).

for all three samples between 32 and 35 K; the annealed Na-poor samples exhibit the peak at slightly higher T than the Sr-poor sample, and the N₂-annealed sample (yNA1G) has a broader less pronounced peak.

The very similar magnetic behavior between the Sr-poor sample and the annealed Na-poor samples suggests that an important similarity exists between the two types of samples. On the one hand, the magnetic behavior appears to be independent of the degree of doping in the samples since the Sr-poor sample has very close to the same doping as its parent Na-poor Na_{*x*}CoO₂ sample, yet their magnetic behavior is markedly different. This leaves two possibilities for the similar magnetic behavior of the Sr-poor and annealed Na-poor samples: (1) their magnetic behavior is due to a common phase that forms during the heating treatment of the samples, or (2) the magnetic behavior is due to a Na or Sr ordering that results in a superstructure that affects the physical properties, as in the Na_{*x*}CoO₂ ($x \approx 0.5$) single crystal samples that have been well-studied in the literature. The first idea of a phase segregation is discussed in the next section, while the Na and Sr ordering observed with electron diffraction is presented and discussed in the following section. Finally, the magnetic behavior of Na-rich samples “directly” synthesized with I₂

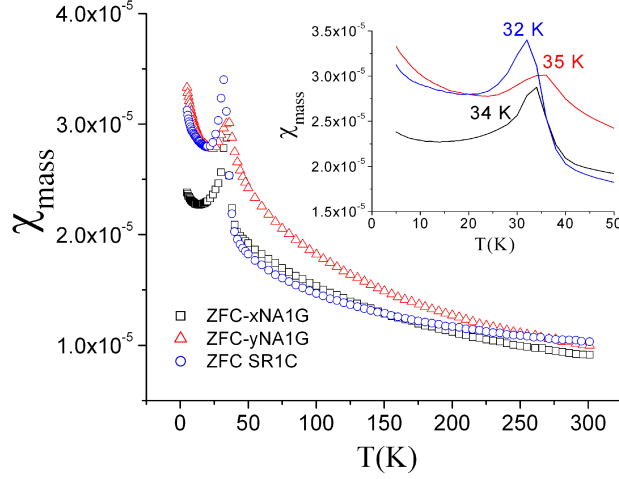


Figure 5.10: ZFC $\chi(T)$ curves for Na-poor samples after annealing, showing very similar behavior to a Sr-poor sample. Sample xNA1G was annealed in flowing O_2 and sample yNA1G was annealed in flowing N_2 . (Inset) Magnified view of the ZFC peak that is observed between 32-35 K.

deintercalation is presented and compared to the Sr-poor and annealed Na-poor samples.

5.3.3 Phase segregation

It is already well understood that a Li-poor sample is unstable due to the pinning of the $Co^{4+/3+}$ redox couple that occurs at the top of the $O^{2-}:2p^6$ band (see Fig. 4.4). In the Li_xCoO_2 cathode of rechargeable Li-ion batteries this instability limits the battery to half of its theoretical capacity. This is because delithiation in Li_xCoO_2 , rather than resulting in an oxidation state greater than $Co^{3.5+}$ for $x < 0.5$, instead leads to oxygen vacancy formation, or to proton insertion, as has been recently demonstrated in NO_2BF_4 chemically-delithiated samples [17]. For Li_xCoO_2 this instability occurs for oxidation states approximately greater than $Co^{3.5+}$ ($x < 0.5$) for both electrochemically and chemically delithiated samples. On the other hand, for some Na_xCoO_2 samples, *e.g.* powder samples Na-deintercalated with NO_2BF_4

[18], a higher oxidation state can be measured if care is taken to measure the samples before they become hydrated. Thus, it appears that in Na_xCoO_2 samples, the instability that occurs below ($x < 0.5$) is preferentially relieved by pulling in H_2O molecules into the structure rather than creating oxygen vacancies or pulling in protons. The mechanism by which the instability caused by the pinning of the $\text{Co}^{4+/3+}$ redox couple at the top of the $\text{O}^{2-}:2p^6$ band is relieved is dependent on the sample composition (Na_xCoO_2 *vs.* Li_xCoO_2), sample type (single crystal, powder, or flux crystal), as well as the deintercalation process (electrochemical, chemical, type of oxidizer, etc.). However, what is clear is that the $\text{Co}^{4+/3+}$ redox couple is unstable in a high oxidation state.

Figure 5.11 shows that a Na-rich ($x \approx 0.70$) sample exhibits much greater stability than a Na-poor ($x \approx 0.40$) sample upon heating in air during a TGA experiment. The Na-rich sample shows a small ≈ 1 wt% loss upon heating beyond the ion-exchange reaction annealing temperature (360°C) up to 400°C ; its greater stability is expected since it corresponds to a less oxidized state of $\text{Co}^{3.3+}$. On the other hand, the Na-poor sample that is in a considerably higher oxidation state shows a much larger wt% loss upon heating up to the same temperature. This is in agreement with TGA plots of $\text{Na}_{0.32}\text{CoO}_2$ measured by Choi [18].

Whereas the XRD pattern for the Na-rich sample before and after the annealing experiment does not show any changes, the Na-poor sample shows a definite shifting of the (004) peak to higher 2θ as well as the emergence of a minority Co_3O_4 minority phase. Fig. 5.12 shows the shift of the (004) XRD peak for a Na-poor sample to higher 2θ during annealing in either an O_2 or N_2 atmosphere. The emergence of a minority Co_3O_4 phase and shifting of the (004) XRD peak to higher 2θ corresponds to a phase segregation of the original Na-poor sample into a Na-poor phase (Co_3O_4 , *i.e.* no Na) and a Na-rich phase with a shifted (004) XRD peak. Such a phase segregation involves an evolution of O_2 and associated weight loss

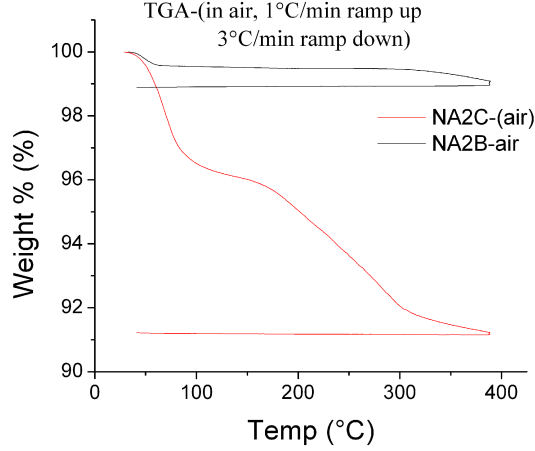


Figure 5.11: TGA for a Na-rich, NA2B, sample, and a Na-poor sample, NA2C, showing the instability in the Na-poor sample under the annealing conditions.

that can be measured with TGA (see Fig 5.11) and corresponds to the following phase segregation reaction for the NA2C sample measured with TGA:



The Na content ($x = 0.4$) of the original Na-poor sample NA2C was determined directly by ICP-MS (see Table 5.1) and the Na content ($x \approx 0.56$) of the Na-rich phase after annealing is estimated from the calibrated (004) XRD peak position of the majority phase of an annealed Na-poor sample, *e.g.* see xNA1G in Table 5.1. Then if we assume that no Na is lost during the anneal, we calculate (A)=0.7. Likewise, if we assume that no Co is lost during the anneal, we calculate (B)=0.1. This results in (C)=0.1, and corresponds to a 3.2 wt% loss. Referring back to Fig 5.11, the total weight% loss of ≈ 8.5 wt% that is measured is much greater than our calculation; however, if the initial weight% loss of ≈ 5 wt% is attributed to absorbed water as has been shown elsewhere [18], then our calculation agrees well with the experimental data. Therefore, it appears that even low-temperature

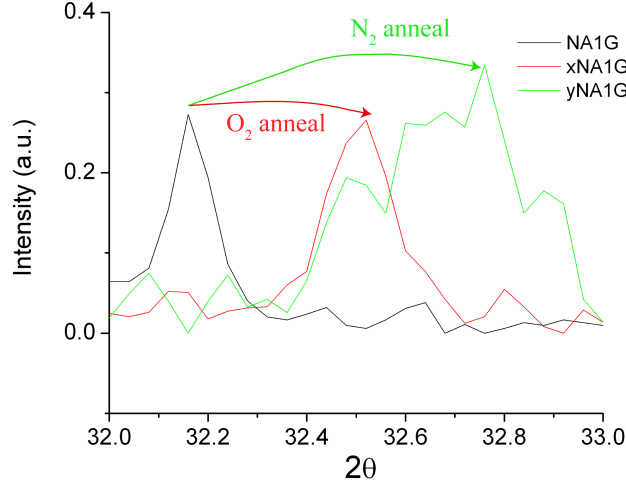


Figure 5.12: X-ray diffractograms of (004) peak of a Na-poor sample before and after N_2 and O_2 annealing treatment at same T as the ion-exchange reaction.

annealing of Na-poor samples can lead to phase segregation into a higher Na content phase, Co_3O_4 , and an associated evolution of O_2 . Furthermore, the phase-segregated Na-rich phase may favor a particular Na-order that has a pronounced affect on the magnetic properties, such as $\chi(T)$; we investigate and discuss the roll of Na and Sr ordering in the following section.

5.3.4 Na and Sr ordering and superstructure

Electron diffraction is a powerful technique for determining Na and Sr ordering that may not be discernible with x-ray powder diffraction alone. Considering the importance of Na order ($2a \times \sqrt{3}a$) on the electronic properties of Na_xCoO_2 ($x \approx 0.5$) [112, 40], the Na and Sr ordering in the parent Na_xCoO_2 , the deintercalated Na_xCoO_2 , the ion-exchanged $Sr_{x/2}CoO_2$, as well as the annealed Na-poor Na_xCoO_2 samples were studied by electron diffraction in the TEM and the results are presented here. Due to their layered structure, TEM samples were easily prepared from the powder samples by dispersing with acetone on a Cu TEM grid with

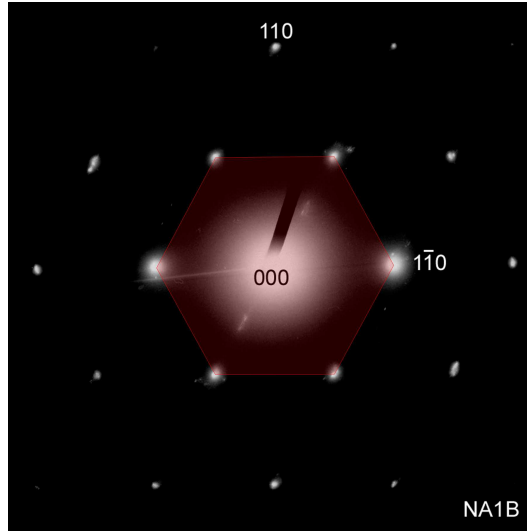


Figure 5.13: Electron Diffraction pattern for a Na-rich parent phase where the red overlay is a guide to distinguish the unit cell and superstructure reflections due to Na ordering. A weak superstructure is observed along a single a -axis $\langle 100 \rangle$ direction.

a lacey-carbon support film. The dispersed samples were easily oriented along the $[001]$ zone axis with minor sample tilting adjustments. The ease of orienting the powder samples along the $[001]$ zone axis provides a convenient way for probing the Na and Sr ordering that exists in the ab -plane.

Fig. 5.13 shows a typical electron diffraction pattern for a Na-rich Na_xCoO_2 parent phase, in this case sample NA1B, that has been indexed and marked with a hexagonal red overlay that is guide for finding the $(a \times a)$ unit cell of the ab -plane. Since the electron diffraction pattern is essentially a map of the reciprocal space, any diffraction spots that are found within the hexagonal red overlay would arise from a periodic ordering that is greater than the a lattice parameter of the unit cell and would thus correspond to a superstructure from Na or Sr ordering that may or may not be commensurate with the hexagonal Co lattice. As compared to the electron diffraction patterns of the Sr and annealed Na-poor samples (presented next), the Na-rich Na_xCoO_2 parent phase of Fig. 5.13 does not present a strong

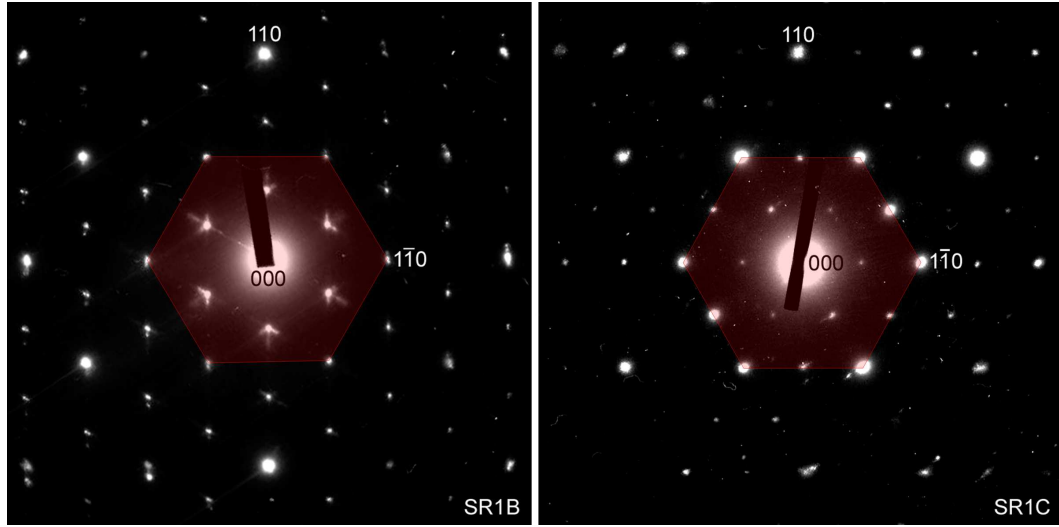


Figure 5.14: Electron Diffraction patterns for Sr-rich ($\text{Sr}_{0.34}\text{CoO}_2$) and Sr-poor ($\text{Sr}_{0.28}\text{CoO}_2$) samples where the red overlays is a guide to distinguish the unit cell and the superstructure reflections due to Sr ordering. A strong superstructure is observed for both samples and corresponds to a $(\sqrt{3}a \times \sqrt{3}a)$ superstructure for the Sr-rich sample (left) and a $(2a \times 2a)$ superstructure for the Sr-poor sample (right).

superstructure, although a superstructure reflection along the $\langle 010 \rangle$ direction is discernible.

In contrast to the Na_xCoO_2 parent samples, both of the ion-exchanged Sr samples exhibit pronounced Sr ordering and distinct superstructures. Fig. 5.14 shows electron diffraction patterns for the Sr-rich SR1B sample (left panel) and the Sr-poor SR1C sample (right panel). Both of these ED patterns contain strong superstructure reflections clearly visible within the red hexagonal overlay defined by the $(a \times a)$ unit cell. The Sr-rich sample contains superstructure reflections that are $1/3$ the reciprocal distance of the (110) diffraction spots. This type of superstructure corresponds to $(\sqrt{3}a \times \sqrt{3}a)$ Sr ordering and agrees well with results obtained by Yang [111]. The $(\sqrt{3}a \times \sqrt{3}a)$ super cell is not commensurate with the original $(a \times a)$ unit cell but *is* commensurate with the original lattice because it is rotated 30° with respect to the original $(a \times a)$ unit cell. In addition to the $(\sqrt{3}a \times \sqrt{3}a)$

superstructure, some satellite reflections surrounding the $1/3$ (110) superstructure reflections can be observed in the ED pattern and may be a result of the super cell being incommensurate with the original ($a \times a$) unit cell.

On the other hand, the Sr-poor sample (right panel of Fig. 5.14) contains superstructure reflections that are $1/2$ the reciprocal distance of the (100) diffraction spots and correspond to ($2a \times 2a$) Sr-ordering. In contrast to the ($\sqrt{3}a \times \sqrt{3}a$) Sr ordering of the Sr-rich sample, the super cell here is commensurate with both the original ($a \times a$) unit cell and the lattice and is not rotated with respect to the original unit cell. Accordingly, no satellite reflections are observed surrounding the superstructure reflections. Most importantly, it should be noted that this Sr-poor sample is the one that exhibited the novel magnetic behavior consisting of a splitting of the ZFC and FC $\chi(T)$ curves at low T and a peak in the ZFC curve at slightly lower T . In order to determine whether the ($2a \times 2a$) ordering plays an important role in determining these magnetic characteristics, electron diffraction was also used to probe the Na order in the annealed Na_xCoO_2 samples that exhibited a similar magnetic behavior.

Fig. 5.15 shows the electron diffraction pattern for the annealed Na-poor sample NA1G; it also clearly corresponds to ($2a \times 2a$) ordering. Therefore, it appears that this type of ordering is critical for obtaining the magnetic properties that we observe. However, whereas for the Sr samples we could be certain of the counter-cation occupancy (0.34 and 0.28), for the annealed Na_xCoO_2 samples we cannot measure x directly from ICP-MS due to the phase segregation that occurs during annealing and the presence of the minority Co_3O_4 phase. On the other hand, we do know that the ED pattern comes from the phase segregated Na-rich Na_xCoO_2 (majority phase), and from the calibrated position of the (004) XRD peak, we can estimate $x \approx 0.56$.

The superstructures observed for the Sr samples are what is expected from

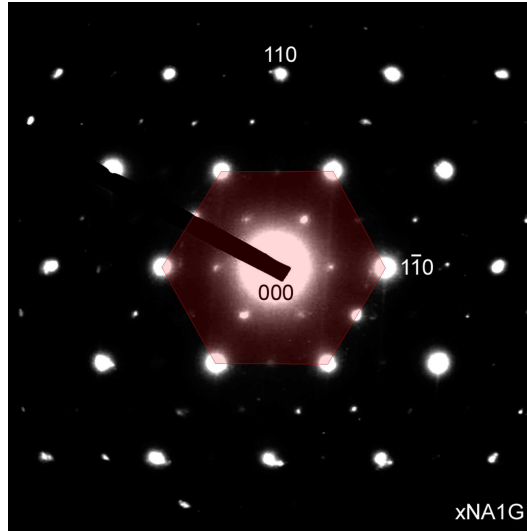


Figure 5.15: Electron Diffraction pattern for an annealed Na-poor sample where the red overlay is a guide to distinguish the unit cell and superstructure reflections due to Na ordering. A strong superstructure is observed and corresponds to a $(2a \times 2a)$ superstructure similar to the superstructure observed for Sr-poor samples.

a simple electrostatic argument for those particular Sr-occupancies. For example, for the Sr-rich Sr_xCoO_2 SR1B sample, we know from ICP-MS that $x \approx 0.34$. This is very close to a $1/3$ occupancy of the counter-cation sites. From an electrostatic argument, the Sr^{2+} ions would prefer to occupy the Sr2 trigonal prismatic sites that share edges with neighboring Co octahedra rather than the Sr1 trigonal prismatic sites that share faces with the Co octahedra. Then the lowest energy configuration will be achieved for Sr^{2+} ions occupying Sr2 sites that are maximally dispersed between CoO_2 sheets. Such a configuration is shown in the schematic of Fig. 5.16 and corresponds to a $(\sqrt{3}a \times \sqrt{3}a)$ superstructure, which agrees with our experimental observations. Similarly, for the Sr-poor Sr_xCoO_2 SR1C sample we measure $x \approx 0.28$ with ICP-MS, which is closer to a $1/4$ occupancy of the counter-cation sites. Again, by a simple electrostatic argument we expect the Sr2 sites to be preferentially filled and the Sr^{2+} ions to be maximally dispersed. For this case, the lowest energy

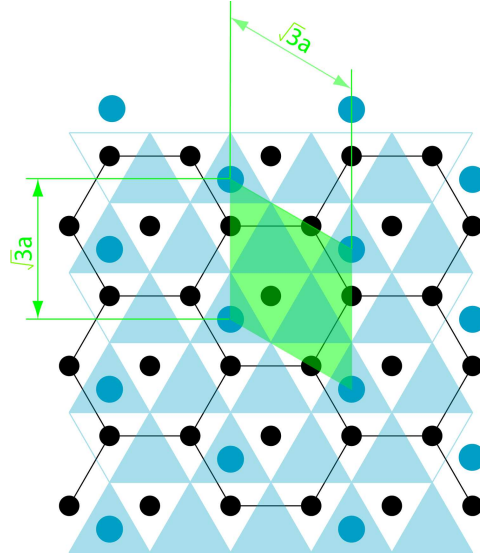


Figure 5.16: Schematic showing 1/3 occupancy of counter cation sites and the corresponding ($\sqrt{3}a \times \sqrt{3}a$) superstructure, where black circles represent a plane of Co ions, blue circles represent a layer of the ordered counter cations, and the vertices of the blue triangles correspond to oxygen ions (filled-in triangles mark Na2 sites; empty triangles mark Na1 sites).

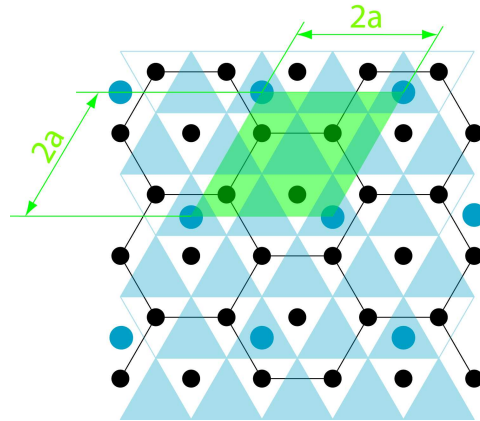


Figure 5.17: Schematic showing 1/4 occupancy of counter cation site and the corresponding ($2a \times 2a$) superstructure, where black circles represent a plane of Co ions, blue circles represent a layer of the ordered counter cations, and the vertices of the blue triangles correspond to oxygen ions (filled-in triangles mark Na2 sites; empty triangles mark Na1 sites).

structure is shown in Fig.5.17 and corresponds to a (2a x 2a) superstructure.

On the other hand, for the annealed Na_xCoO_2 samples a simple electrostatic analysis is not as straightforward for several reasons; there is greater uncertainty in the value of x calculated from the calibrated (004) XRD peak position, the electrostatic repulsion between Na^+ ions is less compared to that of the Sr^{2+} ions, the counter-cation planes are more crowded since $x > 0.5$, and the counter-cation occupancy x is not close to a simple fractional filling, *e.g.* 1/4, 1/3, or 1/2, that gives a straightforward lowest energy arrangement. For these reasons, it is not surprising that neutron diffraction studies for Na_xCoO_2 samples with $x > 0.5$ have shown mixed occupancy of both the Na2 and Na1 sites with the Na2 sites preferentially occupied [42, 23, 58, 45], *e.g.* Na2:Na1 = 2.5 for $\text{Na}_{0.75}\text{CoO}_2$ samples studied by Huang [42].

The annealed Na-poor sample of Fig. 5.15 indicates some type of (2a x 2a) ordering similar to the Sr-poor sample of Fig. 5.14, but the question is what kind of ordering is giving the (2a x 2a) superstructure in the annealed Na_xCoO_2 samples that we estimate to have $x \approx 0.56$? Taking into consideration the mixed site occupancy results from the neutron diffraction experiments, our interpretation of the ED pattern is that the $x \approx 0.56$ sample has ≈ 0.75 occupancy of the Na2 sites and ≈ 0.37 occupancy of the Na1 sites. This is consistent with the preferential occupancy of Na2 sites observed with neutron diffraction and also accounts for a (2a x 2a) superstructure that results from a 3/4 occupancy of Na2 sites (1/4 Na2 vacancies) and a configuration analogous to the $\text{Sr} \approx 1/4$ occupancy discussed for the Sr poor samples and schematically depicted in Fig. 5.17.

Our investigation into determining the most important factor for obtaining the magnetic behavior observed for the Sr-poor and annealed Na-poor samples is strongly related to the counter-cation ordering and subsequent superstructures that are formed. Whereas the phase segregation that occurs during annealing can be

responsible for forming the ordered Sr or Na phase that gives the interesting magnetic properties, the critical factor is the formation of a (2a x 2a) superstructure, whether it be from $\approx 1/4$ occupancy of Sr2 sites in the Sr-poor Sr_xCoO_2 samples or $\approx 3/4$ occupancy of Na2 sites in the majority Na_xCoO_2 phase of the annealed Na-poor samples that we estimate to have $x \approx 0.56$.

5.3.5 I₂-deintercalated Na-rich Na_xCoO_2 samples

In order to avoid the complications of working with a mixed two phase sample, *e.g.* the annealed Na-poor samples that contain a minority Co_3O_4 and a majority $\text{Na}_{x \approx 0.56}\text{CoO}_2$ phase, we “directly” synthesized and studied the magnetic behavior of Na-rich Na_xCoO_2 samples with $0.5 < x < 0.7$. For these samples, chemical deintercalation was carried out using the less powerful oxidizer I_2 (instead of Br_2) in an acetonitrile solution, stirring at room temperature for a minimum of 2 days. Because the chemical deintercalation is carried out at room temperature, the phase segregation and subsequent formation of Co_3O_4 is avoided. XRD analysis for samples NA3D ($\text{Na}_{0.63}\text{CoO}_2$) and NA3E ($\text{Na}_{0.56}\text{CoO}_2$) confirmed that they were single phase (P2 structure). The goal of making these samples was to “directly” synthesize a Na-rich composition that exhibited the same magnetic behavior as the annealed Na-poor samples, and thereby confirm that the magnetic behavior was not attributable to the minority Co_3O_4 composition. In addition, the samples provide an opportunity to measure x directly with ICP-MS rather than having to indirectly determine x using the calibrated (004) XRD peak position.

Figure 5.18 shows the magnetic susceptibility $\chi(T)$ for the two Na_xCoO_2 samples NA3D ($\text{Na}_{0.63}\text{CoO}_2$) and NA3E ($\text{Na}_{0.56}\text{CoO}_2$). The NA3D sample (left panel) that is closer to the Na-rich parent composition has a very similar $\chi(T)$ behavior with “Curie-Weiss” behavior typical of those samples (see Fig. 5.6); however, upon closer inspection (left panel upper right inset) we see that the $\chi(T)$ curves exhibit

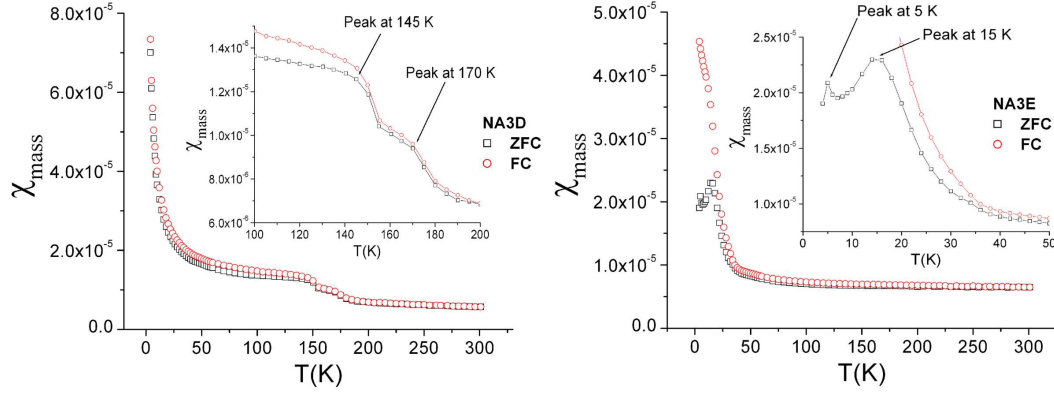


Figure 5.18: $\chi(T)$ curves for I_2 -deintercalated samples, (Left panel) NA3D, $x=0.63$, sample, (Right panel) NA3E, $x=0.56$, sample.

some features of interest, two broad peaks at approximately 170 K and 145 K as well as a small splitting of the ZFC and FC curves below the lower peak temperature.

The NA3E sample (right panel) has the $\chi(T)$ behavior most similar to those of the Sr-poor samples (Fig. 5.8) and the annealed Na-poor samples (Fig 5.10). It exhibits a clear splitting of the ZFC and FC $\chi(T)$ curves and a pronounced peak in the ZFC curve similar in character to those samples (right panel upper right inset), except that the ZFC peak is suppressed to a lower temperature of 15 K (*vs.* ≈ 33 K) and there is a small additional feature at $T \approx 5$ K. The similarities between the $\chi(T)$ curves for the “directly” synthesized NA3E $\text{Na}_{0.56}\text{CoO}_2$ that are single phase and show no evidence of Co_3O_4 and the annealed Na-poor samples (xNA1G, yNA1G) that we estimate to consist of a majority Na_xCoO_2 ($x \approx 0.56$) phase strongly supports that the magnetic behavior of these samples is indeed intrinsic to a composition with $x \approx 0.56$.

5.4 Conclusions

Counter-cation ordering plays a critical role in determining the magnetic behavior such as $\chi(T)$ in Na_xCoO_2 and Sr_xCoO_2 . In particular, Sr_xCoO_2 samples with

$x \approx 1/4$ probed with electron diffraction showed Sr ordering with a $(2a \times 2a)$ superstructure and a complex magnetic behavior characterized by a peak in the ZFC $\chi(T)$ curve at ≈ 32 K and a splitting of the ZFC and FC curves a few K above this temperature. This type of $(2a \times 2a)$ ordering agrees well with a simple electrostatic calculation based on $1/4$ occupancy of the Sr2 counter-cation sites. On the other hand, Sr_xCoO_2 samples with $x \approx 1/3$ showed a $(\sqrt{3}a \times \sqrt{3}a)$ superstructure with magnetic behavior much more similar to its parent Na_xCoO_2 sample.

Annealed Na-poor Na_xCoO_2 samples also exhibited essentially the same magnetic behavior as the Sr-poor Sr_xCoO_2 sample. The Na-poor Na_xCoO_2 samples were shown to undergo a phase segregation due to the annealing conditions that resulted in a Na-rich Na_xCoO_2 phase with $x \approx 0.56$, Co_3O_4 , and the evolution of O_2 . The Na-rich phase was probed with electron diffraction and was also found to exhibit a $(2a \times 2a)$ superstructure. While a simple electrostatic calculation is not as straightforward for the Na samples that are known to have mixed occupancy of both Na1 and Na2 sites, we find the possibility of the $(2a \times 2a)$ superstructure arising from $1/4$ vacancy ordering on Na2 sites consistent with site occupancies measured by neutron diffraction and reported in the literature.

Finally, by comparison to the measured $\chi(T)$ of single phase Na_xCoO_2 “directly” synthesized by I_2 deintercalation and tuned to $x \approx 0.56$, we conclude that the novel magnetic behavior that is observed in both the Sr-poor samples and annealed Na-poor samples is strongly correlated to the $(2a \times 2a)$ superstructure that develops as a result of either $1/4$ occupancy of Sr ions on Sr2 sites or $1/4$ occupancy of Na vacancies on Na2 sites.

Chapter 6

A model for Na_xCoO_2 ($x \approx 0.5$)

6.1 Introduction

In the previous chapter, it was shown that Na and Sr ordering play an important role in determining the magnetic properties of Na_xCoO_2 and Sr_xCoO_2 . In particular, it was shown that Sr_xCoO_2 samples with $x \approx 1/4$ and Na_xCoO_2 samples with $x \approx 0.56$ exhibited a $(2a \times 2a)$ superstructure that gave rise to a peak in the ZFC $\chi(T)$ curve and a splitting of the ZFC and FC curves. From electrostatic calculations and neutron diffraction results reported in the literature [23, 58, 45], a preferential occupancy of the Sr2 and Na2 sites that share edges (rather than faces) with the Co octahedra is expected and accounts for the $(2a \times 2a)$ order; in the Sr_xCoO_2 samples, it is attributable to 1/4 occupancy of Sr2 sites, and in the Na_xCoO_2 samples, it is attributable to 1/4 occupancy of Na vacancies on Na2 sites.

On the other hand, numerous studies [29, 112, 40, 109] have shown that Na_xCoO_2 ($x \approx 0.5$) has a well-ordered $(2a \times \sqrt{3}a)$ orthorhombic superstructure with equal occupancy of the Na2 and Na1 sites, even at ambient temperature. Although early excitement in Na_xCoO_2 was focused on the superconductive $\text{Na}_{0.33}\text{CoO}_2 \cdot 1.3\text{H}_2\text{O}$ phase [91, 99], mapping of the Na_xCoO_2 phase diagram (see Fig. 6.1) re-

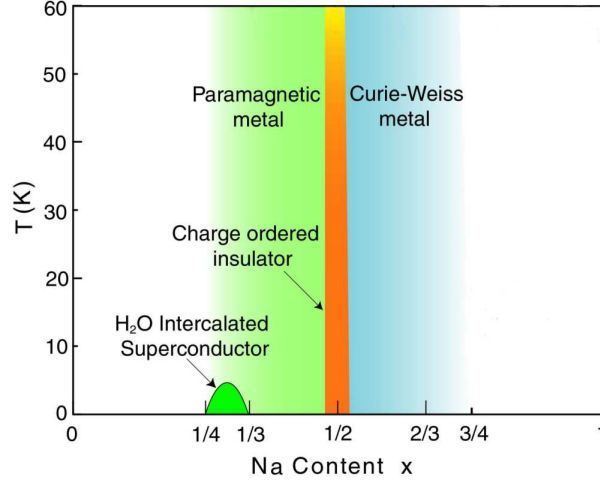


Figure 6.1: Na_xCoO_2 phase diagram (from Foo *et al.* [29])

vealed an equally-interesting insulating Na_xCoO_2 ($x \approx 0.5$) phase between the superconductive $\text{Na}_{0.33}\text{CoO}_2 \cdot 1.3\text{H}_2\text{O}$ and the high-thermoelectric, metallic $\text{Na}_{0.7}\text{CoO}_2$ phase. Subsequently, the Na_xCoO_2 ($x \approx 0.5$) phase has itself become the subject of detailed study [43, 73, 65, 31, 12]. In addition to Na_xCoO_2 ($x \approx 0.5$) being a relatively insulating composition, it is the only composition for P2 Na_xCoO_2 with $d\rho/dT < 0$. Furthermore, it experiences an abrupt transition to strongly insulating behavior at 53 K that remains of unclear origin (see Fig. 6.2).

Foo *et al.* [29] also reported a $(2a \times \sqrt{3}a)$ superstructure that was observed with electron diffraction. Neutron diffraction by Huang *et al.* [40] confirmed the $(2a \times \sqrt{3}a)$ superstructure in Na_xCoO_2 ($x \approx 0.5$) and further elaborated on the details of the structure; the hexagonal symmetry ($P6_3/mmc$) of the P2 structure is changed to orthorhombic ($Pnmm$) symmetry by the equal occupancy of Na1 and Na2 sites by Na ions that order so as to form one dimensional (1D) zig-zag chains (see Fig. 6.3). The Na ordering also creates two distinct types of Co ions that form linear 1D chains (see Fig. 6.3).

Figure 6.4 shows the two types of Co ions with their nearest Na neighbors.

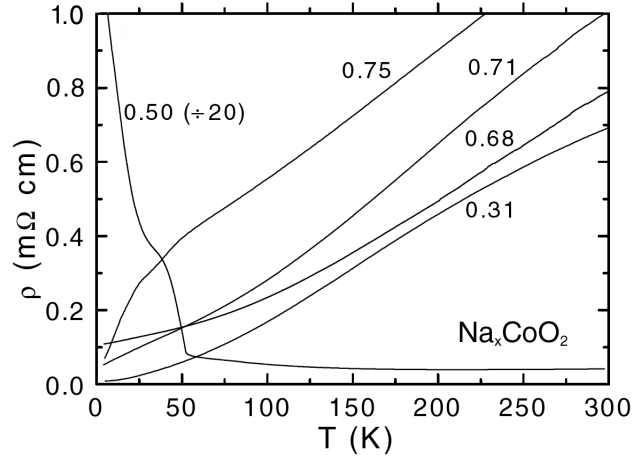


Figure 6.2: In-plane $\rho(T)$ measurements for Na_xCoO_2 floating-zone grown crystal samples with $0.31 < x < 0.75$ and including a Na_xCoO_2 ($x \approx 0.5$) sample (from Foo *et al.* [29]). Note the different scale for the Na_xCoO_2 ($x \approx 0.5$) sample.

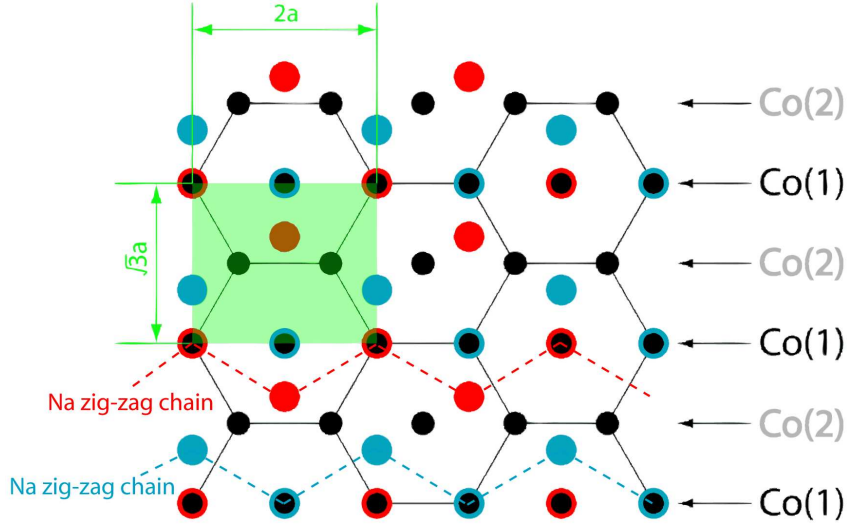


Figure 6.3: Schematic of $(2a \times \sqrt{3}a)$ orthorhombic superstructure for Na_xCoO_2 ($x \approx 0.5$) where black circles represent a plane of Co ions, red circles represent Na ions on one side of the Co plane (*e.g.* above), and blue circles represent Na ions on the opposite side of the Co plane (*e.g.* below). The schematic clearly shows the alternating rows of Co1 ions (with Na ions directly above or below) and Co2 ions (with no Na ions directly above or below).

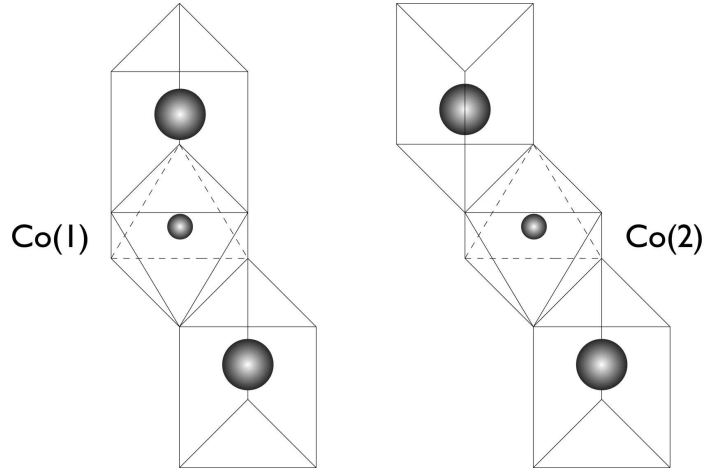


Figure 6.4: Schematic showing the Co1 and Co2 ions (octahedral sites) in Na_xCoO_2 ($x \approx 0.5$) with their nearest Na neighbors (trigonal prismatic sites). The Co1 ions have Na neighbors across an octahedral face (Na1 ion) and opposite octahedral edge (Na2 ion), and the Co2 ions have Na neighbors across opposite octahedral edges (Na2 ions).

Co1 ions “see” Na ions across an octahedral face and an opposite octahedral edge; on the other hand, Co2 ions do not “see” any Na ions across an octahedral face but instead have Na ions across opposite octahedral edges. Early electron and neutron diffraction investigations of the Na_xCoO_2 ($x \approx 0.5$) structure [29, 40, 112] proposed that its insulating character was due to a strong coupling between Na ions and holes in the $\text{Co}^{4+/3+}$ redox couple (t_{2g} holes) that resulted in a charge-ordered state in the Co lattice where the Co2 linear 1D chains consist of Co^{4+} ions and the Co1 linear 1D chains consist of Co^{3+} ions.

A charge-ordered state consisting of Co ions with higher formal charge located at the Co2 sites is based on a nearest neighbor electrostatic calculation where the charge of a Na ion across an octahedral face is screened less effectively than across an octahedral edge (see Fig. 6.4). However, recent neutron diffraction experiments [109] have thrown such a charge-ordered state into question after demonstrating very small differences between the $\langle \text{Co1-O} \rangle$ and $\langle \text{Co2-O} \rangle$ bond distances. Using

Table 6.1: Co–O distances (\AA) and Bond Valence Sums (BVS) as reported by Williams *et al.* [109] based on neutron diffraction structural results for Na_xCoO_2 ($x \approx 0.5$) sample at 10 K and 300 K.

Type	10 K	300 K	$\Delta(10\text{ K} - 300\text{ K})$
$\langle \text{Co1-O} \rangle$	1.887 \AA	1.891 \AA	$\Delta = -.004\text{ \AA}$
BVS (Co1)	3.43	3.40	$\Delta = -.03$
$\langle \text{Co2-O} \rangle$	1.900 \AA	1.898 \AA	$\Delta = +.002\text{ \AA}$
BVS (Co2)	3.31	3.33	$\Delta = +.02$

bond valence sum (BVS) calculations, such small differences in bond distances are not able to justify a conventionally charge-ordered state. In fact, the $\langle \text{Co1-O} \rangle$ bond distance was measured to be smaller than the $\langle \text{Co2-O} \rangle$ bond distance (see Table 6.1), which is opposite to what is expected for the proposed ordered state based on electrostatics.

Whereas the origin of the insulating behavior and the semiconductor–insulator transition (also erroneously referred to as a metal–insulator transition in the literature) that is observed at 53 K has been the focus of most of the research conducted on Na_xCoO_2 ($x \approx 0.5$), less effort has been made in trying to account for the thermoelectric power $S(T)$ which experiences an unusual crossover (change in sign) from $+S$ to $-S$ at $\approx 75\text{ K}$ upon cooling. Although the change in sign in $S(T)$ was reported early on in the investigation of the Na_xCoO_2 phase diagram (see Fig 6.5), little explanation has been offered to account for the crossover of $S(T)$ from $\approx +40\mu\text{V/K}$ to $\approx -500\mu\text{V/K}$ in the floating-zone-grown Na_xCoO_2 ($x \approx 0.5$) crystals that were studied.

It is tempting to interpret the crossover in $S(T)$ as arising from a change in the dominant type of carrier, *i.e.* from p-type (t_{2g} holes) to n-type (unknown character) upon cooling. However, no model exists to account for such a change in carrier type, or even to identify how the electronic structure could yield an n-type

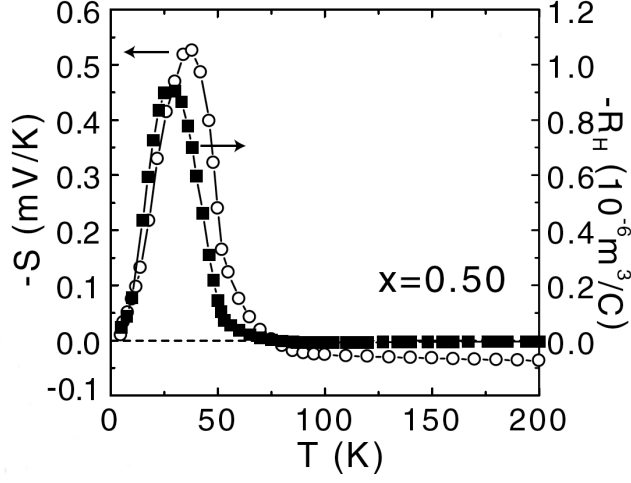


Figure 6.5: Thermopower $S(T)$ and Hall Coefficient $R_H(T)$ for Na_xCoO_2 ($x \approx 0.5$) (data from Foo *et al.* [29]). Note that $-S$ and $-R_H$ are plotted.

thermoelectric power at low T . Nevertheless, it is interesting to note that the Hall Coefficient $R_H(T)$ also suggests a change from p-type to n-type at ≈ 75 K upon cooling (see Fig. 6.5).

It is also interesting to review the magnetic behavior $\chi(T)$ that has been measured for Na_xCoO_2 ($x \approx 0.5$). Figure 6.6 shows both the magnetic ($\chi(T)$) and resistive ($\rho(T)$) characterization of the phase transitions reported by Huang *et al.* [40] for Na_xCoO_2 ($x \approx 0.5$) below 100 K. The magnetic transition, small peak in $\chi(T)$, occurring at 53 K occurs at the same temperature as the transition to strongly insulating behavior upon cooling. On the other hand, the more subtle magnetic transition at ≈ 87 K does not correspond to any strong transition in $\rho(T)$, although a small feature in $d\rho/dT$ is distinguishable at the same T .

The magnetic transition occurring at $\approx 87 - 88$ K has been further studied by Gasparovic *et al.* [30] with polarized and unpolarized neutron scattering measurements. Their data indicate that below 88 K new peaks arise that are distinct from the Na superlattice reflections and are instead due to magnetic ordering. Gas-

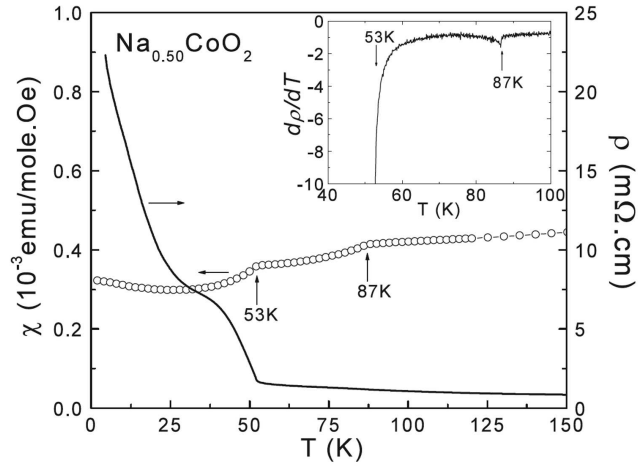


Figure 6.6: Magnetic susceptibility $\chi(T)$ measured for a Na_xCoO_2 ($x \approx 0.5$) polycrystalline powder sample and the electronic resistivity $\rho(T)$ measured along the plane of a Na_xCoO_2 ($x \approx 0.5$) single crystal (data from Huang *et al.* [40]) showing the magnetic and electronic transitions.

parovic *et al.* propose the magnetic order model shown in Fig. 6.7 where half of the Co ions are ordered antiferromagnetically along 1D Co chains that are separated by 1D chains of “nonordered” Co ions. However, from the neutron diffraction experiments one is not able to determine whether the magnetically ordered Co ions occupy Co1 or Co2 sites. Therefore, the question of whether the holes (magnetic Co^{4+}) occupy the Co2 sites, as an electrostatic analysis suggests, or the magnetically dead Co^{3+} occupy the Co2 sites, as the most recent Co–O bond distances measured by neutron diffraction suggest, remains unanswered. However, Gaparovic’s model of the spin arrangement does support the idea of charge-ordering in the Co array, at least below 88 K.

Another important aspect of the structure that is necessary to better understand the magnetic and electronic transitions that occur at 88 K and 53 K is the temperature dependence of the cell parameters. Figure 6.8 shows $a/\sqrt{3}$ and $b/2$ *vs.* T as measured with neutron diffraction by Williams *et al.* [109] for an $(a \times b)$ orthorhombic unit cell of a Na_xCoO_2 ($x \approx 0.5$) powder sample. The lattice parameters

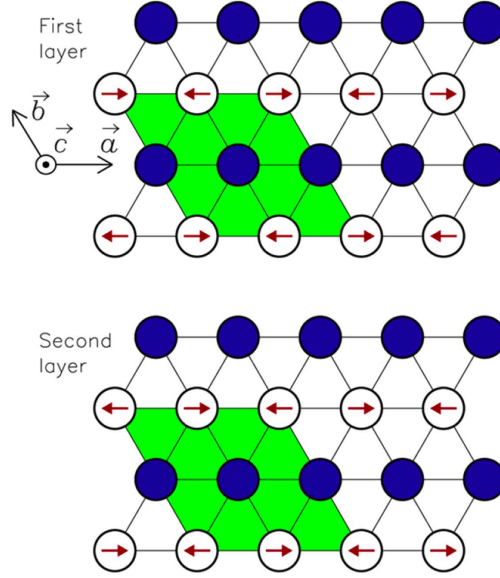


Figure 6.7: Gasparovic *et al.* [30] proposed model for the magnetic order below 88 K in Na_xCoO_2 ($x \approx 0.5$).

show a highly anisotropic thermal expansion with a large c-axis compression upon cooling. Whereas the solid lines in the figure were added by Williams *et al.* as guides to the eye, the dashed lines have been added here to highlight the abrupt change that occurs in dc/dT between the resistive and magnetic transition temperatures ($53 \text{ K} < T < 88 \text{ K}$), and which will be shown to be of importance in accounting for the behavior of Na_xCoO_2 ($x \approx 0.5$).

The surprising experimental result of a larger measured $\langle \text{Co2-O} \rangle$ than $\langle \text{Co1-O} \rangle$ bond distance has already been pointed out. It is also important to point out the temperature dependence of the Co-O bond distances; $\langle \text{Co1-O} \rangle$ decreases while $\langle \text{Co2-O} \rangle$ increases upon cooling from 300 K to 10 K (see Table 6.1). This opposite trend between the $\langle \text{Co1-O} \rangle$ and $\langle \text{Co2-O} \rangle$ bond distances supports the idea of increased charge ordering in the Co array upon cooling; however, as has already been pointed out, the BVS derived from the Co-O bond distances are not sufficiently different to support the idea of a conventional charge ordering.

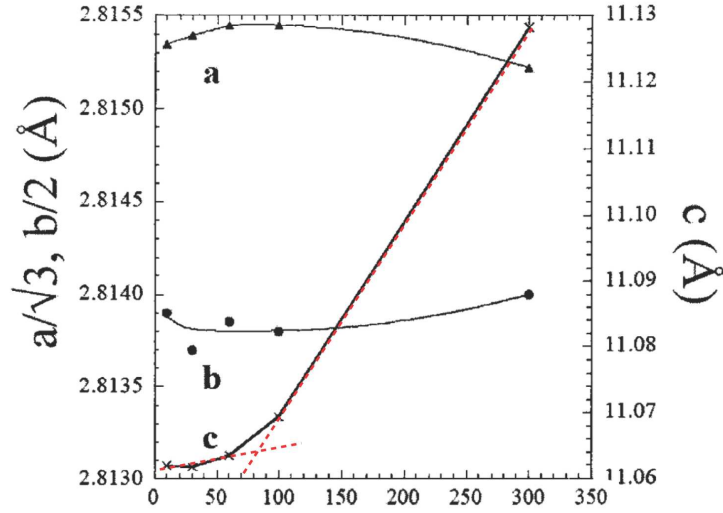


Figure 6.8: Lattice paramets vs. T for Na_xCoO_2 ($x \approx 0.5$) (data taken from Williams *et al.* [109])

Finally, after reviewing the structure and properties of Na_xCoO_2 ($x \approx 0.5$) samples that have been measured and reported in the literature, we are in a position to ask the following key questions necessary for developing a model for Na_xCoO_2 ($x \approx 0.5$):

1. What is the origin of the semiconductor-like resistivity ($d\rho/dT < 0$) already present at 300 K?
2. Why is the $\langle \text{Co1-O} \rangle$ bond distance less than the $\langle \text{Co2-O} \rangle$ bond distance if from an electrostatic calculation we expect the Co2 ions to have the higher formal charge?
3. Why does the c-axis show great compressibility upon cooling and the rate of the c-axis compression (dc/dT) change abruptly at low T ?
4. What is the significance of the opposite trends upon cooling between the $\langle \text{Co1-O} \rangle$ and the $\langle \text{Co2-O} \rangle$ bond distances?

5. Below 88 K, are the magnetically ordered Co ions (see Fig. 6.7) located at the Co2 or Co1 sites, *i.e.* are the holes primarily on the Co2 or the Co1 sites?
6. What is the nature of the crossover of $S(T)$ that occurs at ≈ 75 K?
7. What is the nature of the semiconductor to insulator transition that occurs upon cooling at 53 K?

This chapter presents a model that attempts to answer these key questions and account for the behavior of the physical properties that have been measured and reported in the literature. In addition, thermoelectric power $S(T)$ measurements made on polycrystalline Na_xCoO_2 powder samples will be presented and also used in developing a successful model for Na_xCoO_2 ($x \approx 0.5$).

6.2 Experimental

The majority of the experimental results used in constructing a model that accounts for the complex behavior of Na_xCoO_2 ($x \approx 0.5$) have been taken from the literature and have been presented in the introduction of this chapter. The resistivity $\rho(T)$ (Fig 6.2 and 6.6), thermoelectric power $S(T)$ (Fig. 6.5), Hall coefficient $R_H(T)$ (Fig. 6.5), and the polarized/unpolarized neutron scattering (Fig. 6.7) measurements (used for the proposed magnetic-order model) were all made on single crystals that were prepared by electrochemically deintercalating floating-zone grown Na_xCoO_2 crystals to yield $x \approx 0.5$ as described elsewhere [20, 19]. The reported measurements of $\rho(T)$, $S(T)$, and $R_H(T)$ are the in-plane values.

In addition to the experimental results available in the literature, polycrystalline Na_xCoO_2 ($x \approx 0.5$) samples were prepared by solid-state synthesis and electrochemical deintercalation with I_2 , and their chemical composition was determined with ICP-MS. In order to shed light on the nature of the crossover of $S(T)$ in

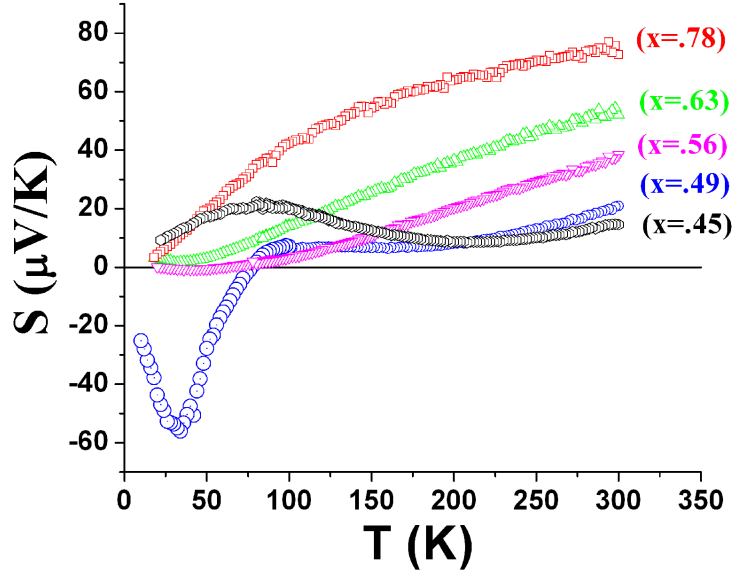


Figure 6.9: $S(T)$ for a series of Na_xCoO_2 samples with a range of x from $.45 < x < .78$ showing that for the Na_xCoO_2 sample ($x = 0.49$) there is a crossover from +S to -S at ≈ 75 K upon cooling.

Na_xCoO_2 ($x \approx 0.5$), thermoelectric power was measured in a homemade setup for these Na_xCoO_2 polycrystalline powder samples.

Figure 6.9 shows the evolution of thermoelectric power $S(T)$ with Na concentration for a series of Na_xCoO_2 samples with a range of x from 0.45 to 0.78 measured from ≈ 15 K to 300 K. The Na_xCoO_2 sample ($x = 0.49$) shows the same crossover of $S(T)$ from +S to -S at ≈ 75 K that was reported by Foo *et al.* [29]; however, unlike the floating-zone grown single crystal measured by Foo which reaches a minimum at $\approx -500 \mu\text{V/K}$, the polycrystalline Na_xCoO_2 ($x \approx 0.5$) sample measured in Fig. 6.9 reaches a minimum at $\approx -60 \mu\text{V/K}$. We attribute this difference in the magnitude of the $S(T)$ minimum to the different sample types (pressed polycrystalline powder sample *vs.* a floating-zone grown “single” crystal measured along the *ab*-plane); however, we note that the $S(T)$ behavior is qualitatively the same for the two sample types, with both exhibiting a crossover of $S(T)$ from +S to -S at ≈ 75 K and

reaching a minimum at ≈ 35 K.

As was pointed out in chapter 4, the thermopower decreases as Na is removed and becomes less temperature dependent for the lower Na content samples. However, as is typical for an $x \approx 0.5$ sample, $S(T)$ exhibits an abrupt crossover in sign at ≈ 75 K that is unique to this composition. For samples with x sufficiently less than 0.5, $S(T)$ does not exhibit a change in sign; however, it may exhibit a local maximum below 100 K, as is the case for the $x = 0.45$ sample in Fig. 6.9.

6.3 Discussion and Model

The characterization of the structure and physical properties that have been presented from the literature and our own experimental measurements are only a small fraction of what has been published, but they represent the most salient characteristics of the Na_xCoO_2 ($x \approx 0.5$) phase. However, what is most needed is a model that is able to account for all of the experimental results. A successful model must be able to answer the seven questions posed afore or at least point the way to the future experiments that are necessary to resolve them. In order to answer these questions, it is necessary to first take a closer look at the details of the Na-ordered Pnmm structure.

In Fig. 6.3, it was shown that the Na ordering in Na_xCoO_2 ($x \approx 0.5$) creates rows of Co1 and Co2 ions; then in Fig. 6.4, the environments surrounding the Co1 and Co2 ions were compared. From Fig. 6.3, it is also apparent that there are two types of Na ions that either occupy a Na1 or Na2 site. It is also useful to compare the environments surrounding the Na1 and Na2 ions (see Fig. 6.10). The information in Figs. 6.4 and 6.10 is already present in Fig. 6.3; however, Fig. 6.10 makes one immediately aware of the Co1–Na1–Co1 “triplets” that are present in the structure.

A schematic of a cross-section of the structure is shown in Fig. 6.11 to further illustrate the Co1–Na1–Co1 triplets. The triplets are of significance because the Na

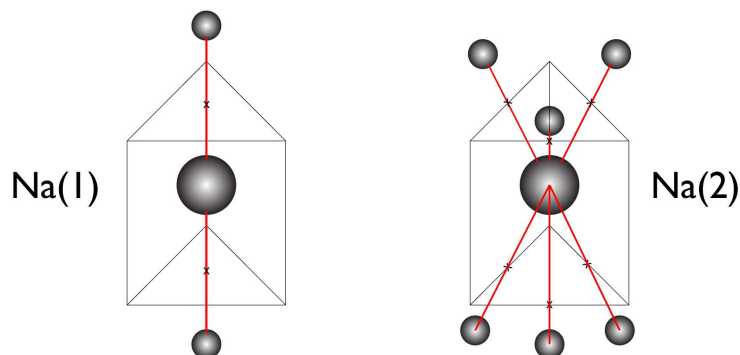


Figure 6.10: Schematic illustration showing the occupied Na1 and Na2 sites in Na_xCoO_2 ($x \approx 0.5$) with their nearest Co neighbors. The Na1 ions have two Co near neighbors (Co1 ions) across opposite faces of their trigonal prism while the Na2 ions have six Co near neighbors (four Co2 ions and two Co1 ions) across all six edges of their trigonal prism.

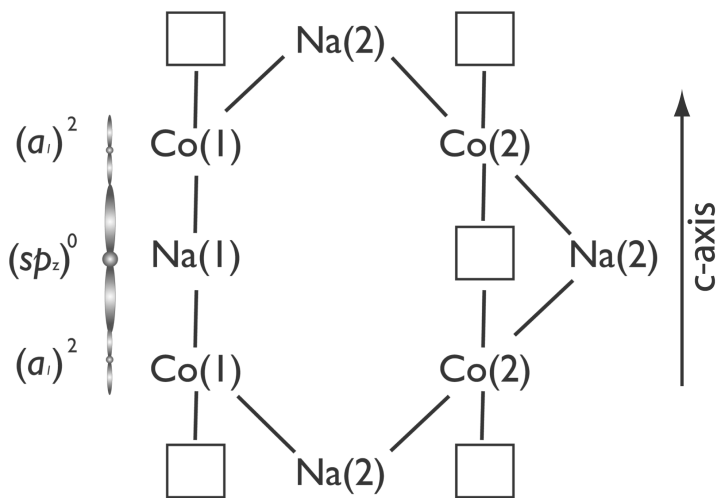


Figure 6.11: Schematic of a cross-section of Na_xCoO_2 ($x \approx 0.5$) structure showing Na-Co-Na triplets where vertical lines connect neighboring ions through octahedral/trigonal prismatic faces, diagonal lines connect ions through octahedral/trigonal prismatic edges, and squares represent vacant Na1 sites. The leftmost schematic shows the electron orbitals of the Na-Co-Na triplets that are directed along the c-axis.

ion sits in a Na1 site that shares faces with 2 neighboring Co octahedra. From an electrostatic calculation, we expect the Na ions to preferentially occupy Na2 sites, as they do for all Na compositions other than $x \approx 0.5$ [23, 58, 45]. Therefore, it is unusual for 1/2 of the Na ions to occupy Na1 sites in the Na_xCoO_2 ($x \approx 0.5$) phase. In fact, from Fig. 6.11 one sees that all of the Co1 ions (1/2 of all Co ions) are part of a Co1–Na1–Co1 triplet. Furthermore, Co1 ions in a triplet are each connected to Co2 ions via a Co1–Na2–Co2 “bridge” where the bridging Na2 ion sees the Co ions across octahedral edges. Similarly, Co1 ions in a triplet are connected to the Co1 ions in triplets directly above and below (not shown) by Co1–Na2–Co1 “bridges” where again the Na2 ion sees the Co1 ions across octahedral edges. Our model will show that the Co1–Na1–Co1 triplets play an important role that is necessary to consider for understanding the Na_xCoO_2 ($x \approx 0.5$) phase.

After a detailed inspection of the structure and careful review of the properties of Na_xCoO_2 ($x \approx 0.5$), one is now in a position to answer the seven questions that a successful model needs to address:

1. What is the origin of the semiconductor-like resistivity ($d\rho/dT < 0$) already present at 300 K?

At 300 K, Na is already ordered, giving rows of Co1 and Co2 ions and an enlarged ($2a \times \sqrt{3}a$) unit cell. Whereas the Na is fully ordered at 300 K, neutron diffraction experiments [109] measure only small differences between $\langle \text{Co1-O} \rangle$ and $\langle \text{Co2-O} \rangle$ bond distances ($\approx .007 \text{ \AA}$) and, therefore, suggest that the Co array is not substantially charge-ordered and that the Co t_{2g} holes remain mainly delocalized. Instead, the larger ($2a \times \sqrt{3}a$) unit cell apparently opens a gap near the Fermi surface that accounts for the semiconducting $d\rho/dT < 0$.

Figure 6.12 shows the $\text{Co}^{4+}/3+$ redox couple of primarily a_1 -orbital parentage that has been split by the Na-ordering. Although it has not yet been made clear whether the holes (Co^{4+}) prefer to be located at the Co2 sites (as

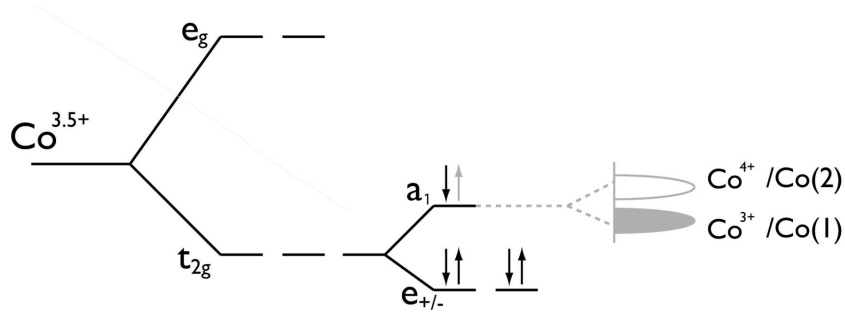


Figure 6.12: Schematic showing the splitting of the $\text{Co}^{4+}/^{3+}$ redox couple due to the Na-ordering.

electrostatics suggests) or at the Co1 sites (as neutron diffraction suggests), our model will argue for holes (Co^{4+}) preferentially at Co2 sites; therefore, Fig. 6.12 depicts a lower energy Co1 band and a higher energy Co2 band. The splitting of the a_1 band results in two narrower Co1 and Co2 bands that for $x \approx 0.5$ results in a band gap at (or near) the Fermi energy and therefore $d\rho/dT < 0$ (see Fig. 6.6).

2. Why is the $\langle \text{Co1-O} \rangle$ bond distance less than the $\langle \text{Co2-O} \rangle$ bond distance if from an electrostatic calculation we expect the Co2 ions to have the higher formal charge?

From an electrostatic calculation, we expect the higher charge Co^{4+} (holes) to preferentially occupy the Co2 sites that do not have a Na^+ neighbor across an octahedral face. Conversely, the lower charge Co^{3+} are expected to preferentially occupy the Co1 sites that do have a Na^+ neighbor across an octahedral face. This would normally result in a smaller $\langle \text{Co2-O} \rangle$ bond distance than a $\langle \text{Co1-O} \rangle$ bond distance because the Co^{4+} has 1 less electron to screen the Co nuclear charge from attracting the O^{2-} electronic charge. However, neutron diffraction measurements indicate the opposite; $\langle \text{Co1-O} \rangle$ is less than $\langle \text{Co2-O} \rangle$ (see Table 6.1).

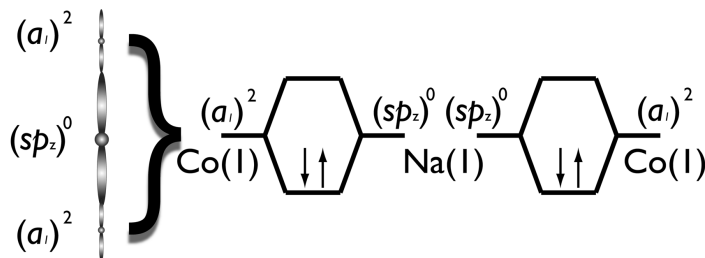


Figure 6.13: Schematic of structure showing Co–Na–Co triplet bonding orbitals.

Our model is supported by an electrostatic calculation and predicts that the Co2 ions have the higher formal charge. The fact that the $\langle \text{Co1-O} \rangle$ bond distance is less than the $\langle \text{Co2-O} \rangle$ bond distance is not surprising if the Co1–Na1–Co1 triplets are taken into consideration. If the holes are on the Co2 sites, then the Co1 ions are Co^{3+} with a $3d^6 = e_g^0 t_{2g}^6 = e_{+/-}^4 a_1^2$ electronic configuration. Because the Co1 a_1 orbitals are directed toward neighboring Na1 ions, it is reasonable to expect some bonding to occur in a triplet from full Co a_1^2 orbitals and an empty Na sp_z^0 hybridized orbital as is depicted in Fig 6.13. The formation of a Co1–Na1–Co1 triplet spreads out the Co1 a_1 -orbital wave function over a larger triplet “molecular orbital” wave function that effectively reduces the electronic screening between the Co1 ions and O^{2-} ions and result in a smaller $\langle \text{Co1-O} \rangle$ bond distance than $\langle \text{Co2-O} \rangle$ bond distance despite the fact that the Co2 ions have the higher formal valence, *i.e.* the Co2 ions have 1 hole each but the Co2 ions have 2 electrons each in delocalized triplet molecular orbitals.

3. Why does the c-axis show great compressibility upon cooling and the rate of

the c-axis compression (dc/dT) change abruptly at low T ?

Charge ordering increases upon cooling by localizing more electrons in Co1–Na1–Co1 triplet molecular orbitals. The localization of holes in the Co2 a_1 orbitals, which have no Na1 neighbors, has little effect on the c-axis lattice parameter; however, the electrons moved to the Co1–Na1–Co1 triplets, result in more c-axis bonding that dramatically reduces the c-axis lattice parameter upon cooling, thus resulting in a highly compressible c-axis. Co2–Na2–Co1 bridges may play an important role in the transfer of electrons from Co2 ions to the Co1–Na1–Co1 triplets.

The change in the c-axis compression rate (dc/dT) that occurs at low T signals a departure from the increased localization of electrons in Co1–Na1–Co1 triplets upon cooling. Looking at Fig. 6.8 (see dashed lines), one sees that the c-axis becomes much less compressible below $T \approx 85$ K (see intersection of dashed lines). This suggests that no more electrons are transferred to the triplets below $T \approx 85$ K and is consistent with a nearly fully charge-ordered Co array with all of the holes located at the Co2 sites. Therefore, as the structure is cooled from 300 K down to about 85 K, progressively more electrons become effectively trapped in Co1–Na1–Co1 triplet molecular orbitals. The electronic structure makes a transition from mainly delocalized Co: $a_1^{1.5}$ holes with a gap near the Fermi energy to localized Co⁴⁺ holes at Co2: a_1^1 orbitals* (see question 5 below).

4. What is the significance of the opposite trends upon cooling between the $\langle\text{Co1-O}\rangle$ and the $\langle\text{Co2-O}\rangle$ bond distances?

The opposite trends upon cooling, whereby the $\langle\text{Co2-O}\rangle$ bond distance increases and the $\langle\text{Co1-O}\rangle$ bond distance decreases, indicates that the holes in the Co a_1 bands have more O character than Co character. Therefore, the

*Note: Total number of a_1 holes is 0.5/Co.

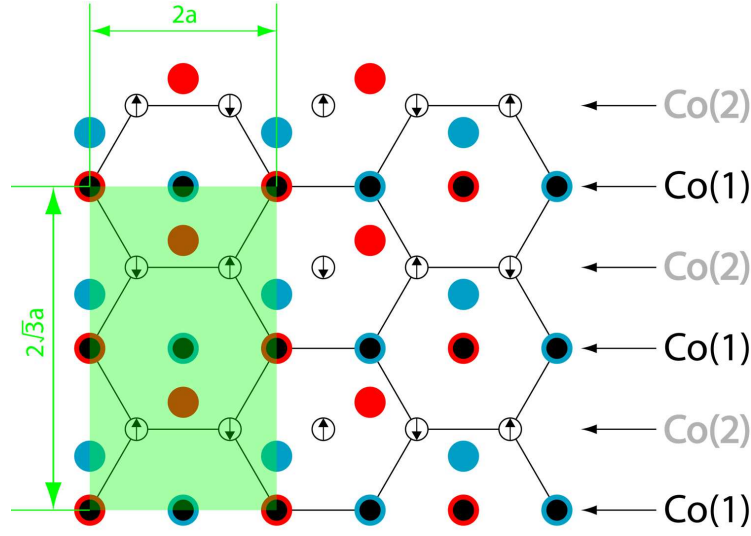


Figure 6.14: Schematic of Na order and the proposed magnetic order below 88 K proposed by Williams *et al.* [109] showing the resulting $(2a \times 2\sqrt{3}a)$ superstructure that is twice as large as the $(2a \times \sqrt{3}a)$ superstructure found above 88 K before the Co2 ions become magnetically ordered.

increased localization of holes at the Co2 ions is more accurately described as an electronic transfer of electrons from the O^{2-} surrounding Co2 ions to the Co1–Na1–Co1 molecular orbitals that likewise contain a large fraction of oxygen $2p$ character.

5. Below 88 K, are the magnetically ordered Co ions (see Fig. 6.7) located at the Co2 or Co1 sites, *i.e.* are the holes primarily on the Co2 or the Co1 sites?

As previously discussed, the lattice parameters as a function of T indicate that the holes become progressively more localized at the Co2 ions upon cooling from 300 K until at about 85 K the Co array becomes close to fully charge-ordered. The magnetic order model in Fig. 6.7 supports the increased charge-ordering upon cooling since the magnetically ordered Co must correspond to Co^{4+} ($S = 1/2$) since the Co^{3+} are low spin diamagnetic t_{2g}^6 ions ($S = 0$). Also, the measured $T_N = 88$ K coincides well with the change in compress-

ibility observed at nearly the same temperature (see Fig. 6.8). However, from Gasparovic's neutron scattering experiment [30], it is not clear whether the magnetically ordered Co ions are located at the Co2 or Co1 sites. But taking into consideration lattice parameters *vs.* T , $\langle \text{Co-O} \rangle$ bond distances, and the role of Na1–Co1–Na1 triplets, it is clear that the magnetically ordered Co ions are located at the Co2 sites as is illustrated in Fig. 6.14. Also, the magnetic order enlarges the magnetic unit cell size to $(2a \times 2\sqrt{3}a)$. An increase in cell size can have a pronounced effect on the electronic properties, as occurs with the Na-ordering that opens a gap near the Fermi surface even at 300 K. However, at 88 K the effect on the transport properties is not as pronounced; although we do note that $T_N = 88$ K does coincide with the steep downturn observed in $S(T)$ prior to the crossover that occurs upon cooling (see Fig. 6.9).

6. What is the nature of the crossover of $S(T)$ that occurs at ≈ 75 K?

In order to understand the $S(T)$ behavior, we must first determine the ground state of Na_xCoO_2 ($x \approx 0.5$). In Fig. 6.12, the splitting of the a_1 band into Co1 and Co2 bands was shown, but the specific ground state was not specified, *i.e.* whether the Fermi level was located in the Co1 band or the Co2 band.

Determining the ground state is not a straightforward task because of the uncertainties that exist in experimentally determining Na content, oxygen content, and Co oxidation state. However, the n-type S and R_H measured at $T < 75$ K (see Figs. 6.5 and 6.9), in addition to results from titration experiments [9, 10, 46, 47], indicate that, despite $x < 0.5$ in some Na_xCoO_2 ($x \approx 0.5$) samples, the Co oxidation state can be close to but always remains slightly less than 3.5+. A maximum in the Co oxidation state occurs due to the pinning of the $\text{Co}^{4+/3+}$ redox couple at the top of the $\text{O}^{2-}:2p^6$ band and results in either an oxygen deficient sample or the insertion of H_3O^+ ions [98, 67]. Therefore, for all Na_xCoO_2 ($x \approx 0.5$) samples with x sufficiently close to 0.5 so that the

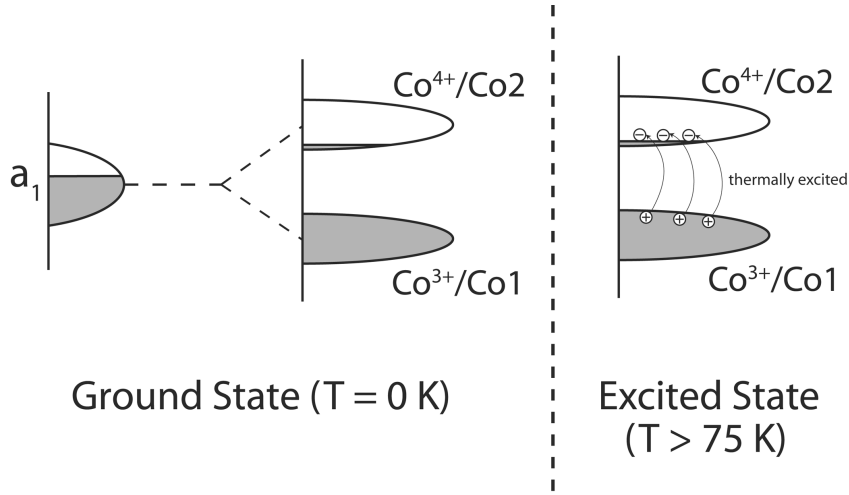


Figure 6.15: Schematic showing the ground state and excited state for Na_xCoO_2 ($x \approx 0.5$).

($2a \times \sqrt{3}a$) ordered superstructure is formed, the a_1 band is split into Co1 and Co2 bands and the Fermi energy is located in the Co2 band.

Figure 6.15 shows the suspected ground state and excited state for Na_xCoO_2 ($x \approx 0.5$) and helps explain the crossover of $S(T)$. At $T \approx 0$, there are no thermally excited carriers and the thermopower is dominated by the less than half-filled n-type Co2 band that gives a negative S . Although the n-type carriers in the Co2 band contribute to the thermopower at all T , at high T (> 75 K) the thermally excited carriers give a net positive S since their thermoelectric contribution dominates due to the Co1 band having much fewer carriers. The steep downturn in S that occurs at ≈ 88 K upon cooling indicates the start of the transition from a high- T Co1-band-dominated thermopower to a Co2-band-dominated thermopower.

7. What is the nature of the semiconductor to insulator transition that occurs upon cooling at 53 K?

As T decreases from 300 K, the Co array is increasingly charge-ordered until

at 88 K, there are enough holes on the Co2 sites to get antiferromagnetic interactions along the Co2 chains of nearly half-filled a_1^1 orbitals. At approximately the same temperature, the decreasing number of thermally excited carriers in the Co1 band causes a sharp downturn in $S(T)$ until at ≈ 75 K the thermoelectric power changes sign as it becomes dominated by the n-type carriers in the Co2 band. Finally at 53 K, there is a pronounced increase in ρ and in $|d\rho/dT|$ that marks the semiconductor to insulator transition. The abrupt change in $\rho(T)$ at 53 K coincides with a magnetic transition also observed at 53 K (see Fig. 6.6) that has not been studied as extensively as the transition at 88 K. Given the increase in the $\langle \text{Co2-O} \rangle$ bond length with decreasing temperature, it is reasonable to suspect a transition from itinerant to polaronic behavior of the conduction electrons in the Co2 band on cooling below 53 K.

6.4 Conclusions

In conclusion, a model that explains many of the salient characteristics of the Na_xCoO_2 ($x \approx 0.5$) phase has been presented. A detailed understanding of structure, *e.g.* the identification of Co1–Na1–Co1 triplets, has been shown to provide important clues for understanding the physical properties of Na_xCoO_2 ($x \approx 0.5$), such as the change in sign in $S(T)$ that occurs at $T \approx 75$ K. The presence of triplet molecular orbitals, in addition to a $\text{Co}^{4+/3+}$ redox couple that is pinned at the top of the $\text{O}^{2-}:2p^6$ band, leads to charge-ordering that does not exhibit large differences in Co–O bond distances and unexpected trends in Co–O bond distances as a function of temperature.

Chapter 7

Observations and Recommendations

7.1 CNT synthesis with lithographic techniques

This dissertation has shown that CNTs can be synthesized from amorphous carbon thin films by electron irradiation in the TEM. It was shown that irradiation effects impart a tensile stress and introduce defects to a CNT thus formed; the CNT can be made to fracture by a brittle or ductile mechanism. A healing of the carbon film was also observed to occur after some critical amount of irradiation.

These results indicate that CNTs, as well as other carbon nanostructures, can be synthesized and tailored by electron irradiation (or other ionizing radiation), and suggests the possibility of larger scale, carbon nanostructure design by e-beam lithography and complementary techniques. Such a technology has the potential of large scale CNT synthesis by patterning amorphous carbon in 1D channels and then using ionizing radiation (e-beam or ion-beam) to graphitize the amorphous carbon and form interconnected networks of CNTs or graphene ribbons.

7.2 Magnetic carbon: curvature and electron transfer

Magnetic carbon materials will continue to attract researchers' attention due to their remarkable physical properties and their potential to develop into a variety of useful technological devices. For this reason, a systematic study of the effect of curvature of graphene sheets and electron donation to the α bands of graphene should be considered. Since curvature is inversely proportional to particle size for a system of carbon-encapsulated metal nanoparticles as was presented in Chapter 3, such a study could be carried out by producing several different size classes of graphene-coated metal nanoparticles, each with tightly controlled size distributions. Furthermore, the effect of electron donation can also be probed by producing nanoparticles of different elemental composition that have different workfunctions. Most interesting would be to choose a material with a larger workfunction than the graphitic encapsulating carbon and see the effect of creating holes in the α band.

7.3 STM of Na_xCoO_2 and charge-ordering

A model was presented in chapter 6 that supported a charge-ordered configuration in the Co array of Na_xCoO_2 ($x \approx 0.5$) where the higher formal charge Co ions are located on rows of Co2 ions. However, direct experimental evidence of such a charge ordering is still sought, especially considering the neutron diffraction measurements of shorter Co1–O bond distances than Co2–O bond distance. STM experiments that can directly observe charge-ordering in the Co array and determine whether the holes reside on Co2 or Co1 ions would be of tremendous benefit to further the understanding of Na_xCoO_2 ($x \approx 0.5$) and the related superconductor $\text{Na}_{0.33}\text{CoO}_2 \cdot 1.3\text{H}_2\text{O}$.

7.4 Na_xCoO_2 as a potential cathode material in a mixed Li-ion Na-ion battery

Li_xCoO_2 can be considered the first cathode material to be used in widely commercialized Li-ion rechargeable batteries and it still remains the most common cathode material today. However, there is room for improvement in both its cost and performance by considering other cathode materials such as LiMn_2O_4 or LiFePO_4 among others. The identification and development of such new materials for an improved electrochemical device comes from a detailed understanding of the structure, properties, and underlying physics of oxide materials in general. The idea to use Na_xCoO_2 as a cathode material in a mixed Li-ion Na-ion battery is motivated by this same spirit of using a fundamental understanding of the properties of oxides in order to intelligently design an improved technological device.

A major drawback of using Li_xCoO_2 as a cathode material in a rechargeable Li or Li-ion battery is the inherent instability in the cathode that is caused by the pinning of the $\text{Co}^{4+/3+}$ redox couple at the top of the $\text{O}^{2-}:\text{2p}^6$ band. This instability essentially limits the capacity of the battery, since only half of the $\text{Co}^{4+/3+}$ redox couple can be reversibly utilized. Deintercalation beyond $x < 0.5$ results in either the creation of oxygen vacancies [107] or the insertion of protons [17]. It follows that an analogous compound to Li_xCoO_2 , but with an active redox couple raised relative to the $\text{O}^{2-}:\text{2p}^6$ band, could relieve the instability caused by the pinning in Li_xCoO_2 and allow for more than 50% of the active redox couple to be utilized, thus increasing the capacity of the battery by up to 50%.

In a mixed Na-ion and Li-ion battery that consists of a Na_xCoO_2 cathode and Li-ion electrolyte, cycling of the battery may preferentially extract and intercalate Li^+ ions from and into the Na_xCoO_2 structure without removing an appreciable amount of the Na^+ ions from the cathode, thereby maintaining the P2 structure

during cycling.* Unlike the Li_xCoO_2 cathode presently used in rechargeable batteries, which has the O3 structure and involves diffusion of Li ions in octahedral sites through smaller tetrahedral sites, the P2 structure can provide faster diffusion of the Li ions through much larger trigonal prismatic sites that do not involve diffusion through high energy tetrahedral sites. Such a P2 cathode could be useful for high-power applications. In addition, the inclusion of a more electropositive counter-cation may raise the $\text{Co}^{4+/3+}$ redox couple relative to the $\text{O}^{2-}:2p^6$ band and allow more of the Co redox couple to be utilized in a reversible charge/discharge cycle by avoiding the problems caused by the pinning of the $\text{Co}^{4+/3+}$ redox couple at the top of the $\text{O}^{2-}:2p^6$ band. More fundamentally, such electrochemical experiments provide a practical method of studying how different counter-cations affect the position of the $\text{Co}^{4+/3+}$ redox couple relative to the $\text{O}^{2-}:2p^6$ band and how such knowledge might lead to the development of better cathode materials for rechargeable batteries.

*This could be tested by checking that the structure of the Na_xCoO_2 cathode remains P2 after cycling as well as by performing chemical analysis of the cathode and electrolyte after cycling.

Bibliography

- [1] P. M. Ajayan, V. Ravikumar, and J. C. Charlier. Surface reconstructions and dimensional changes in single-walled carbon nanotubes. *Physical Review Letters*, 81(7):1437–1440, 1998.
- [2] P. M. Allemand, K. C. Khemani, A. Koch, F. Wudl, K. Holczer, S. Donovan, G. Gruner, and J. D. Thompson. Organic molecular soft ferromagnetism in a fullerene-c60. *Science*, 253(5017):301–303, 1991.
- [3] A. N. Andriotis, M. Menon, R. M. Sheetz, and L. Chernozatonskii. Magnetic properties of c-60 polymers. *Physical Review Letters*, 90(2):026801, 2003.
- [4] V. E. Antonov, I. O. Bashkin, S. S. Khasanov, A. P. Moravsky, Y. G. Morozov, Y. M. Shulga, Y. A. Ossipyan, and E. G. Ponyatovsky. Magnetic ordering in hydrofullerite c60h24. *Journal of Alloys and Compounds*, 330:365–368, 2002.
- [5] S. Bandow, F. Kokai, K. Takahashi, M. Yudasaka, and S. Iijima. Unique magnetism observed in single-wall carbon nanohorns. *Applied Physics a-Materials Science & Processing*, 73(3):281–285, 2001.
- [6] S. Bandow, T. Yamaguchi, and S. Iijima. Magnetism of adsorbed oxygen on carbon nanohorns. *Chemical Physics Letters*, 401(4-6):380–384, 2005.
- [7] F. Banhart. Irradiation effects in carbon nanostructures. *Reports on Progress in Physics*, 62(8):1181–1221, 1999.

- [8] F. Banhart, T. Fuller, P. Redlich, and P. M. Ajayan. The formation, annealing and self-compression of carbon onions under electron irradiation. *Chemical Physics Letters*, 269(3-4):349–355, 1997.
- [9] M. Banobre-Lopez, F. Rivadulla, R. Caudillo, M. A. Lopez-Quintela, J. Rivas, and J. B. Goodenough. Role of doping and dimensionality in the superconductivity of NaCoO_2 . *Chemistry of Materials*, 17(8):1965–1968, 2005.
- [10] P. W. Barnes, M. Avdeev, J. D. Jorgensen, D. G. Hinks, H. Claus, and S. Short. Superconductivity and cobalt oxidation state in metastable $\text{NaCoO}_{2-\delta}$ (x approximate to 1/3; y approximate to 4x). *Physical Review B*, 72(13):134515, 2005.
- [11] S. P. Bayrakci, C. Bernhard, D. P. Chen, B. Keimer, R. K. Kremer, P. Lemmens, C. T. Lin, C. Niedermayer, and J. Strempfer. Bulk antiferromagnetism in $\text{Na}_{0.82}\text{CoO}_2$ single crystals. *Physical Review B*, 69(10):100410(R), 2004.
- [12] J. Bobroff, G. Lang, H. Alloul, N. Blanchard, and G. Collin. Nmr study of the magnetic and metal-insulator transitions in $\text{Na}_{0.5}\text{CoO}_2$: A nesting scenario. *Physical Review Letters*, 96(10):107201, 2006.
- [13] D. W. Boukhvalov, P. F. Karimov, E. Z. Kurmaev, T. Hamilton, A. Moewes, L. D. Finkelstein, M. I. Katsnelson, V. A. Davydov, A. V. Rakhmanina, T. L. Makarova, Y. Kopelevich, S. Chiuzbaian, and M. Neumann. Testing the magnetism of polymerized fullerene. *Physical Review B*, 69(11):115425, 2004.
- [14] R. Caudillo, X. Gao, R. Escudero, M. Jose-Yacaman, and J. B. Goodenough. Ferromagnetic behavior of carbon nanospheres encapsulating silver nanoparticles. *Physical Review B*, 74:214418, 2006.
- [15] R. Caudillo, H. E. Troiani, M. Miki-Yoshida, M. A. L. Marques, A. Rubio, and M. J. Yacaman. A viable way to tailor carbon nanomaterials by irradiation-

- induced transformations. *Radiation Physics and Chemistry*, 73(6):334–339, 2005.
- [16] D. P. Chen, H. C. Chen, A. Maljuk, A. Kulakov, H. Zhang, P. Lemmens, and C. T. Lin. Single-crystal growth and investigation of $\text{Na}_{1-x}\text{CoO}_2$ and $\text{Na}_{1-x}\text{CoO}_2 \cdot y\text{H}_2\text{O}$. *Physical Review B*, 70(2):024506, 2004.
- [17] J. Choi, E. Alvarez, T. A. Arunkumar, and A. Manthiram. Proton insertion into oxide cathodes during chemical delithiation. *Electrochemical and Solid State Letters*, 9(5):A241–A244, 2006.
- [18] J. Choi and A. Manthiram. Comparison of the chemical and structural instabilities of $\text{Na}_{0.75}\text{CoO}_2$ and Li_xCoO_2 . *Physical Review B*, 74(20):205114, 2006.
- [19] F. C. Chou, E. T. Abel, J. H. Cho, and Y. S. Lee. Electrochemical deintercalation, oxygen non-stoichiometry, and crystal growth of $\text{Na}_{1-x}\text{CoO}_2$. *Journal of Physics and Chemistry of Solids*, 66(1):155–160, 2005.
- [20] F. C. Chou, J. H. Cho, and Y. S. Lee. Magnetic susceptibility study of hydrated and nonhydrated $\text{Na}_{1-x}\text{CoO}_2 \cdot y\text{H}_2\text{O}$ single crystals. *Physical Review B*, 70(14):144526, 2004.
- [21] B. L. Cushing and J. B. Wiley. Topotactic routes to layered calcium cobalt oxides. *Journal of Solid State Chemistry*, 141(2):385–391, 1998.
- [22] G. C. DeFotis. Magnetism of solid oxygen. *Physical Review B*, 23:4714, 1981.
- [23] C. Delmas, J. J. Braconnier, C. Fouassier, and P. Hagenmuller. Electrochemical intercalation of sodium in $\text{Na}_{1-x}\text{CoO}_2$ bronzes. *Solid State Ionics*, 3-4(AUG):165–169, 1981.

- [24] C. deVaulx, M. H. Julien, C. Berthier, M. Horvatic, P. Bordet, V. Simonet, D. P. Chen, and C. T. Lin. Nonmagnetic insulator state in NaCoO_2 and phase separation of Na vacancies. *Physical Review Letters*, 95(18):186405, 2005.
- [25] J. L. Elechiguerra, J. L. Burt, J. R. Morones, A. Camacho-Bragado, X. Gao, H. H. Lara, and M. J. Yacaman. *Journal of Nanobiotechnology*, 3(6), 2005. online journal.
- [26] T. Enoki, N. Kawatsu, Y. Shibayama, H. Sato, R. Kobori, S. Maruyama, and K. Kaneko. Magnetism of nano-graphite and its assembly. *Polyhedron*, 20(11-14):1311–1315, 2001.
- [27] P. Esquinazi, R. Hohné, K. H. Han, A. Setzer, D. Spemann, and T. Butz. Magnetic carbon: Explicit evidence of ferromagnetism induced by proton irradiation. *Carbon*, 42(7):1213–1218, 2004.
- [28] P. Esquinazi, A. Setzer, R. Hohné, C. Semmelhack, Y. Kopelevich, D. Spemann, T. Butz, B. Kohlstrunk, and M. Losche. Ferromagnetism in oriented graphite samples. *Physical Review B*, 66(2):024429, 2002.
- [29] M. L. Foo, Y. Y. Wang, S. Watauchi, H. W. Zandbergen, T. He, R. J. Cava, and N. P. Ong. Charge ordering, commensurability, and metallicity in the phase diagram of the layered NaCoO_2 . *Physical Review Letters*, 92(24):247001, 2004.
- [30] G. Gasparovic, R. A. Ott, J. H. Cho, F. C. Chou, Y. Chu, J. W. Lynn, and Y. S. Lee. Neutron scattering study of novel magnetic order in $\text{Na}_{0.5}\text{CoO}_2$. *Physical Review Letters*, 96(4):046403, 2006.
- [31] J. L. Gavilano, D. Rau, B. Pedrini, J. Hinderer, H. R. Ott, S. M. Kazakov, and J. Karpinski. Unconventional charge ordering in $\text{Na}_{0.7}\text{CoO}_2$ below 300 K. *Physical Review B*, 69(10):100404, 2004.

- [32] A. K. Geim and K. S. Novoselov. The rise of graphene. *Nature Materials*, 6(3):183–191, 2007.
- [33] J. Giles. Scientists create fifth form of carbon. *Nature*, pages 040322–5, 2004.
- [34] J. B. Goodenough. *Physical Review B*, 100:564, 1955.
- [35] K. H. Han, D. Spemann, P. Esquinazi, R. Hohne, V. Riede, and T. Butz. Ferromagnetic spots in graphite produced by proton irradiation. *Advanced Materials*, 15(20):1719–+, 2003.
- [36] K. H. Han, D. Spemann, P. Esquinazi, R. Hohne, V. Riede, and T. Butz. Magnetic signals of proton irradiated spots created on highly oriented pyrolytic graphite surface. *Journal of Magnetism and Magnetic Materials*, 272-76:1190–1191, 2004. Part 2 Sp. Iss. SI.
- [37] K. H. Han, D. Spemann, R. Hohne, A. Setzer, T. Makarova, P. Esquinazi, and T. Butz. Observation of intrinsic magnetic domains in c-60 polymer. *Carbon*, 41(4):785–795, 2003.
- [38] K. Harigaya and T. Enoki. Theory on the mechanisms of novel magnetism in stacked nanographite. *Molecular Crystals and Liquid Crystals*, 386:205–209, 2002.
- [39] R. Hohne and P. Esquinazi. Can carbon be ferromagnetic? *Advanced Materials*, 14(10):753–756, 2002.
- [40] Q. Huang, M. L. Foo, J. W. Lynn, H. W. Zandbergen, G. Lawes, Y. Y. Wang, B. H. Toby, A. P. Ramirez, N. P. Ong, and R. J. Cava. Low temperature phase transitions and crystal structure of $\text{Na}_0.5\text{CoO}_2$. *Journal of Physics-Condensed Matter*, 16(32):5803–5814, 2004.

- [41] Q. Huang, M. L. Foo, R. A. Pascal, J. W. Lynn, B. H. Toby, T. He, H. W. Zandbergen, and R. J. Cava. Coupling between electronic and structural degrees of freedom in the triangular lattice conductor Na_xCoO_2 . *Physical Review B*, 70(18):184110, 2004.
- [42] Q. Huang, B. Khaykovich, F. C. Chou, J. H. Cho, J. W. Lynn, and Y. S. Lee. Structural transition in Na_xCoO_2 with x near 0.75 due to Na rearrangement. *Physical Review B*, 70(13):134115, 2004.
- [43] J. Hwang, J. Yang, T. Timusk, and F. C. Chou. Infrared conductivity of Na_xCoO_2 : Evidence of gapped states. *Physical Review B*, 72(2):024549, 2005.
- [44] S. Iijima. Helical microtubules of graphitic carbon. *Nature*, 354(6348):56–58, 1991.
- [45] J. D. Jorgensen, M. Avdeev, D. G. Hinks, J. C. Burley, and S. Short. Crystal structure of the sodium cobaltate deuterate superconductor $\text{Na}_x\text{CoO}_2 \cdot 4x\text{D}_2\text{O}$ (x approximate to $1/3$). *Physical Review B*, 68(21):214517, 2003.
- [46] M. Karppinen, I. Asako, T. Motohashi, and H. Yamauchi. Oxygen non-stoichiometry and actual Co valence in Na_xCoO_2 -delta. *Physical Review B*, 71(9):092105, 2005.
- [47] M. Karppinen, S. Asako, T. Motohashi, and H. Yamauchi. Oxidation state of cobalt in the Na_xCoO_2 -delta center dot gamma H_2O superconductor. *Chemistry of Materials*, 16(9):1693–1696, 2004.
- [48] M. Karppinen, H. Fjellvag, T. Konno, Y. Morita, T. Motohashi, and H. Yamauchi. Evidence for oxygen vacancies in misfit-layered calcium cobalt oxide, $\text{Ca}_x\text{Co}_2\text{O}_{3+q}$. *Chemistry of Materials*, 16(14):2790–2793, 2004.

- [49] Y. Kopelevich, R. R. daSilva, J. H. S. Torres, and A. Penicaud. Local ferromagnetism in microporous carbon with the structural regularity of zeolite y. *Physical Review B*, 68:092408, 2003.
- [50] A. V. Krasheninnikov and K. Nordlund. Stability of irradiation-induced point defects on walls of carbon nanotubes. *J. Vac. Sci. Technol. B*, 20:728–733, 2002.
- [51] A. V. Krasheninnikov and K. Nordlund. Irradiation effects in carbon nanotubes. *Nuclear Instruments and Methods in Physics Research Section B-Beam Interactions with Materials and Atoms*, 216:355–366, 2004.
- [52] A. V. Krasheninnikov, K. Nordlund, and J. Keinonen. Production of defects in supported carbon nanotubes under ion irradiation. *Physical Review B*, 65(16):165423, 2002.
- [53] A. V. Krasheninnikov, K. Nordlund, M. Sirvio, E. Salonen, and J. Keinonen. Formation of ion-irradiation-induced atomic-scale defects on walls of carbon nanotubes. *Physical Review B*, 63(24):245405, 2001.
- [54] H. W. Kroto, J. R. Heath, S. C. Obrien, R. F. Curl, and R. E. Smalley. C-60 - buckminsterfullerene. *Nature*, 318(6042):162–163, 1985.
- [55] K. Kusakabe and M. Maruyama. Magnetic nanographite. *Physical Review B*, 67(9):092406, 2003.
- [56] K. Kusakabe and Y. Takagi. On possible surface magnetism in nanographite. *Molecular Crystals and Liquid Crystals*, 387:231–235, 2002.
- [57] P. O. Lehtinen, A. S. Foster, Y. C. Ma, A. V. Krasheninnikov, and R. M. Nieminen. Irradiation-induced magnetism in graphite: A density functional study. *Physical Review Letters*, 93(18):187202, 2004.

- [58] J. W. Lynn, Q. Huang, C. M. Brown, V. L. Miller, M. L. Foo, R. E. Schaak, C. Y. Jones, E. A. Mackey, and R. J. Cava. Structure and dynamics of superconducting NaCoO_2 hydrate and its unhydrated analog. *Physical Review B*, 68(21):214516, 2003.
- [59] T. L. Makarova, K. H. Han, P. Esquinazi, R. R. da Silva, Y. Kopelevich, I. B. Zakharova, and B. Sundqvist. Magnetism in photopolymerized fullerenes. *Carbon*, 41(8):1575–1584, 2003.
- [60] T. L. Makarova, B. Sundqvist, R. Hohné, P. Esquinazi, Y. Kopelevich, P. Scharff, V. Davydov, L. S. Kashevarova, and A. V. Rakhmanina. Magnetic carbon, retraction. *Nature*, 440:707, 2006.
- [61] T. L. Makarova, B. Sundqvist, R. Hohné, P. Esquinazi, Y. Kopelevich, P. Scharff, V. A. Davydov, L. S. Kashevarova, and A. V. Rakhmanina. Magnetic carbon. *Nature*, 413(6857):716–718, 2001.
- [62] C. A. Marianetti, G. Kotliar, and G. Ceder. Role of hybridization in NaCoO_2 and the effect of hydration. *Physical Review Letters*, 92(19):196405, 2004.
- [63] M. A. L. Marques, H. E. Troiani, M. Miki-Yoshida, M. Jose-Yacaman, and A. Rubio. On the breaking of carbon nanotubes under tension. *Nano Letters*, 4(5):811–815, 2004.
- [64] M. Maruyama, K. Kusakabe, S. Tsuneyuki, K. Akagi, Y. Yoshimoto, and J. Yamauchi. Magnetic properties of nanographite with modified zigzag edges. *Journal of Physics and Chemistry of Solids*, 65(2-3):119–122, 2004.
- [65] P. Mendels, D. Bono, J. Bobroff, G. Collin, D. Colson, N. Blanchard, H. Al-loul, I. Mukhamedshin, F. Bert, A. Amato, and A. D. Hillier. Cascade of bulk magnetic phase transitions in NaCoO_2 as studied by muon spin rotation. *Physical Review Letters*, 94(13):136403, 2005.

- [66] J. S. Miller. The quest for magnetic polymers - caveat-emptor. *Advanced Materials*, 4(6):435–438, 1992.
- [67] C. J. Milne, D. N. Argyriou, A. Chemseddine, N. Aliouane, J. Veira, S. Lands-
gesell, and D. Alber. Revised superconducting phase diagram of hole-doped
na-x(h3o)(z)coo2 center dot yh(2)o. *Physical Review Letters*, 93(24):247007,
2004.
- [68] A. W. Mombru, H. Pardo, R. Faccio, O. F. de Lima, E. R. Leite, G. Zanelatto,
A. J. C. Lanfredi, C. A. Cardoso, and F. M. Araujo-Moreira. Multilevel
ferromagnetic behavior of room-temperature bulk magnetic graphite. *Physical
Review B*, 71(10):100404, 2005.
- [69] Y. Morita, J. Poulsen, K. Sakai, T. Motohashi, T. Fujii, I. Terasaki, H. Ya-
mauchi, and M. Karppinen. Oxygen nonstoichiometry and cobalt valence in
misfit-layered cobalt oxides. *Journal of Solid State Chemistry*, 177(9):3149–
3155, 2004.
- [70] G. D. Morris, J. H. Brewer, S. R. Dunsiger, and M. Montour. Antiferromag-
netism in solid oxygen. *Hyperfine Interactions*, 104:381, 1997.
- [71] T. Motohashi, R. Ueda, E. Naujalis, T. Tojo, I. Terasaki, T. Atake, M. Karp-
pinen, and H. Yamauchi. Unconventional magnetic transition and transport
behavior in na0.75coo2. *Physical Review B*, 67(6):064406, 2003.
- [72] A. Mrzel, A. Omerzu, P. Umek, D. Mihailovic, Z. Jaglicic, and Z. Trontelj.
Ferromagnetism in a cobaltocene-doped fullerene derivative below 19 k due to
unpaired spins only on fullerene molecules. *Chemical Physics Letters*, 298(4-
6):329–334, 1998.
- [73] I. R. Mukhamedshin, H. Alloul, G. Collin, and N. Blanchard. Co-59 nmr

- study of the co states in superconducting and anhydrous cobaltates. *Physical Review Letters*, 94(24):247602, 2005.
- [74] Y. Murakami and H. Suematsu. Magnetism of c-60 induced by photo-assisted oxidation. *Pure and Applied Chemistry*, 68(7):1463–1467, 1996.
- [75] K. Murata, H. Ushijima, H. Ueda, and K. Kawaguchi. Magnetic-properties of amorphous-like carbons prepared from tetraaza compounds by the chemical vapor-deposition (cvd) method. *Journal of the Chemical Society-Chemical Communications*, (18):1265–1266, 1991.
- [76] K. Murata, H. Ushijima, H. Ueda, and K. Kawaguchi. A stable carbon-based organic magnet. *Journal of the Chemical Society-Chemical Communications*, (7):567–569, 1992.
- [77] B. Narymbetov, A. Omerzu, V. V. Kabanov, M. Tokumoto, H. Kobayashi, and D. Mihailovic. Origin of ferromagnetic exchange interactions in a fullerene-organic compound. *Nature*, 407(6806):883–885, 2000.
- [78] K. Niwase. Irradiation-induced amorphization of graphite. *Physical Review B*, 52(22):15785–15798, 1995.
- [79] K. S. Novoselov, A. K. Geim, S. V. Morozov, D. Jiang, M. I. Katsnelson, I. V. Grigorieva, S. V. Dubonos, and A. A. Firsov. Two-dimensional gas of massless dirac fermions in graphene. *Nature*, 438(7065):197–200, 2005.
- [80] K. S. Novoselov, A. K. Geim, S. V. Morozov, D. Jiang, Y. Zhang, S. V. Dubonos, I. V. Grigorieva, and A. A. Firsov. Electric field effect in atomically thin carbon films. *Science*, 306(5696):666–669, 2004.
- [81] K. S. Novoselov, Z. Jiang, Y. Zhang, S. V. Morozov, H. L. Stormer, U. Zeitler, J. C. Maan, G. S. Boebinger, P. Kim, and A. K. Geim. Room-temperature quantum hall effect in graphene. *Science*, 315(5817):1379–1379, 2007.

- [82] A. A. Ovchinnikov and V. N. Spector. Organic ferromagnets - new results. *Synthetic Metals*, 27(3-4):B615–B624, 1988.
- [83] N. Park, M. Yoon, S. Berber, J. Ihm, E. Osawa, and D. Tomanek. Magnetism in all-carbon nanostructures with negative gaussian curvature. *Physical Review Letters*, 91(23):237204, 2003.
- [84] L. R. Radovic and B. Bockrath. On the chemical nature of graphene edges: Origin of stability and potential for magnetism in carbon materials. *Journal of the American Chemical Society*, 127(16):5917–5927, 2005.
- [85] F. Rivadulla, J. S. Zhou, and J. B. Goodenough. Chemical, structural, and transport properties of $\text{Na}_{1-x}\text{CoO}_2$. *Physical Review B*, 68(7):075108, 2003.
- [86] A. V. Rode, R. G. Elliman, E. G. Gamaly, A. I. Veinger, A. G. Christy, S. T. Hyde, and B. Luther-Davies. Electronic and magnetic properties of carbon nanofoam produced by high-repetition-rate laser ablation. *Applied Surface Science*, 197:644–649, 2002.
- [87] A. V. Rode, E. G. Gamaly, A. G. Christy, J. G. F. Gerald, S. T. Hyde, R. G. Elliman, B. Luther-Davies, A. I. Veinger, J. Androulakis, and J. Giapintzakis. Unconventional magnetism in all-carbon nanofoam. *Physical Review B*, 70(5):054407, 2004.
- [88] J. A. Rodriguez-Manzo, F. Lopez-Urias, M. Terrones, and H. Terrones. Magnetism in corrugated carbon nanotubes: The importance of symmetry, defects, and negative curvature. *Nano Letters*, 4(11):2179–2183, 2004.
- [89] H. Sakurai, S. Takenouchi, N. Tsujii, and E. Takayama-Muromachi. Synthesis, characterization, and magnetic properties of $\gamma\text{-Na}_x\text{CoO}_2$ ($0.70 \leq x \leq 0.84$). *Journal of the Physical Society of Japan*, 73(8):2081–2084, 2004.

- [90] B. C. Sales, R. Jin, K. A. Affholter, P. Khalifah, G. M. Veith, and D. Mandrus. Magnetic, thermodynamic, and transport characterization of $\text{Na}_{0.75}\text{CoO}_2$ single crystals. *Physical Review B*, 70(17):174419, 2004.
- [91] R. E. Schaak, T. Klimczuk, M. L. Foo, and R. J. Cava. Superconductivity phase diagram of $\text{Na}_{1-x}\text{CoO}_2 \cdot 1.3\text{H}_2\text{O}$. *Nature*, 424(6948):527–529, 2003.
- [92] Y. G. Shi, Y. L. Liu, H. X. Yang, C. J. Nie, R. Jin, and J. Q. Li. Raman spectroscopy study of $\text{Na}_{1-x}\text{CoO}_2$ and superconducting $\text{Na}_{1-x}\text{CoO}_2 \cdot y\text{H}_2\text{O}$. *Physical Review B*, 70(5):052502, 2004.
- [93] D. J. Singh. Electronic structure of NaCo_2O_4 . *Physical Review B*, 61(20):13397–13402, 2000.
- [94] S. B. Sinnott and R. Andrews. Carbon nanotubes: Synthesis, properties, and applications. *Critical Reviews in Solid State and Materials Sciences*, 26(3):145–249, 2001.
- [95] D. Spemann, K. H. Han, P. Esquinazi, R. Hohne, and T. Butz. Ferromagnetic microstructures in highly oriented pyrolytic graphite created by high energy proton irradiation. *Nuclear Instruments & Methods in Physics Research Section B-Beam Interactions with Materials and Atoms*, 219-20:886–890, 2004.
- [96] D. Spemann, K. H. Han, R. Hohne, T. L. Makarova, P. Esquinazi, and T. Butz. Evidence for intrinsic weak ferromagnetism in a c-60 polymer by pxe and mfm. *Nuclear Instruments and Methods in Physics B*, 210:531–536, 2003.
- [97] J. Sugiyama, H. Itahara, J. H. Brewer, E. J. Ansaldo, T. Motohashi, M. Karpinen, and H. Yamauchi. Static magnetic order in $\text{Na}_{0.75}\text{CoO}_2$ detected by muon spin rotation and relaxation. *Physical Review B*, 67(21):214420, 2003.

- [98] K. Takada, K. Fukuda, M. Osada, I. Nakai, F. Izumi, R. A. Dilanian, K. Kato, M. Takata, H. Sakurai, E. Takayama-Muromachi, and T. Sasaki. Chemical composition and crystal structure of superconducting sodium cobalt oxide bilayer-hydrate. *Journal of Materials Chemistry*, 14(9):1448–1453, 2004.
- [99] K. Takada, H. Sakurai, E. Takayama-Muromachi, F. Izumi, R. A. Dilanian, and T. Sasaki. Superconductivity in two-dimensional CoO_2 layers. *Nature*, 422(6927):53–55, 2003.
- [100] K. Takada, H. Sakurai, E. Takayama-Muromachi, F. Izumi, R. A. Dilanian, and T. Sasaki. Superconductivity of a hydrous sodium cobalt oxide. *Physica C-Superconductivity and Its Applications*, 408-10:165–168, 2004.
- [101] K. Takahata, Y. Iguchi, D. Tanaka, T. Itoh, and I. Terasaki. Low thermal conductivity of the layered oxide $(\text{Na,Ca})\text{Co}_2\text{O}_4$: Another example of a phonon glass and an electron crystal. *Physical Review B*, 61(19):12551–12555, 2000.
- [102] K. Tanaka, M. Kobashi, H. Sanekata, A. Takata, T. Yamabe, S. Mizogami, K. Kawabata, and J. Yamauchi. Peculiar magnetic property of pyrolytic carbon prepared from adamantane. *Journal of Applied Physics*, 71(2):836–841, 1992.
- [103] I. Terasaki, Y. Sasago, and K. Uchinokura. Large thermoelectric power in NaCo_2O_4 single crystals. *Physical Review B*, 56(20):12685–12687, 1997.
- [104] H. Terrones, M. Terrones, F. Lopez-Urias, J. A. Rodriguez-Manzo, and A. L. Mackay. Shape and complexity at the atomic scale: the case of layered nanomaterials. *Philosophical Transactions of the Royal Society of London Series A-Mathematical Physical and Engineering Sciences*, 362(1823):2039–2063, 2004.
- [105] J. B. Torrance, S. Oostra, and A. Nazzal. A new, simple-model for organic

- ferromagnetism and the first organic ferromagnet. *Synthetic Metals*, 19(1-3):709–714, 1987.
- [106] H. E. Troiani, M. Miki-Yoshida, G. A. Camacho-Bragado, M. A. L. Marques, A. Rubio, J. A. Ascencio, and M. Jose-Yacaman. Direct observation of the mechanical properties of single-walled carbon nanotubes and their junctions at the atomic level. *Nano Letters*, 3(6):751–755, 2003.
- [107] S. Venkatraman and A. Manthiram. Synthesis and characterization of p3-type CoO_2 -(δ). *Chemistry of Materials*, 14(9):3907–3912, 2002.
- [108] L. Viciu, Q. Huang, and R. J. Cava. Stoichiometric oxygen content in Na_xCoO_2 . *Physical Review B*, 73(21):212107, 2006.
- [109] A. J. Williams, J. P. Attfield, M. L. Foo, L. Viciu, and R. J. Cava. High-resolution neutron diffraction study of possible charge ordering in $\text{Na}_{0.5}\text{CoO}_2$. *Physical Review B*, 73(13):134401, 2006.
- [110] R. A. Wood, M. H. Lewis, M. R. Lees, S. M. Bennington, M. G. Cain, and N. Kitamura. Ferromagnetic fullerene. *Journal of Physics-Condensed Matter*, 14(22):L385–L391, 2002.
- [111] H. X. Yang, Y. G. Shi, Y. Q. Guo, X. Liu, R. J. Xiao, J. L. Luo, and J. Q. Li. Strontium ordering, structural modulation in layered hexagonal Sr_xCoO_2 and physical properties of $\text{Sr}_{0.35}\text{CoO}_2$. *Materials Research Bulletin*, 42(1):94–101, 2007.
- [112] H. W. Zandbergen, M. Foo, Q. Xu, V. Kumar, and R. J. Cava. Sodium ion ordering in Na_xCoO_2 : Electron diffraction study. *Physical Review B*, 70(2):024101, 2004.

- [113] Y. B. Zhang, Y. W. Tan, H. L. Stormer, and P. Kim. Experimental observation of the quantum hall effect and berry's phase in graphene. *Nature*, 438(7065):201–204, 2005.
- [114] J. S. Zhou, J. B. Goodenough, J. M. Gallardo-Amores, E. Moran, M. A. Alario-Franco, and R. Caudillo. Hexagonal versus perovskite phase of manganite rmno_3 (r=y, ho, er, tm, yb, lu). *Physical Review B*, 74(1):014422, 2006.

Vita

Roman Caudillo, the son of Susana Arredondo and Roberto Caudillo and the younger brother of Roberto and Gerardo, was born in Mexico City, Mexico on January 13, 1977. In 1981, he moved with his family to Flemington, New Jersey, where they lived until relocating to Austin, Texas in 1991. After completing his work at Westlake High School, Austin, Texas, in 1995, he entered Yale University in New Haven, Connecticut. He received the degree of Bachelor of Science in Mechanical Engineering from Yale University in May 2000. During the following years, he was employed as an engineer at Applied Materials, Austin, Texas and RockShox, Colorado Springs, Colorado. In August of 2002, he entered graduate school at the University of Texas at Austin to pursue a Doctorate of Philosophy in Materials Science and Engineering.

Permanent Address: 1104 Exton Cove, Austin, Texas 78733

This dissertation was typeset with $\text{\LaTeX 2}_{\epsilon}$ ^{**} by the author.

^{**} $\text{\LaTeX 2}_{\epsilon}$ is an extension of \LaTeX . \LaTeX is a collection of macros for \TeX . \TeX is a trademark of the American Mathematical Society. The macros used in formatting this dissertation were written by Dinesh Das, Department of Computer Sciences, The University of Texas at Austin, and extended by Bert Kay, James A. Bednar, and Ayman El-Khashab.